

**NAVAL POSTGRADUATE SCHOOL**  
**Monterey, California**



**THESIS**

**PASSIVE DETECTION OF GASES IN THE ATMOSPHERE.  
CASE STUDY: REMOTE SENSING OF SO<sub>2</sub> IN THE UV  
USING LINUS**

by

Anastasios G. Halvatzis

December 2002

Thesis Advisor:

Richard C. Olsen

Second Reader:

Richard M. Harkins

**Approved for public release; distribution is unlimited**

THIS PAGE INTENTIONALLY LEFT BLANK

<b>REPORT DOCUMENTATION PAGE</b>			<i>Form Approved OMB No. 0704-0188</i>	
Public reporting burden for this collection of information is estimated to average 1 hour per response, including the time for reviewing instruction, searching existing data sources, gathering and maintaining the data needed, and completing and reviewing the collection of information. Send comments regarding this burden estimate or any other aspect of this collection of information, including suggestions for reducing this burden, to Washington headquarters Services, Directorate for Information Operations and Reports, 1215 Jefferson Davis Highway, Suite 1204, Arlington, VA 22202-4302, and to the Office of Management and Budget, Paperwork Reduction Project (0704-0188) Washington DC 20503.				
<b>1. AGENCY USE ONLY (Leave blank)</b>		<b>2. REPORT DATE</b> December 2002	<b>3. REPORT TYPE AND DATES COVERED</b> Master's Thesis	
<b>4. TITLE AND SUBTITLE:</b> Passive Detection of Gases in the Atmosphere. Case Study: Remote Sensing of SO <sub>2</sub> in the UV Using LINUS			<b>5. FUNDING NUMBERS</b>	
<b>6. AUTHOR(S):</b> Anastasios G. Halvatzis				
<b>7. PERFORMING ORGANIZATION NAME(S) AND ADDRESS(ES)</b> Naval Postgraduate School Monterey, CA 93943-5000			<b>8. PERFORMING ORGANIZATION REPORT NUMBER</b>	
<b>9. SPONSORING /MONITORING AGENCY NAME(S) AND ADDRESS(ES)</b> N/A			<b>10. SPONSORING/MONITORING AGENCY REPORT NUMBER</b>	
<b>11. SUPPLEMENTARY NOTES:</b> The views expressed in this thesis are those of the author and do not reflect the official policy or position of the Department of Defense or the U.S. Government.				
<b>12a. DISTRIBUTION / AVAILABILITY STATEMENT</b> Approved for public release; distribution is unlimited			<b>12b. DISTRIBUTION CODE</b>	
<b>13. ABSTRACT (maximum 200 words)</b>  An imaging UV spectrometer was used to study sulfuric plumes at Lassen Volcanic National Park, in an effort to identify and quantify SO <sub>2</sub> presence. The NPS instrument, LINUS (Lineate Imaging Near-Ultraviolet Spectrometer) was taken to Lassen on September 13 and 14, 2002. Data taken there are compared to laboratory measurements of SO <sub>2</sub> subsequently run at NPS. These data, along with additional measurements of platinum discharges for wavelength calibration, allow for comparison with atmospheric modeling calculations. Observations were modeled with the standard MODTRAN code. Comparisons between simulated and measured data showed minor indications of SO <sub>2</sub> in the Lassen data. The gas concentration was estimated to be less than 10ppmv.				
<b>14. SUBJECT TERMS:</b> Gas Detection, Sulfur Dioxide, Remote Sensing, Ultraviolet (UV), LINUS, Spectral Imager, MODTRAN			<b>15. NUMBER OF PAGES</b> 135	
			<b>16. PRICE CODE</b>	
<b>17. SECURITY CLASSIFICATION OF REPORT</b> Unclassified	<b>18. SECURITY CLASSIFICATION OF THIS PAGE</b> Unclassified	<b>19. SECURITY CLASSIFICATION OF ABSTRACT</b> Unclassified	<b>20. LIMITATION OF ABSTRACT</b> UL	

NSN 7540-01-280-5500

Standard Form 298 (Rev. 2-89)  
Prescribed by ANSI Std. Z39-18

THIS PAGE INTENTIONALLY LEFT BLANK

**Approved for public release; distribution is unlimited**

**PASSIVE DETECTION OF GASES IN THE ATMOSPHERE.  
CASE STUDY: REMOTE SENSING OF SO<sub>2</sub> IN THE UV USING LINUS**

Anastasios G. Halvatzis  
Major, Hellenic Air Force  
B.S., Hellenic Air Force Academy, 1988  
B.S., University of Macedonia in Thessaloniki, 1995

Submitted in partial fulfillment of the  
requirements for the degree of

**MASTER OF SCIENCE IN PHYSICS**

from the

**NAVAL POSTGRADUATE SCHOOL  
December 2002**

Author: Anastasios G. Halvatzis

Approved by: Richard C. Olsen  
Thesis Advisor

Richard M. Harkins  
Second Reader

William B. Maier II  
Chairman, Department of Physics

THIS PAGE INTENTIONALLY LEFT BLANK

## ABSTRACT

An imaging UV spectrometer was used to study sulfuric plumes at Lassen Volcanic National Park, in an effort to identify and quantify  $\text{SO}_2$  presence. The NPS instrument, LINUS (Lineate Imaging Near-Ultraviolet Spectrometer), was taken to Lassen on September 13 and 14, 2002. Data taken there are compared to laboratory measurements of  $\text{SO}_2$  subsequently run at NPS. These data, along with additional measurements of platinum discharges for wavelength calibration, allow for comparison with atmospheric modeling calculations. Observations were modeled with the standard MODTRAN code. Comparisons between simulated and measured data showed minor indications of  $\text{SO}_2$  in the Lassen data. The gas concentration was estimated to be less than 10ppmv.

THIS PAGE INTENTIONALLY LEFT BLANK



## TABLE OF CONTENTS

I.	INTRODUCTION.....	1
II.	DEFINITIONS AND BASIC PHYSICS .....	3
A.	REMOTE SENSING .....	3
B.	ELECTROMAGNETIC RADIATION.....	4
1.	Electromagnetic Spectrum .....	4
2.	Blackbody Radiation.....	5
3.	Interactions with the Atmosphere .....	7
a.	Scattering.....	9
b.	Transmission.....	9
c.	Absorption.....	9
d.	Reflection.....	10
III.	SULFUR DIOXIDE .....	11
A.	GENERAL.....	11
B.	ABSORPTION PROCESSES IN THE VISIBLE AND UV .....	11
C.	BEER'S LAW - ABSORPTION CROSS SECTION .....	12
D.	SO <sub>2</sub> ABSORPTION CROSS SECTIONS IN THE NEAR UV .....	13
IV.	UV REMOTE SENSING OF VOLCANIC SO <sub>2</sub> .....	19
A.	GENERAL.....	19
B.	TOMS.....	19
C.	BREWER SPECTROMETER .....	22
D.	COSPEC .....	24
1.	Brief Description of Instrument and Its Operation .....	24
2.	Calculations and Limitations of the SO <sub>2</sub> Flux Determination .....	26
3.	SO <sub>2</sub> Flux Measurement Techniques Using COSPEC .....	29
E.	FLYSPEC .....	31
F.	SUMMARY .....	33
V.	LINEATE IMAGING NEAR ULTRA VIOLET SPECTROMETER (LINUS) .....	37
A.	GENERAL.....	37
B.	DEVICE DESCRIPTION AND OPERATION.....	37
1.	Hardware .....	37
a.	Host Computer.....	38
b.	Scanning system .....	38
c.	Camera system .....	38
d.	Optics .....	39
2.	Software .....	40
3.	LINUS Operation .....	40
VI.	EXPERIMENTAL DATA COLLECTION .....	43
A.	GENERAL.....	43

B.	BRIEF VOLCANIC HISTORY OF LASSEN PARK.....	44
C.	DATA ACQUISITION.....	45
1.	First Trip.....	45
2.	Second Trip .....	45
D.	RAW DATA.....	49
VII.	MODELING WITH MODTRAN .....	53
A.	GENERAL.....	53
B.	MODTRAN4 .....	53
C.	SELECTION OF MODTRAN4 INPUT CARDS AND VARIABLE VALUES .....	55
1.	Selection of Input Cards.....	56
2.	Selection of Variable Values .....	56
a.	Card 1.....	57
b.	Card 1A .....	59
c.	Card 2.....	61
d.	Card 2C .....	61
e.	Cards 2C1 and 2C2.....	61
f.	Card 3.....	63
g.	Card 3A1.....	63
h.	Card 3A2.....	64
i.	Card 4.....	64
D.	SIMULATION NOTES .....	64
1.	Variable Values Verification.....	64
2.	Computational Time.....	65
3.	Spectral Resolution .....	65
VIII.	DATA ANALYSIS .....	67
A.	SIMULATED DATA .....	67
1.	LINUS UV Filter.....	67
2.	SO <sub>2</sub> Presence Effects and Spectral Signature .....	68
a.	Figures 8.2 through 8.4.....	68
b.	Figures 8.5 and 8.6.....	71
c.	Figures 8.7 and 8.8.....	74
3.	Spectral Profile Structure Investigation.....	77
B.	EXPERIMENTAL DATA .....	79
1.	Wavelength and SO <sub>2</sub> Calibration of LINUS .....	79
2.	Data Analysis .....	82
a.	Individual Image Analysis.....	82
b.	Ensemble Analysis .....	87
C.	COMPARISON BETWEEN EXPERIMENTAL AND SIMULATED DATA .....	88
D.	SUMMARY .....	93
IX.	SUMMARY, CONCLUSIONS AND RECOMMENDATIONS .....	97
APPENDIX A.	MODTRAN INPUT CARDS AND VARIABLES .....	99

<b>APPENDIX B.</b>	<b>EXAMPLES OF MODTRAN INPUT CARDS.....</b>	<b>101</b>
<b>APPENDIX C.</b>	<b>SELECTED SPECTRAL PROFILES FROM EXPERIMENTAL DATA .....</b>	<b>107</b>
<b>LIST OF REFERENCES</b>	<b>.....</b>	<b>111</b>
<b>INITIAL DISTRIBUTION LIST.....</b>		<b>115</b>

THIS PAGE INTENTIONALLY LEFT BLANK

## LIST OF FIGURES

Figure 2.1.	Spectral imager classifications. (From: Multispectral Users Guide, 1995) .....	4
Figure 2.2.	Electromagnetic spectrum. (From: Barrett & Curtis, 1982).....	5
Figure 2.3.	Blackbody radiation curves for various temperatures. As shown by (a) and (b) as the temperature increases there is a significant change of scale and the maximum irradiance occurs at shorter wavelengths. (From: Elachi, 1987).....	6
Figure 2.4.	Atmospheric layers. (From: Lenoble, 1993) .....	8
Figure 2.5.	Interaction of EM radiation with the atmosphere. (From: Gibson, 2000) .....	8
Figure 2.6.	Solar irradiance approximated by a blackbody, at the top of the atmosphere (TOA) and at sea level. (From: Elachi, 1987) .....	10
Figure 3.1.	Absorption spectrum of SO <sub>2</sub> . (From: Atkins, 1982).....	12
Figure 3.2.	SO <sub>2</sub> absorption cross section from 290 to 317nm. (From: Brassington, 1981).....	15
Figure 3.3.	Comparison of measurements between Brassington (solid line) and Thomson et al. (dotted line). (From: Brassington, 1981).....	16
Figure 3.4.	Comparison of measurements between Brassington, Thomson et al. and Woods et al. for the 300.03nm absorption peak. (From: Brassington, 1981) .	16
Figure 3.5.	High precision SO <sub>2</sub> absorption cross-section peaks at 298 and 300nm at 20 <sup>0</sup> C. The dotted line is with 1.01x10 <sup>-5</sup> Pa of nitrogen buffer gas. The solid lines are is for SO <sub>2</sub> alone. The original article refers to the solid line as the one with the buffer gas and the dotted as SO <sub>2</sub> alone, but this is obviously opposite since the buffer gas smoothes out the spectral details. (From: Woods et al., 1980).....	17
Figure 3.6.	High resolution absorption cross section of SO <sub>2</sub> at 20 <sup>0</sup> C with nitrogen buffer gas over the spectral region 297.8-300.3nm. (From: Woods et al., 1980).....	17
Figure 3.7.	SO <sub>2</sub> absorption cross section for (a) 295 K and (b) 210 K. (From: Thomas et al., 1987) .....	18
Figure 4.1.	Absorption cross sections of atmospheric UV absorbers. (From: Strickland, 1999).....	20
Figure 4.2.	False-color image of SO <sub>2</sub> from the June 16, 1991 eruption of Mt. Pinatubo, Philippines, produced from TOMS data. The triangular symbol marks the location of the source volcano. (From: < <a href="http://skye.gsfc.nasa.gov">http://skye.gsfc.nasa.gov</a> >, 2002) .....	21
Figure 4.3.	Brewer Station on the roof of the Environment Canada Building, Toronto. (From: < <a href="http://www.ns.ec.gc.ca">http://www.ns.ec.gc.ca</a> >, 2002) .....	23
Figure 4.4.	Example of Brewer station output. (From: WOUDC, 2002).....	23
Figure 4.5.	Close-up view of COSPEC. (From: USGS website, 2002).....	24
Figure 4.6.	Internal design of COSPEC. (From: COSPEC IV Manual, 1976) .....	25
Figure 4.7.	Example of COSPEC output to a paper chart recorder. (From: < <a href="http://www.gsj.jp">http://www.gsj.jp</a> >, 2002) .....	26

Figure 4.8.	Example of long-term COSPEC calculation results in metric tons/day (mt/d) of SO <sub>2</sub> Kilauea Summit, Hawaii SO <sub>2</sub> emission rates. (From: Elias et al., 1998).....	27
Figure 4.9.	Example of estimated uncertainties of SO <sub>2</sub> flux calculations based on vehicle-mounted COSPEC. The black vertical bars represent the standard deviation of all traverses on a single day. Kilauea's East Rift Zone, Hawaii. (From: Elias et al., 1998).....	28
Figure 4.10.	COSPEC mounted on vehicle. (From: < <a href="http://www.volcanoes.ca">http://www.volcanoes.ca</a> >, 2002) ...	30
Figure 4.11.	COSPEC on airplane and on ground. (From: USGS website, 2002) .....	30
Figure 4.12.	Concurrent data collection with COSPEC and FLYSPEC. (From: Mares, 2002) 32	
Figure 4.13.	FLYSPEC sample data frame collected at Kilauea Volcano, Hawaii in March 2002. (From: Mares, 2002) .....	32
Figure 4.14.	Comparison between COSPEC and FLYSPEC data taken concurrently in March 2002 at Kilauea Volcano, Hawaii. (From: Mares, 2002) .....	33
Figure 4.15.	UV sensors used in the detection of volcanic SO <sub>2</sub> . (From: Krueger at al., 2000) 34	
Figure 4.16.	Absorption spectra of SO <sub>2</sub> and O <sub>3</sub> and wavelength bands used by the UV detectors. (From: Krueger at al., 2000).....	35
Figure 5.1.	LINUS architecture. (From: Kompatzki, 2000).....	37
Figure 5.2.	LINUS optical layout. (From: Kompatzki, 2000) .....	39
Figure 5.3.	Spectral response for the 300nm UV filter. (From: Filter Specs).....	39
Figure 5.4.	Pictures of LINUS. On the left side is the electronics section with the computer the amplifier and the camera pulser and cooler. On the right side is the optics section, which also includes the camera body and the scanner mirror assembly. ....	40
Figure 5.5.	LINUS spectral imaging schematic diagram.....	42
Figure 5.6.	Data set produced by LINUS output. ....	42
Figure 6.1.	Map of Lassen Volcanic National Park. The square on the right is magnification of the area included in the left box. Locations 1, 2 and 3 are the spots where the measurements took place. (After: USGS website, 2002).....	43
Figure 6.2.	Some of the Sulfur Works vents. ....	44
Figure 6.3.	The May 22, 1915 explosive eruption of Lassen Peak. (From: USGS website, 2002).....	45
Figure 6.4.	Sulfur Works as seen from location 1.....	47
Figure 6.5.	LINUS setup at location 2.....	48
Figure 6.6.	Screenshot of LINUS monitor at the time of data file acquisition. This is how the raw data looked like to the operators. ....	50
Figure 6.7.	The previously presented data file in pseudocolor, which gave to Linus operators a first feeling about the intensity variations along the spectrum contained in the image. ....	51
Figure 6.8.	A first indication of the spectral profile of the recorded image by averaging the middle 256 lines. Vertical axis units are Digital Numbers (DN).....	52

Figure 7.1.	MODTRAN results for single and multiple scattering.....	58
Figure 7.2.	Ratio of single divided by multiple scattering from MODTRAN results. ....	58
Figure 7.3.	Effect of using the DISORT algorithm in the spectral region of interest. ....	59
Figure 7.4.	Solar irradiance comparison for $5\text{cm}^{-1}$ (LSUN=F) and $1\text{cm}^{-1}$ (LSUN=T) spectral resolution. Results for Lassen Park with MODTRAN standard atmosphere 2. ....	60
Figure 7.5.	SO <sub>2</sub> concentration as a function of altitude for the MODTRAN standard atmosphere 2. ....	63
Figure 8.1.	The continuous line shows the Gaussian fit of the LINUS filter response. Diamonds show data points taken from the real filter response curve presented in figure 5.3. ....	67
Figure 8.2.	Simulated sky radiance spectral profiles for various SO <sub>2</sub> concentrations at Sulfur Works without LINUS filter effect. Resolution 0.08nm. ....	69
Figure 8.3.	Simulated sky radiance spectral profiles for various SO <sub>2</sub> concentrations at Sulfur Works, without LINUS filter effect, at smaller scale than figure 8.2. Resolution 0.08nm. ....	70
Figure 8.4.	Simulated sky radiance spectral profiles for various SO <sub>2</sub> concentrations at Sulfur Works without LINUS filter effect. Resolution 0.5nm. ....	70
Figure 8.5.	Simulated spectral profiles for various SO <sub>2</sub> concentrations at Sulfur Works with LINUS filter effect. Resolution 0.08nm. ....	72
Figure 8.6.	Simulated spectral profiles for various SO <sub>2</sub> concentrations at Sulfur Works with LINUS filter effect. Resolution 0.5nm. ....	73
Figure 8.7.	Ratios of SO <sub>2</sub> concentrations to regular atmosphere at 0.08nm resolution. ....	75
Figure 8.8.	Ratios of SO <sub>2</sub> concentrations to regular atmosphere at 0.5nm resolution. ....	76
Figure 8.9.	Spectrum of regular atmosphere and atmosphere with no O <sub>3</sub> . ....	77
Figure 8.10.	Ratio of radiances in log-scale of regular atmosphere to atmosphere with no O <sub>3</sub> . ....	78
Figure 8.11.	Linear ratio of radiances of regular atmosphere to atmosphere with no O <sub>3</sub> . ....	78
Figure 8.12.	Spectrums of solar irradiance out of the atmosphere and regular atmosphere radiance at 2.13km altitude. ....	79
Figure 8.13.	Results of wavelength calibration of LINUS using a platinum lamp. ....	80
Figure 8.14.	SO <sub>2</sub> calibration results of LINUS. ....	81
Figure 8.15.	Plot of the averages from figures C.2 through C.5. ....	83
Figure 8.16.	Comparison of spectral profiles with strong structure over the Sulfur Works vents (possible SO <sub>2</sub> presence) with Lassen Peak (clear atmosphere). ....	84
Figure 8.17.	Ratios of strong Sulfur Works spectra (possible SO <sub>2</sub> existence) with strong Lassen Peak spectra (clear atmosphere). ....	85
Figure 8.18.	Ratios of the Sulfur Works averages (blue, green) to the Lassen Peak average (red) shown in figure 8.15 above. ....	86
Figure 8.19.	Ratios of Sulfur Works (possible SO <sub>2</sub> existence) with Lassen Peak spectra (clear atmosphere). Spectral profiles that do not have strong structure were used. ....	86
Figure 8.20.	Summary of the experimental measurements with a simulated clear atmosphere and SO <sub>2</sub> calibration spectral profiles. ....	87

Figure 8.21.	Measured and simulated spectral profiles of clear atmosphere. The simulated data are in 0.08nm resolution.....	89
Figure 8.22.	Measured and simulated spectral profiles of clear atmosphere. The simulated data are in 0.5nm resolution. ....	89
Figure 8.23.	Measured and simulated spectral profiles of clear atmosphere and simulated with 10ppmv SO <sub>2</sub> atmosphere. The simulated data are in 0.5nm resolution. ....	90
Figure 8.24.	Ratios of data taken over the Sulfur Works vents (SW_080 and SW_206) and clear atmosphere at Lassen Peak (SW_503) divided by simulated clear atmosphere. ....	91
Figure 8.25.	Inverted ratios of simulated clear atmosphere and 10ppmv of SO <sub>2</sub> -containing atmosphere divided by clear atmosphere at Lassen Peak (SW_503).....	92
Figure 8.26.	Ratios of selected experimental to simulated data.....	92
Figure 8.27.	Comparison between MODTRAN and SO <sub>2</sub> calibration absorption characteristics.....	93
Figure C.1.	Plot of the spectral profiles of all selected images. ....	107
Figure C.2.	Plot of spectral profiles of one group of selected images at Sulfur Works...	108
Figure C.3.	Plot of spectral profiles of another group of selected images at Sulfur Works.....	108
Figure C.4.	Plot of spectral profiles of selected images at Lassen Peak.....	109
Figure C.5.	Plot of spectral profiles of measurements taken with the aperture of LINUS covered. ....	109



## LIST OF TABLES

Table 2.1.	Atmospheric constituents. (From: Durkee, 1999) .....	7
Table 4.1.	Satellite missions with TOMS instruments. (From: Krueger et al., 2000) .....	22
Table 4.2.	Calculation of SO <sub>2</sub> flux from COSPEC output. (From: Stoiber et al., 1983) ..	27
Table 4.3.	Limitations of the COSPEC calculations. (From: Stoiber et al., 1983) .....	28
Table 7.1.	Molecular species for user defined atmospheric profiles. SO <sub>2</sub> is number 9. (After MODTRAN4 User's Manual, 1999).....	55

THIS PAGE INTENTIONALLY LEFT BLANK

## ACKNOWLEDGMENTS

I would like to express my acknowledgments to the people that directly or indirectly contributed to the creation of this thesis. First of all, many thanks to Professor R. C. Olsen for his help and guidance. His skills and experience with IDL were invaluable in the manipulation and processing of the experimental data. Thanks to Mr. R. M. Harkins for his help with LINUS in the lab and during the deployments in the field. Finally, I would like to express my deep gratitude to my father who, by his support and direction in my early years, was one of the primary reasons for my presence in Monterey and subsequently for this thesis.

THIS PAGE INTENTIONALLY LEFT BLANK

## I. INTRODUCTION

Advancements in semiconductor technology during the past two decades were a big impetus to Remote Sensing. As sensor properties and computational power increases, Remote Sensing is finding applications in an increasing number of areas outside its traditional boundaries. The most heavily used part of the electromagnetic spectrum was the visible region followed later by the infrared and microwave regions. The ultraviolet region, although the least used so far, gives the potential of many new applications.

Remote Sensing of the atmosphere and its constituents has long been of great importance for many reasons, both civilian and military. The ability to detect, quantify and calculate the distribution of the atmospheric constituents is of great significance. In the civilian case, monitoring of the atmosphere is directly related to public safety, quality of life and economy, for example, for weather prediction, the monitoring of ozone, greenhouse effect gases and pollution, and the detection of accidents and cataclysmic events that affect the atmosphere, such as volcano eruptions. In the case of the military, Remote Sensing of the atmosphere can be used for tactical and strategic intelligence and battlefield awareness by finding chemical/biological weapons gas clouds from safe distances, and rocket and aircraft exhaust plumes, for example.

The Physics Department of the Naval Postgraduate School has over ten years of experience with the design and development of numerous devices due to research projects related to atmospheric Remote Sensing in the UV. The first device, beginning in 1990, was MUSTANG (Middle Ultraviolet SpecTrograph for Analysis of Nitrogen Gases) and continued with DUUVIS (Dual Use UltraViolet Imaging Spectrometer), NUVIS (Naval Postgraduate School UltraViolet Imaging Spectrometer), with the latest being LINUS (Lineate Imaging Ultraviolet Spectrometer).

LINUS is an imaging spectrometer with the ability to operate from the UV through Near UV to the first half of the visible spectrum depending on its configuration and calibration. Currently, it is set-up to operate at approximately  $300 \pm 10$  nm with the purpose of detecting Sulfur Dioxide ( $\text{SO}_2$ ).  $\text{SO}_2$  is a trace atmospheric gas, which can be

found in urban areas as a primary pollutant in the exhaust plums of industrial smokestacks and in volcanic plumes. It has strong absorption bands centered at 300nm.

The purposes of this thesis effort were to develop the operational capability of LINUS, deploy it in the field in order to acquire data of natural plumes, and finally analyze the data to specify the plume content in SO<sub>2</sub>. The device was deployed at Lassen Volcanic National Park for experimental data acquisition in August and September of 2002. The measurements were also modeled with the MODTRAN4 code, so that the experimental data can be better evaluated through analysis and direct comparison.

This thesis consists of nine chapters and 3 appendices. Chapter II presents some definitions and the basic physics involved in the operation of LINUS and analysis of its measurements. Chapter III is dedicated to SO<sub>2</sub>, which is the subject of the measurements. It examines the absorption behavior of the gas in the spectral region of interest as documented by detailed measurements of its absorption cross-section. Chapter IV presents the current capabilities and practices worldwide in the detection and measurement of volcanic SO<sub>2</sub> in the UV. Chapter V gives a brief description of LINUS and its operation. Detailed information can be found in other theses: Kompatzki, 2000; Blackwell, 2001, Kuriger, 2001 and Gray, 2002. Chapter VI describes the deployment and experimental data collection with LINUS at Lassen Volcanic Park and also provides a first indication of the raw data. Chapter VII presents the concepts and technical details of modeling the LINUS data with the MODTRAN4 code. The analysis of both the simulated and experimental data is presented in chapter VIII. Finally, chapter IX summarizes the conclusions deduced by this project.

## **II. DEFINITIONS AND BASIC PHYSICS**

### **A. REMOTE SENSING**

Remote Sensing is the acquisition of information about an object without physical contact (Manual of Remote Sensing, 1983). The information is acquired by detecting and measuring changes that the object imposes on the surrounding field. This can include electromagnetic or acoustic energy emitted or reflected by the object or changes to the gravitational or magnetic field due to the presence of the object (Elachi, 1987). Remote sensing measurements that depend on a natural energy source are called passive, while those that depend on a man-made energy source, which usually is on the same platform as the sensor, are called active.

Remote sensing in the electromagnetic spectrum depends upon observed spectral differences in the energy reflected or emitted from features of interest. The observation of features at several different wavelengths in an effort to derive information about the features and their distributions is the basis of multispectral remote sensing (Campbell, 1987).

With the developments in detector technologies, new detectors termed imaging spectrometers are available. They are capable of recording image data in a large number, typically hundreds, of spectral channels. For a given pixel, enough samples of its reflectance properties can be obtained to allow a very accurate characterization of the pixel's spectral reflectance or emittance curve, over the spectral region covered by the sensor. This is a case of hyperspectral remote sensing. Data analysis for the hyperspectral data sets can extend beyond image analysis and involve procedures for the recognition of fine spectral features in recorded spectra of individual pixels. These procedures range from using models based on a scientific understanding of the spectroscopic processes involved in spectrum formation, to library searching techniques that allow identification based on matches to library prototypes (Richards & Jia, 1999). Hyperspectral imagers, such as LINUS, produce a spectral image of the scene where each pixel has three components: two spatial (x and y coordinates) and one spectral. Usually the sensor

records one of the spatial components and the spectral component and scans the other spatial dimension. The data can be thought as a hyperspectral data cube.

Even higher spectral resolution can be achieved by ultraspectral imagers, which can record subtle spectral details of materials. Figure 2.1 illustrates the classification of the three remote sensing areas.

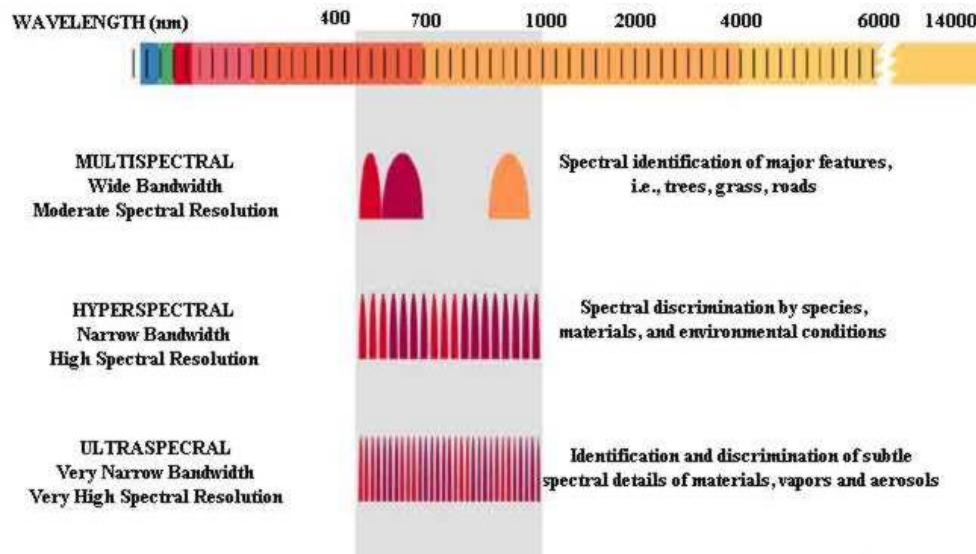


Figure 2.1. Spectral imager classifications. (From: Multispectral Users Guide, 1995)

## B. ELECTROMAGNETIC RADIATION

### 1. Electromagnetic Spectrum

Although the electromagnetic spectrum is continuous in nature, major divisions and subdivisions have been established for convenience and by tradition. Figure 2.1 shows the typical division of the spectrum in terms of frequency, wavelength and photon energy. The spectral regions most heavily used in remote sensing are the visible and infrared but the ultraviolet and microwave regions are also used.



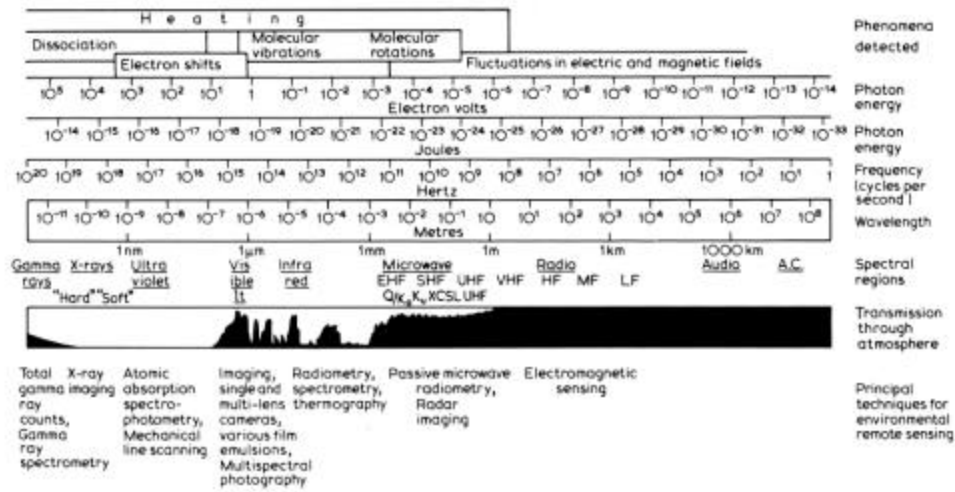


Figure 2.2. Electromagnetic spectrum. (From: Barrett & Curtis, 1982)

## 2. Blackbody Radiation

All objects at temperatures above absolute zero radiate energy. When they are in thermal equilibrium with their surroundings, they absorb and radiate the same amount of energy and their temperature stays constant with time. As the temperature of the object increases, the spectral distribution and amplitude of the radiated energy changes. In order to approximate this behavior, the concept of blackbody was introduced. Blackbody is an ideal source of electromagnetic energy, with radiation properties that depend only on its temperature. The spectral distribution of the radiated intensity  $R$ , is given by Planck's radiation law:

$$R(\lambda) = \frac{2\pi^5 k^4}{15} \frac{1}{e^{\frac{hc}{\lambda kT}} - 1} \quad (2.1)$$

where  $h$  is the Planck's constant,  $c$  is the speed of light,  $\lambda$  is the wavelength,  $k$  is the Boltzman's constant and  $T$  is the absolute temperature of the blackbody. Figure 2.3 illustrates the behavior of a blackbody at various temperatures.

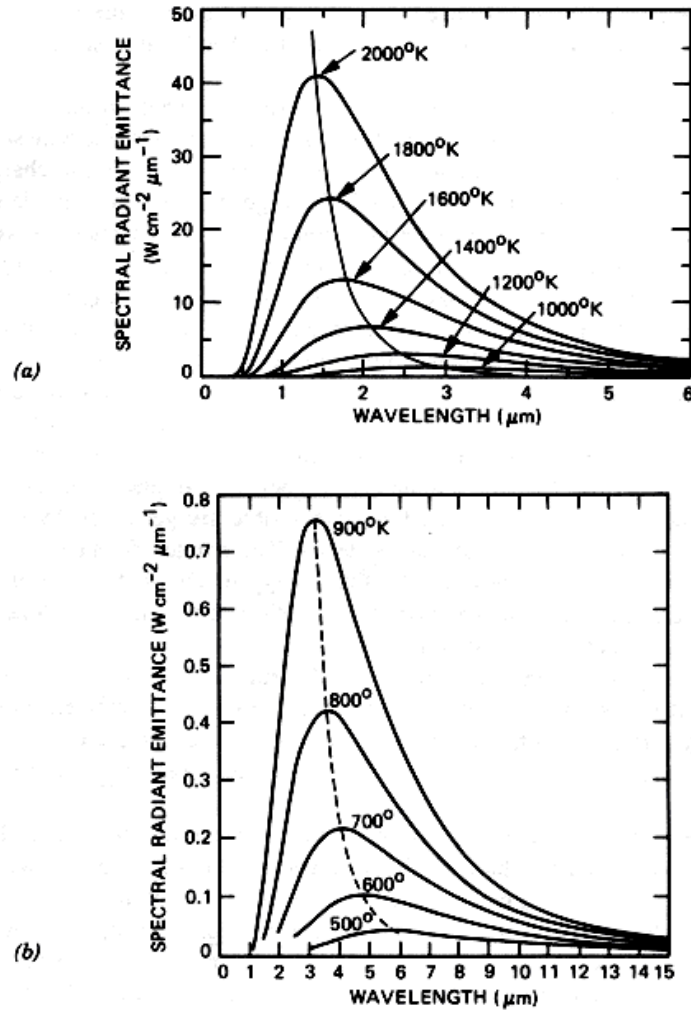


Figure 2.3. Blackbody radiation curves for various temperatures. As shown by (a) and (b) as the temperature increases there is a significant change of scale and the maximum irradiance occurs at shorter wavelengths. (From: Elachi, 1987)

The total radiated energy over the entire spectrum is given by Stefan -Boltzmann's law:

$$R = sT^4 \quad (2.2)$$

where  $s = 5.67 \times 10^{-8} \text{ [W/(m}^2\text{K}^4\text{)]}$  and the maximum of the spectral distribution is given by Wien's displacement law:

$$\lambda_{\max} T = 2898 [\mu\text{mK}] \quad (2.3)$$

The concept of blackbody is important because it can be used to model the sun, which is the source for passive remote sensing. Figure 2.6 shows that the sun radiates approximately as a blackbody at about 5900K.

### 3. Interactions with the Atmosphere

Since all radiation used for remote sensing of terrestrial objects must pass through the atmosphere, interactions with it are very important. The atmosphere consists of a generally homogeneous mixture of O<sub>2</sub>, N<sub>2</sub> and Ar with variable concentrations of water vapor, CO<sub>2</sub> and O<sub>3</sub>. The pressure and density of the atmosphere decrease approximately exponentially with altitude while the temperature has a more complicated variation, which characterizes the division of the atmosphere into layers. The composition of the atmosphere is shown in table 2.1 and its layers are shown in figure 2.4.

Constituent Name / (type)	Formula	Molec. Mass	% by volume
Nitrogen/ (Permanent)	N <sub>2</sub>	28.0134	78.084
Oxygen / (Permanent)	O <sub>2</sub>	31.9988	20.9476
Argon / (Permanent)	Ar	39.948	0.934
Water Vapor / (Variable)	H <sub>2</sub> O	18.0160	0-7
Carbon Dioxide / (Variable)	CO <sub>2</sub>	44.00995	0.01-0.1
Ozone / (Variable)	O <sub>3</sub>	47.9982	0-0.01
Neon / (Permanent)	Ne	20.183	0.001818
Helium / (Permanent)	He	4.0026	0.000524
Methane / (Permanent)	CH <sub>4</sub>	16.04303	0.0002
Sulfur Dioxide / (Variable)	SO <sub>2</sub>	64.064	0-0.0001
Hydrogen / (Permanent)	H <sub>2</sub>	2.01594	0.00005
Nitrogen Dioxide / (Variable)	NO <sub>2</sub>	46.0055	0-0.000002

Table 2.1. Atmospheric constituents. (From: Durkee, 1999)

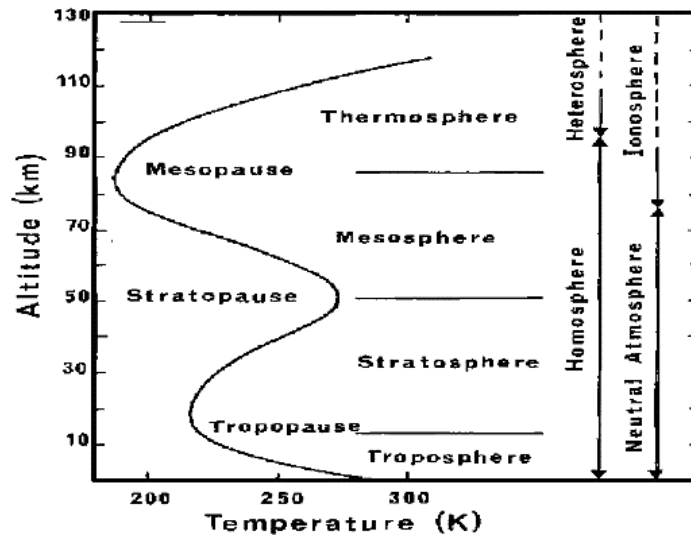


Figure 2.4. Atmospheric layers. (From: Lenoble, 1993)

The main processes between the electromagnetic radiation and the atmosphere are graphically illustrated in figure 2.5 below and are as follows:

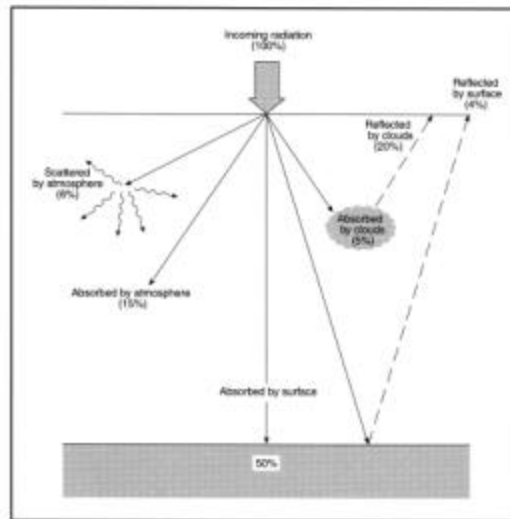


Figure 2.5. Interaction of EM radiation with the atmosphere. (From: Gibson, 2000)

### ***a. Scattering***

Scattering is the redirection of the radiation by molecules of atmospheric gases or by particles suspended in the atmosphere. The amount of scattering depends on the size of the molecules or particles, their abundance, the wavelength of the radiation and the depth of the atmosphere through which the radiation is traveling.

*Rayleigh* scattering occurs when molecules of atmospheric gases or particles have diameters that are very small relative to the wavelength of the radiation. It is wavelength dependent with a factor of  $(1/\lambda^4)$ , which means that short wavelengths are scattered more. It is the dominant scattering process above the troposphere and is responsible for the existence of the UV background of the sky used for LINUS measurements.

*Mie* scattering is caused by larger particles, such as dust smoke and water droplets, that their diameters are comparable to the wavelength of electromagnetic radiation. It is wavelength dependent but in a very complicated way. It is dominant in the lower atmosphere, where larger particles are more abundant.

*Nonselective* scattering is caused by particles that are much larger than the wavelength of the scattered radiation, such as larger water droplets or large particles of dust. It is not wavelength dependent and causes a whitish or grayish haze at visible wavelengths (Campbell, 1987).

### ***b. Transmission***

Transmission is the process when incident radiation passes through the atmosphere without measurable attenuation. As the radiation passes through layers of the atmosphere with different constituents and densities, it is refracted (deflected). Refraction affects the speed (decreases) and the wavelength (increases) of the radiation but not its frequency.

### ***c. Absorption***

Absorption is an important process since it affects the electromagnetic radiation available for remote sensing and also - for the purpose of this thesis - provides

the basis for detection and quantitative estimation of the  $\text{SO}_2$ . Through this process, the radiation is absorbed by molecules and it raises the temperature of the atmosphere, causes chemical reactions or is reradiated at longer wavelengths. The main molecules responsible for the atmospheric absorption are  $\text{O}_3$ ,  $\text{O}_2$ ,  $\text{H}_2\text{O}$  and  $\text{CO}_2$ . The combined result of scattering and absorption to the amount of solar radiation reaching the surface of the earth at each wavelength is illustrated in figure 2.6 below.

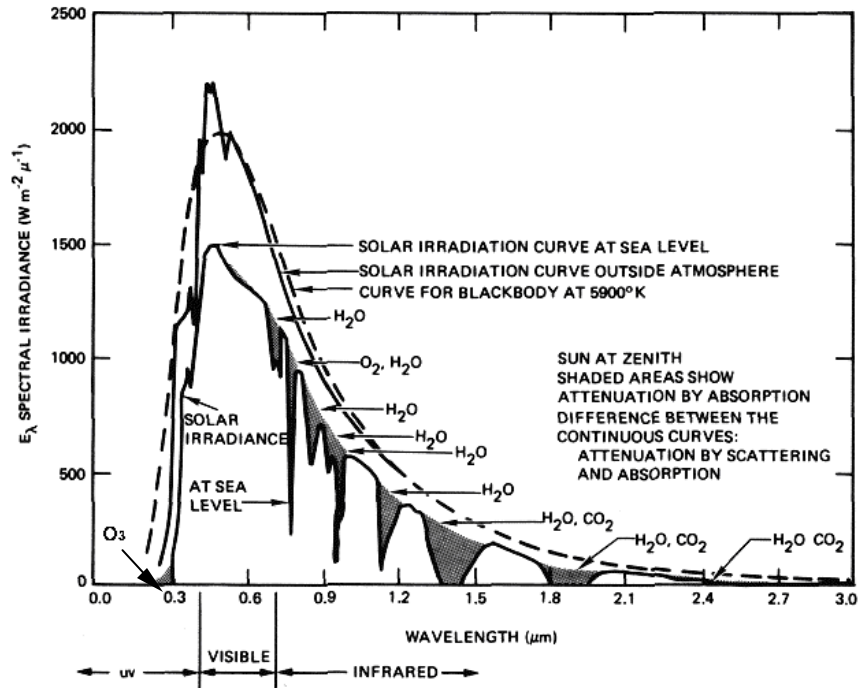


Figure 2.6. Solar irradiance approximated by a blackbody, at the top of the atmosphere (TOA) and at sea level. (From: Elachi, 1987)

#### *d. Reflection*

Reflection is mainly caused by clouds and is not a topic of interest for this thesis.

### **III. SULFUR DIOXIDE**

#### **A. GENERAL**

Sulfur dioxide ( $\text{SO}_2$ ) is a trace chemical compound in the Earth's atmosphere, mainly present in the troposphere where it is a primary pollutant released by fossil fuel combustion, volcanic emissions, oxidation of organic material in soils and biogenic emissions over the oceans. Some estimates consider that coal burning accounts for 50% of the annual global emissions and oil burning for another 25 -30%. Volcanic emissions due to eruptions are responsible for the presence of  $\text{SO}_2$  in the stratosphere.

$\text{SO}_2$  is a colorless gas with a suffocating, choking odor and its density is over twice of that of air at the same conditions (2.618 g/lit at 25 °C and 1 atm). It reacts on the surface of various airborne solid particles (aerosols) and can be oxidized within airborne water droplets, producing sulfuric acid, which can be transported by winds and is deposited as acid rain.

The lifetime of  $\text{SO}_2$  in the troposphere is a few days, while in the stratosphere it is several weeks. This makes  $\text{SO}_2$  from volcanoes one of the most important sources of stratospheric aerosols. Its abundance in the atmosphere is highly variable above a very low background concentration. Clean continental air contains less than 1 ppb of  $\text{SO}_2$ .

#### **B. ABSORPTION PROCESSES IN THE VISIBLE AND UV**

The absorption processes in the visible and UV regions of the spectrum mainly involve electronic transitions of the valence electrons of the atoms. When an electronic transition occurs in a molecule, the redistribution of the electrons changes the electrostatic forces operating on the nuclei. The molecule responds to the change of forces by bursting into vibration. In other words, an electronic transition is usually accompanied by a vibrational transition. The extra vibrational structure in a spectrum can be resolved if the sample is gaseous but in a liquid or solid sample, the lines merge together and result in a broad, almost featureless line. The vibrational transitions that accompany the electronic transitions are themselves accompanied by rotational transitions. As a result, the electronic spectra of gaseous samples can be very complicated

(Atkins, 1982). The considerable vibrational structure of gaseous  $\text{SO}_2$  at  $25^\circ\text{C}$  is shown in figure 3.1.

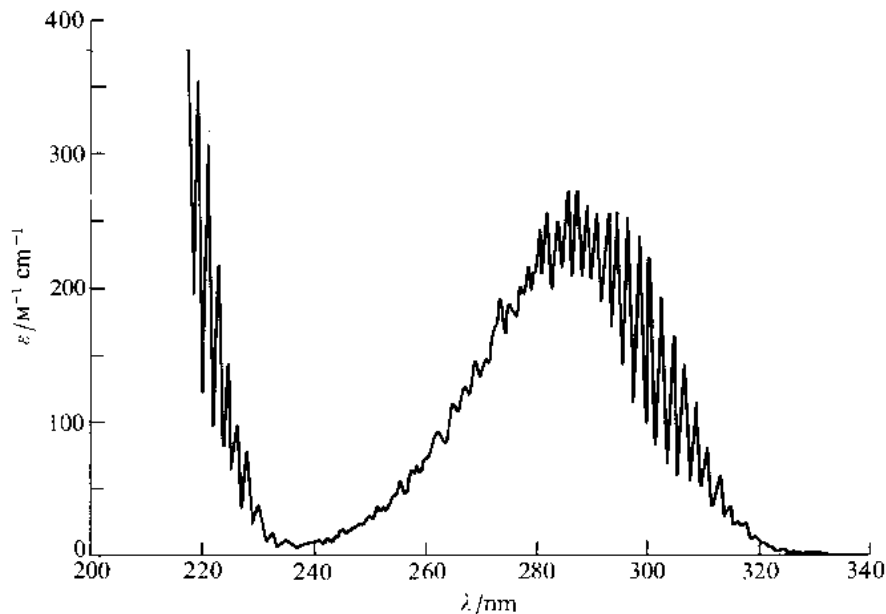


Figure 3.1. Absorption spectrum of  $\text{SO}_2$ . (From: Atkins, 1982)

### C. BEER'S LAW - ABSORPTION CROSS SECTION

When a beam of monochromatic radiation of initial intensity  $I_0$  passes through a material, absorption takes place and the beam leaving the material has smaller intensity,  $I$ . The absorption of a photon of the radiation corresponds to a change in the internal state of a molecule of the material between two energy levels. The energy of the transition is determined by the separation of the energy levels between the two states.

Assume that the material density is  $c$ . Then, the absorption of radiation by a thin layer of thickness  $dx$  at a distance  $x$  from the surface is:

$$dI = -\sigma c I dx \quad (3.1)$$

where  $\sigma$  is the absorption cross section of the material. The *absorption cross section* is a measure of a molecule's ability to absorb radiation at a specified wavelength and is usually expressed in  $\text{cm}^2/\text{particle}$ . It depends on the kind of molecule, i.e., the material,



and the wavelength of the radiation. If the path length of the radiation through the material is  $l$ , then by integrating equation (3.1) the transmitted radiation becomes:

$$I = I_0 e^{-scl} \quad (3.2)$$

The above equation is Beer's law and applies to optically thin samples. Another version of the law contains the molar absorption coefficient  $\epsilon$ .

Beer's law is the main theoretical tool used to calculate absorption cross sections for various materials. In the experimental setups, a monochromatic light of known intensity is directed into a sample with specific characteristics, such as temperature and pressure, the outgoing light intensity is measured, and thus, the absorption cross section can be calculated.

#### **D. SO<sub>2</sub> ABSORPTION CROSS SECTIONS IN THE NEAR UV**

The absorption spectrum of SO<sub>2</sub> between 285 and 315nm displays a series of well-defined peaks and troughs spaced approximately 2nm apart. This constitutes a strong spectral signature useful in remote sensing applications. For this reason, LINUS was designed to operate in the region 290-310nm with a maximum spectral response at about 300nm.

One application is the Differential Absorption Lidar (DIAL), which uses the difference in absorption cross section between an absorption peak and an adjacent trough to measure SO<sub>2</sub> concentrations remotely for environmental monitoring purposes. The maximum differential absorption cross section occurs close to 300 nm. This, considering that most DIAL systems use dye lasers that work most efficiently at this wavelength, raised the need for very accurate measurements of the SO<sub>2</sub> absorption cross section in this wavelength region (Brassington, 1981). Another application is the processing of the data produced by the TOMS instrument, which will be discussed later in this thesis.

There were several measurements reviewed for this region of wavelengths with spectral resolutions varying from moderate ( $\sim 0.02\text{nm}$ ) to high ( $\sim 0.002\text{nm}$ ). In most of these cases, the experimental setup included frequency doubled dye lasers and used cells containing SO<sub>2</sub> at atmospheric temperatures ( $\sim 20^\circ\text{C}$ ) and pressures. Measurements at

high ( $\sim 100^{\circ}\text{C}$ ) and low ( $-60^{\circ}\text{C}$ ) temperatures and low pressures were also conducted. In some cases, dry nitrogen was used as a buffer gas to simulate atmospheric pressure broadening, which smears the fine spectral structure of pure  $\text{SO}_2$ .

The results of some of these measurements are presented in figures 3.2 through 3.7 below. Figure 3.2, from the work of Brassington in 1981, shows the absorption cross section of  $\text{SO}_2$  in the spectral region from 290 to 317nm, while figures 3.3 and 3.4 compare the results of that work with previous results for the peaks at 296, 298 and 300nm. The presented Brassington measurements were conducted over a broad spectral region compared to previous works at moderate resolution (0.01 nm), low pressures (2.3-17.6mbars) and ambient temperatures (292–300K), without the use of buffer gas. In the work of Woods et al., 1980, high-resolution (0.002nm) measurements were conducted in the spectral region from 297.0 to 301.0nm at  $20^{\circ}\text{C}$  with the use of nitrogen buffer gas at 1atm in order to simulate in the laboratory, conditions encountered in the lower atmosphere (pressure broadening). Figure 3.5 from that work shows the absorption cross section peaks at 298 and 300nm in detail, while figure 3.6 shows the same two peaks with the in-between trough and with nitrogen buffer gas. Finally, figure 3.7 from Thomas et al., shows the  $\text{SO}_2$  absorption cross section in the region from 300.0 to 320.4nm for room and low temperature (295 and 210K) at moderate resolution (0.03nm).

LINUS, used for the measurements in this thesis, is currently set up to operate in the spectral region from 290 to 310nm with a maximum spectral response at about 300nm. The above-mentioned measurements, illustrated in the following figures, are of great significance since they provide the needed spectral signatures that will allow recognition of potential  $\text{SO}_2$  detection by LINUS and subsequent quantitative estimations.

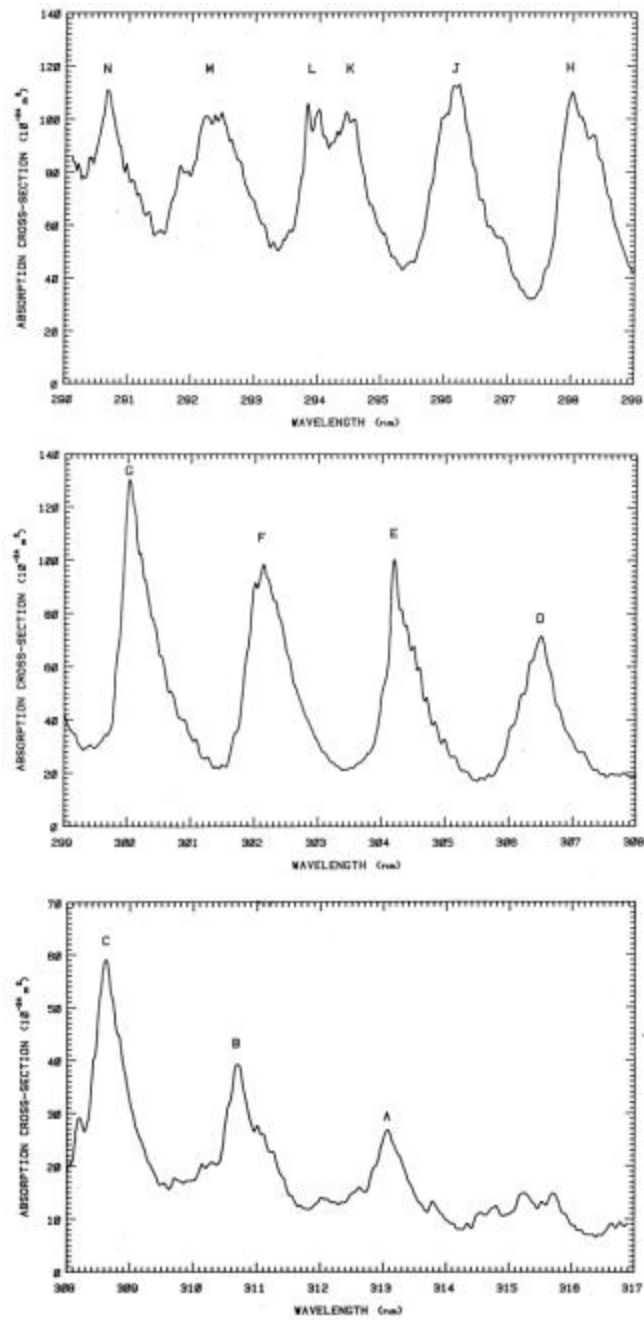


Figure 3.2. SO<sub>2</sub> absorption cross section from 290 to 317nm. (From: Brassington, 1981)

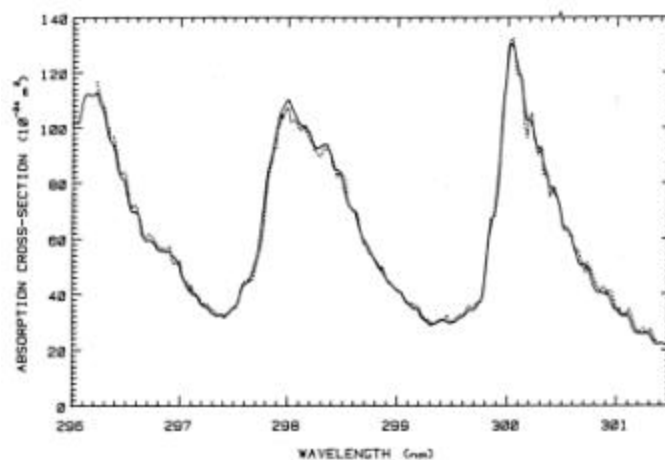


Figure 3.3. Comparison of measurements between Brassington (solid line) and Thomson et al. (dotted line). (From: Brassington, 1981)

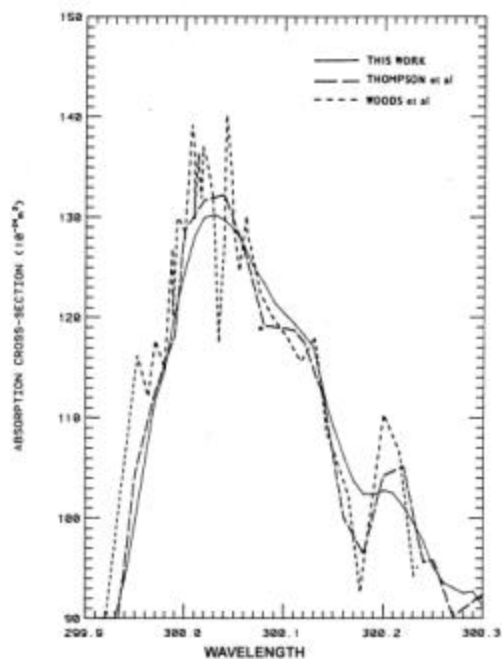


Figure 3.4. Comparison of measurements between Brassington, Thomson et al. and Woods et al. for the 300.03nm absorption peak. (From: Brassington, 1981)

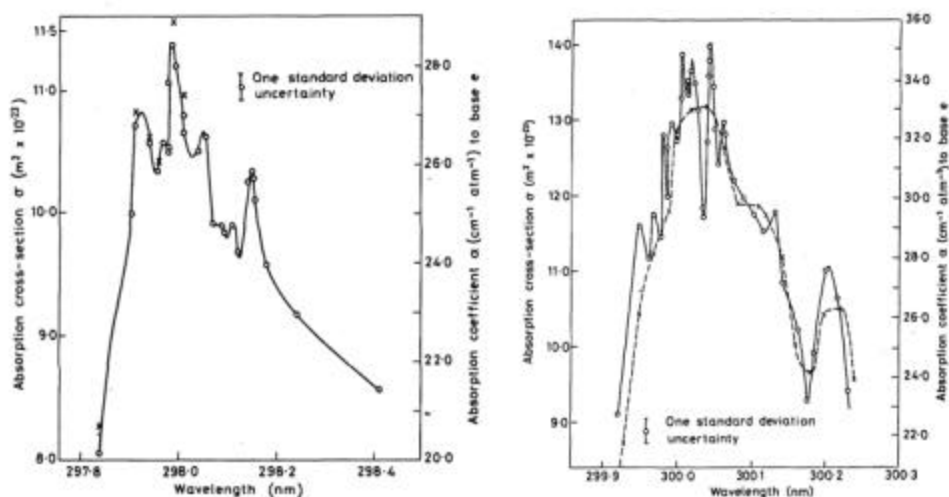


Figure 3.5. High precision  $\text{SO}_2$  absorption cross-section peaks at 298 and 300 nm at  $20^\circ\text{C}$ . The dotted line is with  $1.01 \times 10^5$  Pa of nitrogen buffer gas. The solid line is for  $\text{SO}_2$  alone. The original article refers to the solid line as the one with the buffer gas and the dotted as  $\text{SO}_2$  alone, but this is obviously opposite since the buffer gas smooths out the spectral details. (From: Woods et al., 1980).

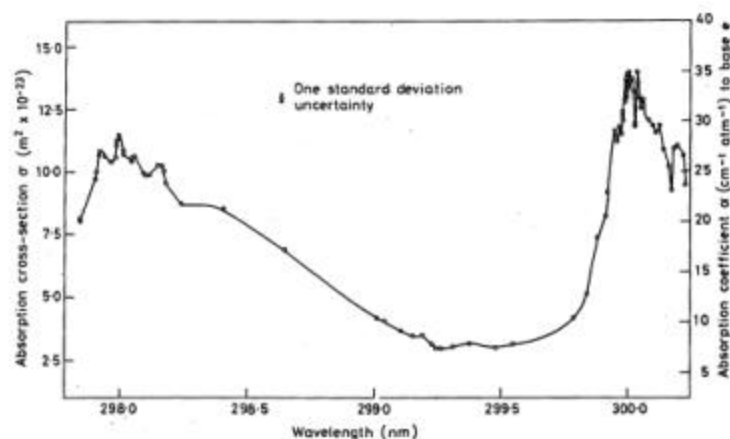


Figure 3.6. High resolution absorption cross section of  $\text{SO}_2$  at  $20^\circ\text{C}$  with nitrogen buffer gas over the spectral region 297.8–300.3 nm. (From: Woods et al., 1980)

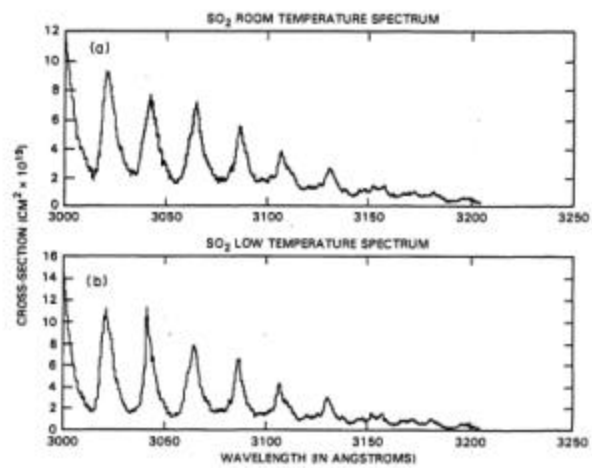


Figure 3.7. SO<sub>2</sub> absorption cross section for (a) 295 K and (b) 210 K. (From: Thomas et al., 1987)

## **IV. UV REMOTE SENSING OF VOLCANIC SO<sub>2</sub>**

### **A. GENERAL**

Volcanic gases are a fundamental part of volcanic activity. Ranging from dramatic emissions of acidic vapors released by highly active volcanoes to invisible emanations through soils, volcanic gases play an important role in influencing the behavior of a volcano. Quantitative information on volcanic emissions is essential to studies of climate change, volcanic processes and natural hazards.

Each year volcanic eruptions inject significant but variable amounts of ash and gases into the atmosphere, which may encircle the globe for weeks after an eruption endangering aircraft and affecting the weather. The conversion of SO<sub>2</sub> to sulfate aerosols impacts stratospheric chemistry and the global climate. Volcanoes are by far the largest contributor of stratospheric sulfate aerosols. The presence of aerosols increases the atmospheric albedo, reflecting solar radiation, absorbing terrestrial infrared radiation and modifying the greenhouse effect in the atmosphere. Aviation is also affected by these emissions because jet engines and avionic systems fail in flight when volcanic ash is ingested and longer term damage results from exposure to sulfuric acid aerosols, including the crazing of aircraft windows, fading of polyurethane paint and accumulation of sulfate deposits in jet engines. By studying gases, volcanologists gain insight into a number of volcanic processes, and by studying long-term gas data along with other types of data, try to forecast eruptive activity.

### **B. TOMS**

The presence of ozone (O<sub>3</sub>) in the earth's atmosphere was originally postulated to explain the cutoff of solar radiation reaching the ground at UV wavelengths. Subsequently the region from 300 to 340nm, where strong ozone spectral signature exists, became the standard for measurements of column ozone amounts with ground and spaceborne instruments (Krueger et al., 2000). The best long-term global dataset of atmospheric ozone was collected by the Total Ozone Mapping Spectrometer (TOMS) onboard the Nimbus-7 satellite. TOMS provided global ozone data almost every day

from October 1978 to May 1993 from a low earth polar orbit. The instrument operated by comparing incident solar radiation with radiation reflected from the earth's atmosphere. Six UV wavelengths were observed, each with a bandwidth of 1nm: 313, 318, 331, 340, 360 and 380nm (<http://daac.gsfc.nasa.gov>).

UV remote sensing of volcanic clouds from space began with the discovery that  $\text{SO}_2$ , in the 1982 El Chichon eruption clouds, could be mapped with TOMS. During the eruption, ozone levels were observed to be anomalously high, until it was realized by Arlin Krueger and his colleagues at NASA, that TOMS was detecting volcanic  $\text{SO}_2$  in addition to ozone. Ozone and  $\text{SO}_2$  have similar absorption spectra in parts of the wavelength region where TOMS operates, as shown in figure 4.1, with  $\text{SO}_2$  producing stronger absorption at the shortest TOMS wavelengths (300-320nm).

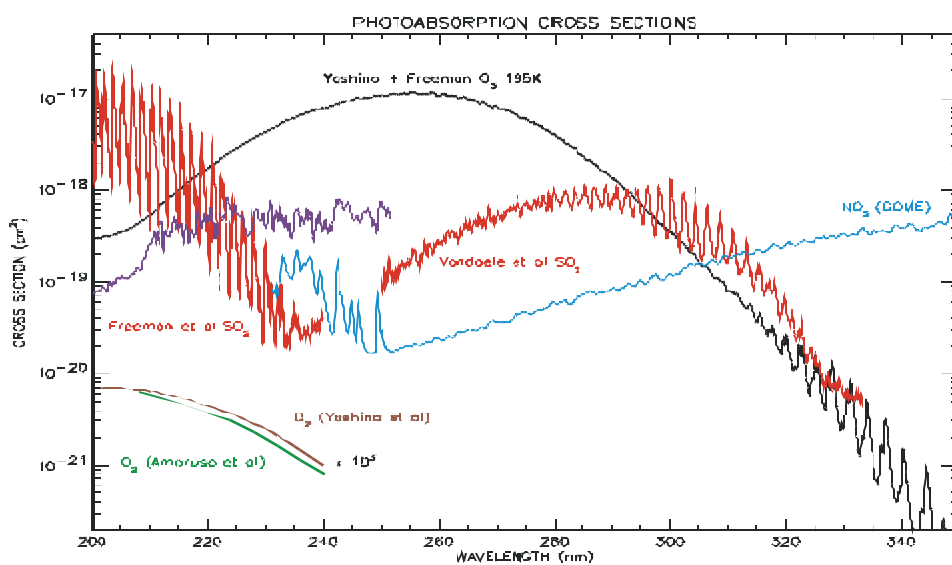


Figure 4.1. Absorption cross sections of atmospheric UV absorbers. (From: Strickland, 1999)

Normally the background amounts of  $\text{SO}_2$  are so small that they can be neglected in ozone data processing. However, the great abundance of  $\text{SO}_2$  in explosive eruption clouds can overwhelm the absorption by ozone causing large errors in the ozone retrievals. This was first observed in 1982 as mentioned previously, and led to the



development of new algorithms to separately determine ozone and  $\text{SO}_2$  in volcanic clouds. The spatial resolution of TOMS is 50km at nadir. Thus, volcanic clouds that extend from less than 50km to many thousands of kilometers can be measured (Krueger et al., 2000). An example of  $\text{SO}_2$  detection by TOMS shown in figure 4.2 is the volcanic cloud created after the eruption of Mt. Pinatubo in the Philippines. The units in the figure are Dobson Units (DU):  $1\text{DU}=1\text{matm}\cdot\text{cm}=10\text{ppm}\cdot\text{m}$ .

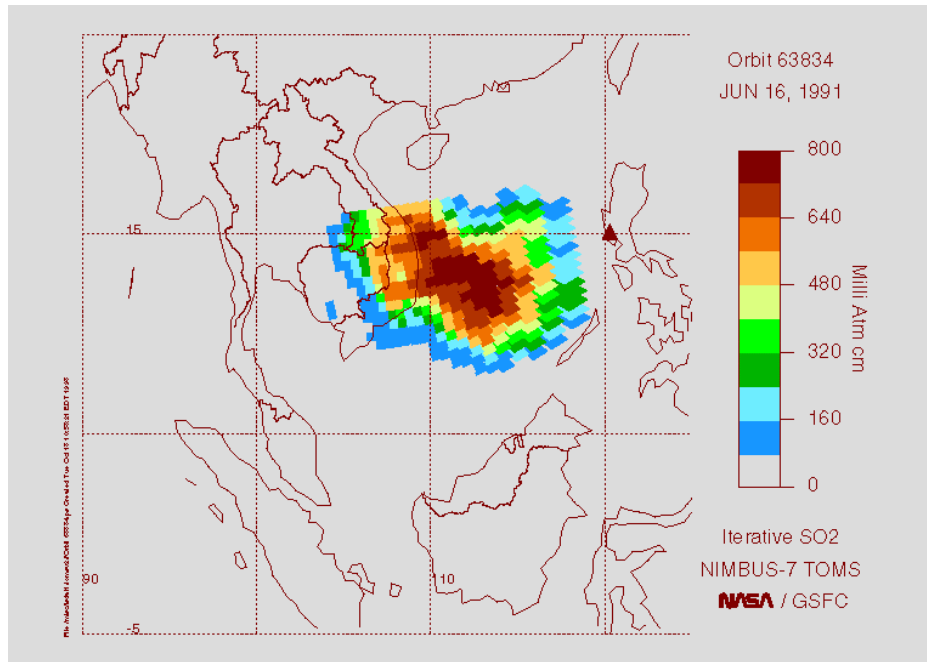


Figure 4.2. False-color image of  $\text{SO}_2$  from the June 16, 1991 eruption of Mt. Pinatubo, Philippines, produced from TOMS data. The triangular symbol marks the location of the source volcano. (From: <<http://skye.gsfc.nasa.gov>>, 2002)

Table 4.1 below shows the satellite missions with TOMS instruments. Earth Probe TOMS is currently the only NASA spacecraft in orbit specializing in ozone retrieval.

Satellite	Launch/ Activation Dates	Ending Date	Orbit Height, km	LT Ascending Node	Nadir Footprint, km
Nimbus-7	October 24, 1978 November 1, 1978	May 6, 1993	955	11:30 AM	50
Meteor-3/5	Aug 15, 1991 Aug 22, 1991	December 24, 1994	1200	Not Sun- synchronous	62
TOMS Earth Probe	July 2, 1996 July 17, 1996	Operating, July 1999	500 (Launch- September 1997)	11:30 AM	24
			739 (November 1997 -present)		39
ADEOS	August 17, 1996 September 11, 1996	June 30, 1997	797	10:30 PM	42
TBD platform	2002				

Table 4.1. Satellite missions with TOMS instruments. (From: Krueger et al., 2000)

### C. BREWER SPECTROMETER

The Brewer spectrometer (see figure 4.3) is a ground based UV spectrometer designed for automated monitoring of total ozone and SO<sub>2</sub> by measuring the spectral absorption of direct sunlight in five narrow bands between 305 and 320nm. In addition, the instrument measures direct and global (direct + diffuse) spectral irradiance in the wavelength range from 290 to 372nm. If direct sun is available, total ozone is derived from direct sun measurements. For cloudy sky conditions, ozone may be derived from scattered UV radiation from the zenith direction. The center wavelengths for the 5 UV channels are 306.3, 310.1, 313.5, 316.8 and 320.1nm.

Successful measurement of column SO<sub>2</sub> amounts in volcanic clouds depends on a chance passage of the cloud over a station. One of the few cases in which this occurred was when the Mt. Spurr, Alaska cloud crossed over Toronto on September 19, 1992. A Brewer spectrometer was looking up at the plume and allowed both the Nimbus-7 and Meteor-3 TOMS instruments to be directly compared with ground observations.

An example of the output produced by the Brewer station of Montreal, Canada is shown in figure 4.4. The graph shows daily mean total ozone values (in Dobson Units) as a function of the season. The results of the most accurate Brewer direct sun measurements are shown in red. All other types of data are shown in blue. The green line indicates total ozone values smoothed by a one month running mean. The dashed lines represent the “normal”, pre-1980 total ozone annual cycle and two standard deviations envelope for daily mean total ozone (From the World Ozone and Ultraviolet Radiation

Data Center (WOUDC)). If a volcanic  $\text{SO}_2$  cloud happens to pass over the station, these data are modified due to the additional absorption and  $\text{SO}_2$  quantitative calculations can be made.



Figure 4.3. Brewer Station on the roof of the Environment Canada Building, Toronto.  
(From: <<http://www.ns.ec.gc.ca>>, 2002)

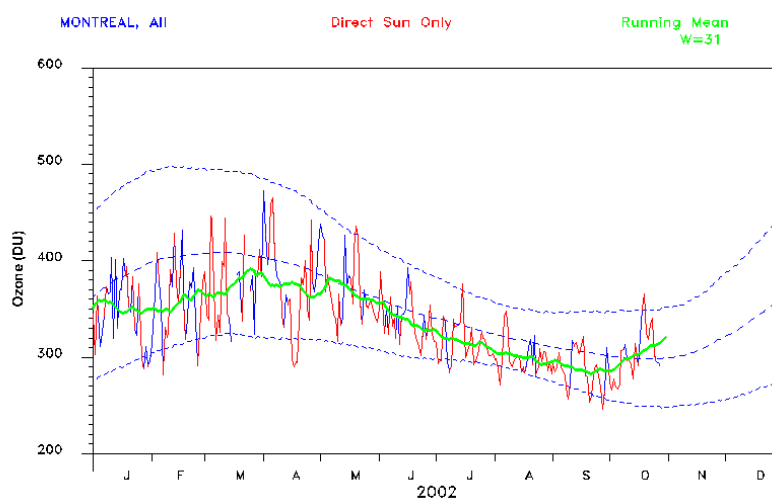


Figure 4.4. Example of Brewer station output. (From: WOUDC, 2002)

#### D. COSPEC

COSPEC (see figure 4.5) is an instrument developed in the 1960s by Barringer Research, a company in Toronto, Canada, to measure emissions of  $\text{SO}_2$  from industrial stacks for pollution monitoring purposes. Volcanologists quickly realized the potential of COSPEC since volcanoes are essentially natural smokestacks. It was first used in 1971 at Mt. Mihara in Japan and then usage spread around the world providing a collection of data that has been used to estimate a worldwide  $\text{SO}_2$  flux (emission rate) from volcanoes.

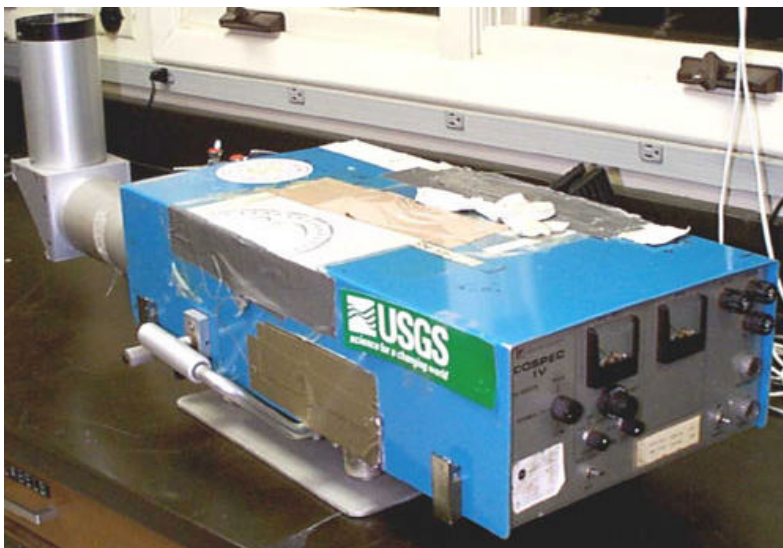


Figure 4.5. Close-up view of COSPEC. (From: USGS website, 2002)

##### 1. Brief Description of Instrument and Its Operation

The instrument operates in the UV region of the spectrum using scattered UV radiation from the sky. The UV sensor has an effective spectral range of 280-320nm but the instrument is usually operated from 300 to 315nm. Its operation is based on the principles of correlation spectroscopy and its internal design is illustrated in figure 4.6. Radiation is gathered by the telescope with a field of view of 23 milliradians by 7 milliradians (1.318 by 0.401 degrees). The collected radiation is focused on a diffraction grating, which separates the radiation into individual wavelengths. This radiation is focused on the rotating correlator disk, which has four sets of seven narrow slits (four

masks) engraved on it. The rotation sequentially places the slits so that they coincide approximately with the peaks and troughs of the  $\text{SO}_2$  absorption bands. This modulated radiation is monitored by the photomultiplier tube and the resulting voltages are processed by the electronics. The ratio between the two sets of incoming radiation ( $\text{SO}_2$  peaks and troughs) is known when no  $\text{SO}_2$  is present to absorb energy. When  $\text{SO}_2$  is

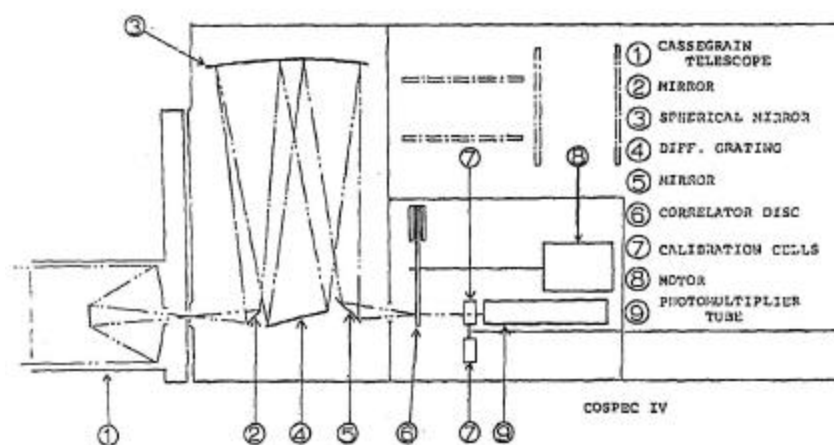


Figure 4.6. Internal design of COSPEC. (From: COSPEC IV Manual, 1976)

present, one set of the slits (corresponding to the troughs) loses energy, and thus, the ratio changes. These changes are electronically processed to yield an output voltage, which is a function of the concentration times the pathlength (optical depth) of the  $\text{SO}_2$  within the field of view of the device (Millan et al., 1976 and Stoiber et al., 1983). The instrument is connected to a data logger or portable computer, which records the output in digital format and an analogue paper chart recorder, which plots the voltage recordings that correspond to a real time  $\text{SO}_2$  profile for the area covered by the sensor. An example of the paper chart recorder output is shown in figure 4.7. The instrument response is calibrated by the rotation of cells, which contain known  $\text{SO}_2$  concentrations, into the optical path. Frequent calibrations indicate the amount of instrument drift.

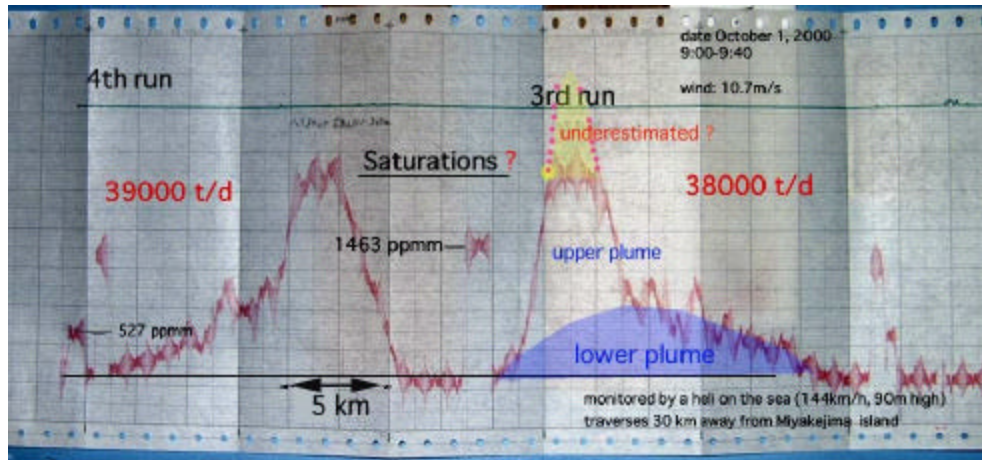


Figure 4.7 Example of COSPEC output to a paper chart recorder. (From: <http://www.gsj.jp>, 2002)

## 2. Calculations and Limitations of the SO<sub>2</sub> Flux Determination

The initial SO<sub>2</sub> absorption profile is converted from volts to an average concentration path length in parts per million-meter (ppm-m). One ppm-m of SO<sub>2</sub> is equivalent to one cubic centimeter of SO<sub>2</sub> gas uniformly mixed in one million cubic centimeters of air that is viewed by COSPEC over an optical path of one meter at a pressure of 101.325 kPa and a temperature of 20°C (Jones and Stix, 2001). The concentration is multiplied by the width of the plume cross-section and produces a SO<sub>2</sub> cross-section in ppm-m<sup>2</sup>. The cross-section is then multiplied by the speed at which the plume crosses this two dimensional area (usually the wind speed is used) producing the SO<sub>2</sub> flux in ppm-m<sup>3</sup>/sec. Finally this value is converted to metric tons per day (t/d) for convenience in reporting (Stoiber et al., 1983). Detailed information about the calculations can be found among other sources in Mares, [2002]. The SO<sub>2</sub> flux calculation is summarized in table 4.2 and an example of the final product, - SO<sub>2</sub> emission rate in tons per day for the Kilauea Summit, Hawaii - is shown in figure 4.8 below.

COSPEC Output :	ppm.m
Plume Width :	m
Plume Speed :	m.s <sup>-1</sup>
COSPEC Output x Width of Plume = SO <sub>2</sub> Plume Cross-Section	
ppm.m x m	= ppm.m <sup>2</sup>
SO <sub>2</sub> Plume Cross-Section x Plume Speed = SO <sub>2</sub> Flux	
ppm.m <sup>2</sup> x m.s <sup>-1</sup>	= ppm.m <sup>3</sup> .s <sup>-1</sup>
Conversion to metric tons.day <sup>-1</sup> :	
(Density of SO <sub>2</sub> gas : 2.86 x 10 <sup>-3</sup> g.ppm <sup>-1</sup> .m <sup>3</sup> ; STP correction factor : 273/293)	
X ppm.m <sup>3</sup> s <sup>-1</sup> x 2.86x10 <sup>-3</sup> g.ppm <sup>-1</sup> .m <sup>3</sup> x 10 <sup>-6</sup> tons.g <sup>-1</sup> x 86,400 s.day <sup>-1</sup> x 273.293	
= Y tons.day <sup>-1</sup>	

Table 4.2. Calculation of SO<sub>2</sub> flux from COSPEC output. (From: Stoiber et al., 1983)

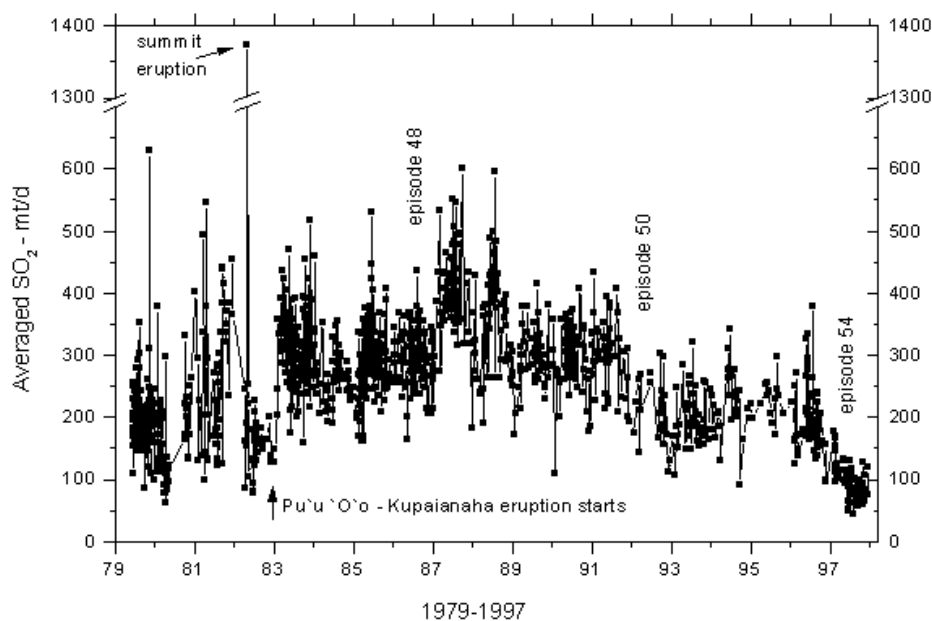


Figure 4.8. Example of long-term COSPEC calculation results in metric tons/day (mt/d) of SO<sub>2</sub> Kilauea Summit, Hawaii SO<sub>2</sub> emission rates. (From: Elias et al., 1998)

The estimation of the error in the SO<sub>2</sub> flux calculations by Stoiber et al. is presented in table 4.3. An example of flux calculation together with estimated uncertainties for Kilauea's east rift zone, Hawaii is shown in figure 4.9.

Data :		
Calibration Cell Concentrations :	$425 \pm 12 \text{ ppm.m}$	$\pm 3 \%$
Chart Record Reading Error :	$\pm 0.5 \text{ mm}$	
(0.5 mm = 6 ppm.m)		
For an average deflection of 100 ppm.m		$\pm 6 \%$
Distance Determination Error		$\pm 5 \%$ to $\pm 10 \%$
Windspeed determination		
(generally)		$\pm 10 \%$ to $\pm 20 \%$
(worst case)		$\pm 40 \%$
Total Error : (square root of the sum of the squares)		
Generally :		$\pm 13 \%$ to $\pm 23 \%$
Worst Case :		$\pm 42 \%$

Table 4.3. Limitations of the COSPEC calculations. (From: Stoiber et al., 1983)

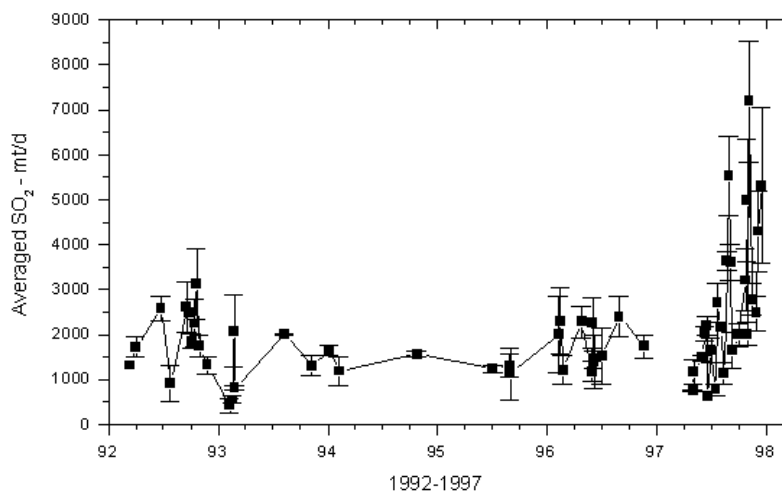


Figure 4.9. Example of estimated uncertainties of SO<sub>2</sub> flux calculations based on vehicle-mounted COSPEC. The black vertical bars represent the standard deviation of all traverses on a single day. Kilauea's East Rift Zone, Hawaii. (From: Elias et al., 1998)

The uncertainty of wind speed is the largest source of error, which increases with the variability of the wind at low wind speeds. Other factors affecting the quality of the COSPEC data and calculations (Millan et al., 1976 and Stoiber et al., 1983) are the following:

- Due to weather conditions (mainly shear winds) the plume profile may be different than the Lagrangian and Eulerian profiles assumed in order to derive the methodology used for the calculations.



- The time of day that the measurements are taken. Since scattered solar radiation is used as the source, early or late in the day measurements are affected by the lower levels of UV radiation, which result in a decreased signal to noise ratio, and thus, the precision of the measurements is reduced.
- The lack of light due to weather conditions (clouds, fog, etc.).
- The presence of volcanic ash in the plume does not allow complete transmission of UV radiation, resulting in a reduction in the measured  $\text{SO}_2$  flux from the actual value.
- The target gas signal is diluted by the radiation scattered by the atmosphere and condensed water vapor into the field of view from outside the solid angle, which collects radiation observed by the sensor. This effect depends on the distance of the instrument from the plume and the width of the plume. For example, when one views a vertical plume, as from a stack or volcano with the COSPEC at a ground point some distance away, the signal may decrease as much as 60% at a distance of only 500m from the crater, if the  $\text{SO}_2$  concentration path-length is 1000ppm-m and the meteorological range is 9.8km (Stoiber et al., 1983). If a plume is viewed from below and it is wider than the vertical distance between the sensor and the bottom of the plume, all the UV radiation reaching the COSPEC comes through the plume. Except for the edges of the plume, this radiation is not scattered into the field of view of the sensor from the outside.

### **3. $\text{SO}_2$ Flux Measurement Techniques Using COSPEC**

There are three standard techniques of collecting data on volcanic plumes with COSPEC: airborne, ground mobile, and ground stationary (see figures 4.10 and 4.11). COSPEC has also been used on a boat. Each technique has advantages and disadvantages depending on the location, access to it, surrounding terrain, plume size, shape and altitude, cost and availability of airplanes etc. In the first two techniques, COSPEC is mounted on an airplane or vehicle that makes traverses beneath the gas plume, with the traverses oriented perpendicular to the direction of the plume. The preferred technique is with an airplane equipped with a good navigation system, since much data can be obtained in a short period of time and plumes that cannot be accessed by other means can be measured (Stoiber et al., 1983).



Figure 4.10. COSPEC mounted on vehicle. (From: <<http://www.volcanoes.ca>>, 2002)

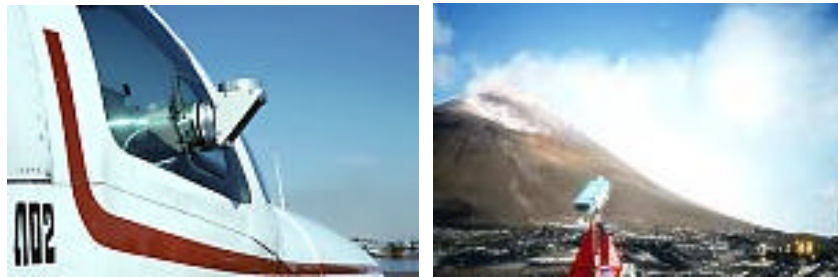


Figure 4.11. COSPEC on airplane and on ground. (From: USGS website, 2002)

The ground stationary technique will be presented here, since it is similar in concept with the one used with LINUS. It involves mounting COSPEC on a tripod either directly under or off to the side of the plume. If COSPEC is under the plume, then the instrument is aligned with the plume axis and a right-angle mirror/rotator is attached to the telescope. The mirror is then rotated through a series of angles until the whole width of the plume has been scanned. When the COSPEC is to the side of the plume, the goniometer head on the tripod can be used to scan the COSPEC through a vertical angle if the plume is horizontal or a horizontal angle if the plume is vertical as it leaves the volcano (Stoiber et al., 1983).

The ground stationary technique probably produces the least reliable data because varying plume geometries often make calculations difficult and large and variable path-lengths from the plume cause variable signal attenuation due to scattering, thus affecting the measured SO<sub>2</sub> flux. However, this technique is the only one, which can be applied under certain circumstances, such as at volcanoes where there is no effective air or ground access (Stoiber et al., 1983). A comparison between the vehicle and tripod-based measurements of the Kilauea Volcano, Hawaii from 1995 to 1997 showed that the vehicle-based measurements were 1.3-2 times greater than the tripod-based. That discrepancy was attributed to a combination of factors including multiple degassing sources, plume thickness and geometry, distance from the measurement site to the plume and instrument configuration. It was concluded that the tripod-based data, although they provide important information for the vent activity, should be interpreted with care and the best estimate of SO<sub>2</sub> emission rates was provided by the vehicle-based technique (Elias et al., 1998).

#### **E. FLYSPEC**

FLYSPEC is a sensor currently under development by Keith Horton, Assistant researcher at the Hawaii Institute of Geophysics and Planetology. It is essentially a miniature COSPEC (its name emphasizes its size in comparison to COSPEC) that takes advantage of new spectrometer and computing technology. Apart from the reduced size of FLYSPEC, other differences with COSPEC are the lower cost of the device, reduced data processing time and real data analysis capability. Although no formal literature is currently published, details about the design and operation of the device can be found in Mares, 2002. Figure 4.12 shows COSPEC and FLYSPEC mounted on the same vehicle, figure 4.13 shows some sample data collected by FLYSPEC at the Kilauea volcano, Hawaii in March 2002 and figure 4.14 shows a comparison between COSPEC and FLYSPEC data taken concurrently at the same site.

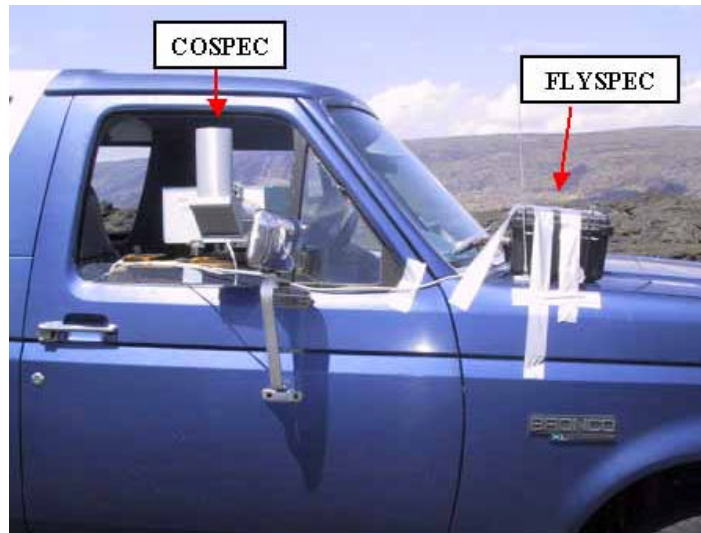


Figure 4.12. Concurrent data collection with COSPEC and FLYSPEC. (From: Mares, 2002)

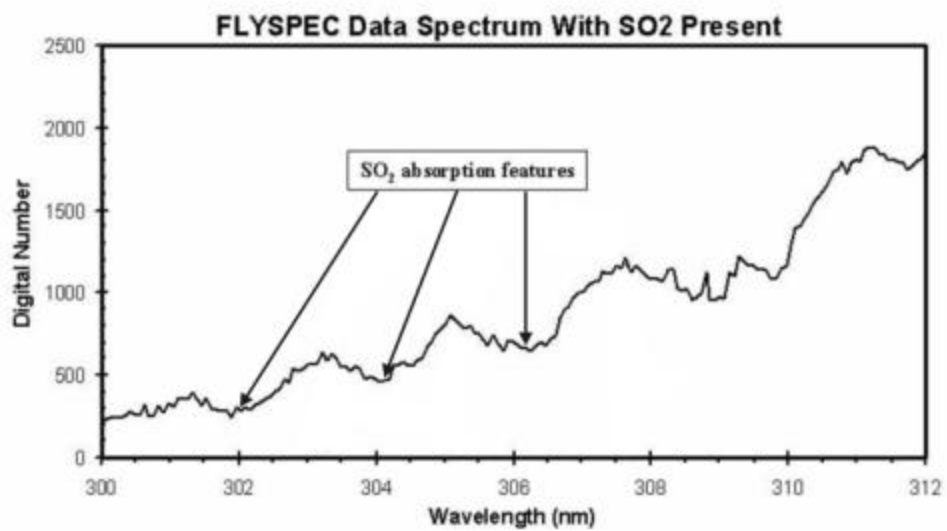


Figure 4.13. FLYSPEC sample data frame collected at Kilauea Volcano, Hawaii in March 2002. (From: Mares, 2002)

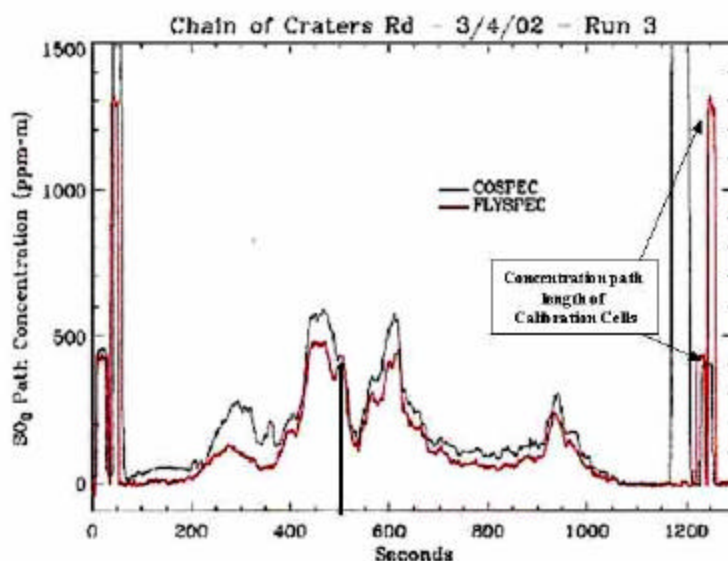


Figure 4.14. Comparison between COSPEC and FLYSPEC data taken concurrently in March 2002 at Kilauea Volcano, Hawaii. (From: Mares, 2002)

## F. SUMMARY

TOMS is a spaceborne instrument that allows detection and quantification of large-scale  $\text{SO}_2$  emissions during volcanic eruptions. The results depend on the algorithms used to extract the  $\text{SO}_2$  information from the raw data. TOMS  $\text{SO}_2$  data led to significant advances from determining eruptive emission rates to tracking of individual clouds and assessing global volcanism and atmospheric impacts.

The ground-based instruments can only locally detect and quantify  $\text{SO}_2$  emissions and their accuracy greatly depends on weather conditions and especially wind direction and velocity. They use scattered UV radiation except for the Brewer spectrometer, which uses direct sunlight when there are no clouds. Brewer spectrometers are stationary instruments mainly used to measure ozone in the atmosphere and they can only measure volcanic  $\text{SO}_2$  by chance, if the weather conditions bring a volcanic cloud over the Brewer station. COSPEC and FLYSPEC are mobile instruments, which can be mounted on vehicles or aircraft that have to pass under the plume, or they can be used stationary on the ground at a site. COSPEC has a 30-year history of  $\text{SO}_2$  observations, has produced a

large collection of data and is the main ground based instrument in use today. FLYSPEC is a new instrument still under development, based on the same principles as COSPEC but takes advantage of new technologies in order to be smaller, faster and cheaper than its predecessor. Figure 4.15 below summarizes the data collection techniques for UV remote sensors while figure 4.16 shows the wavelength region in which they operate.

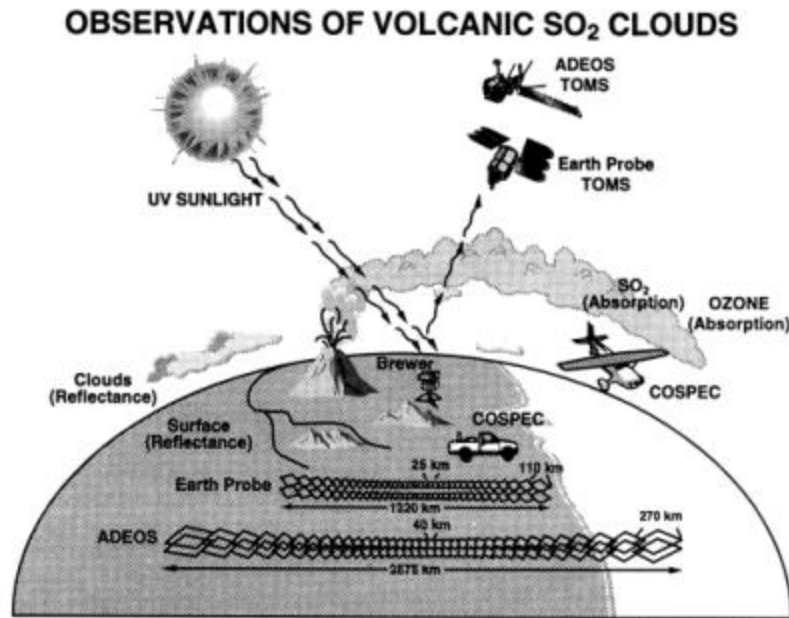


Figure 4.15. UV sensors used in the detection of volcanic SO<sub>2</sub>. (From: Krueger et al., 2000)

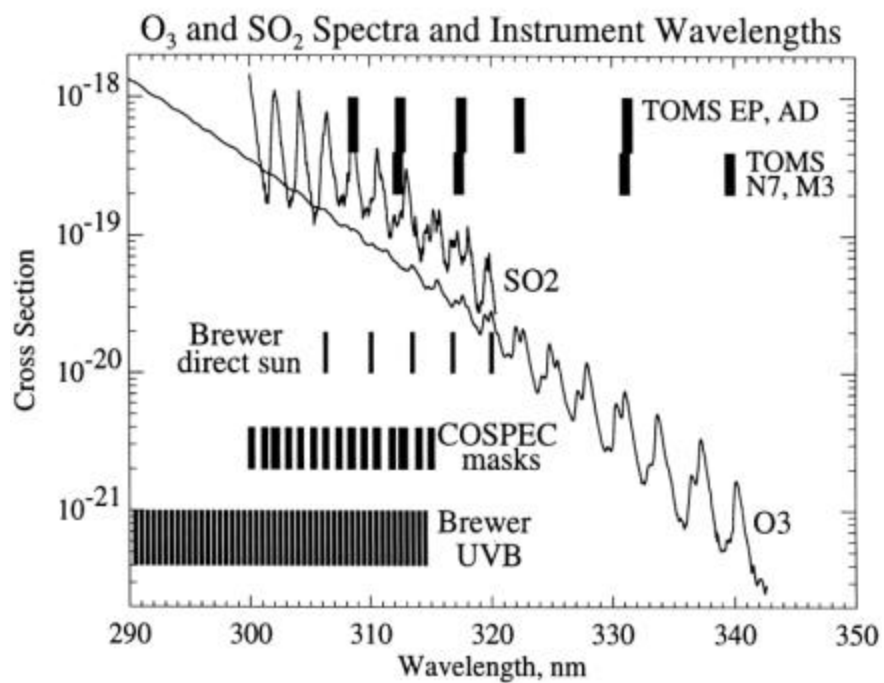


Figure 4.16. Absorption spectra of SO<sub>2</sub> and O<sub>3</sub> and wavelength bands used by the UV detectors. (From: Krueger et al., 2000)

THIS PAGE INTENTIONALLY LEFT BLANK



## V. LINEATE IMAGING NEAR ULTRA VIOLET SPECTROMETER (LINUS)

### A. GENERAL

LINUS is a hyperspectral ultraviolet imaging spectrometer designed to study atmospheric gas plumes. It was designed and developed by Professor Scott Davis and his students of the Physics Department at the Naval Postgraduate School.

### B. DEVICE DESCRIPTION AND OPERATION

In order to understand the capabilities of LINUS and the kind of data it can produce, a brief description of the device and its operation is given below. Detailed information about the device can be found in (Kompatzki, 2000) and (Gray, 2002). Elements from the first work are shown below. The architecture of LINUS is shown in figure 5.1.

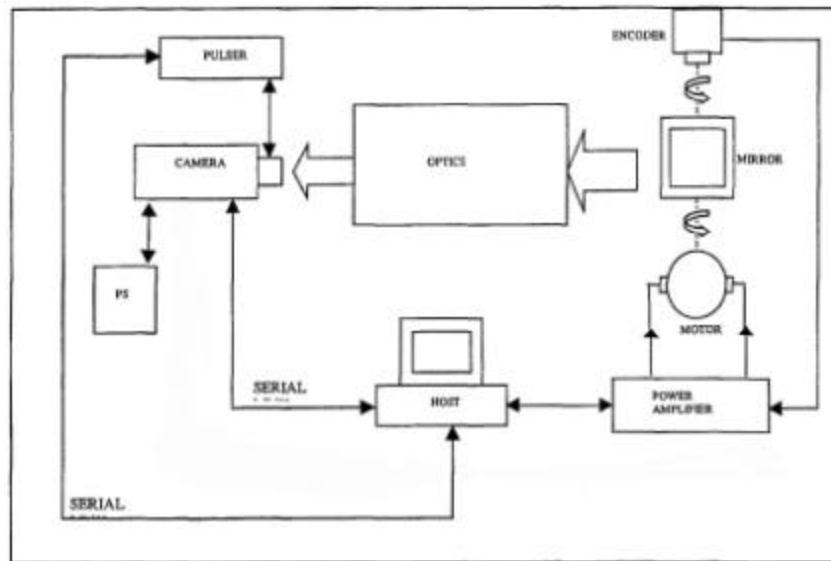


Figure 5.1. LINUS architecture. (From: Kompatzki, 2000)

#### 1. Hardware

LINUS (see figure 5.4) consists of four main subsystems:

***a. Host Computer***

The host computer is the heart of LINUS acting as the main processing, synchronizing and control unit. It is an ICS Advent system composed of a 7490 series chassis, a 14.1" liquid crystal display, keyboard and mouse, all ruggedized for field use. The CPU board is based on an Intel Pentium processor.

***b. Scanning system***

The scanning system performs the optomechanical scanning of the scene. It is a closed loop angular position control system that points the image-scanning mirror to any desirable heading. It consists of the following:

- A National Instruments Flexmotion 6C motion card.
- A 12FS model Kollmorgen Motion Technologies Group high torque low - inertia DC servomotor.
- A R137 model Gurley Precision Instruments digital encoder, which provides position feedback. The encoder has a resolution of 144,000 counts per revolution.
- A National Instruments nuDrive multiaxis power amplifier.
- The scanner mirror assembly which houses the mirror, the DC motor and the encoder.

***c. Camera system***

The camera is a Princeton Instruments Intensified Pentamax System, which consists of an ultraviolet intensified CCD camera, a power supply, a PG-200 pulser with an MCP-100 high voltage power supply and a high-speed serial link board. At the front end of the camera is an integrated, ultraviolet enhanced microchannel plate (MPC) image intensifier. The output of the intensifier is optically connected to a 512x512 charge coupled device (CCD) detector array via a tapered fiber optic bundle. The camera is cooled to a temperature set by the user and its spectral range is 200-550nm. Camera control and data acquisition is accomplished through the host computer, which is connected to the camera through the high-speed serial link.

*d. Optics*

The optical layout of LINUS is shown in figure 5.2. At the front end is the scanner mirror, which is operated by the servo system. The radiation reflected by the mirror passes through a filter, which in the case of the measurements used in support for this thesis, is centered at about 300nm with a spectral response as shown in figure 5.3. After the filter, the primary telescope objective focuses the radiation onto a vertical slit aperture. Then, a collimating lens sends the radiation to a reflective plane diffraction grating, and after been focused by the camera objective, ends up onto the input plane of the camera's image intensifier.

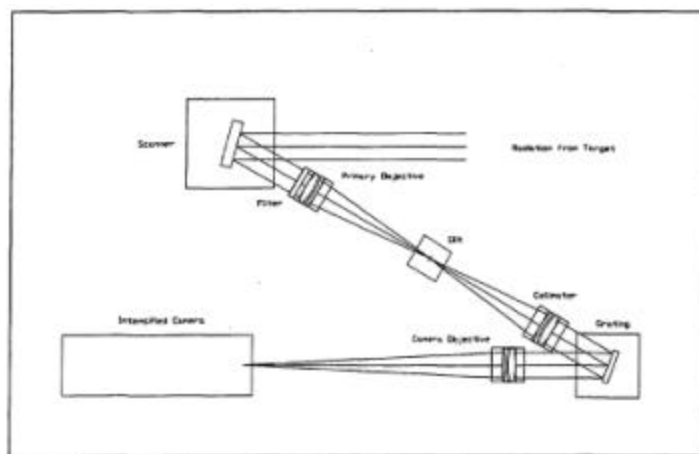


Figure 5.2. LINUS optical layout. (From: Kompatzki, 2000)

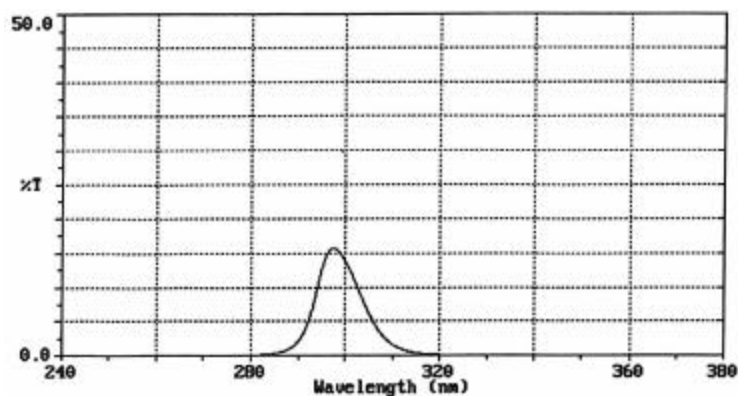


Figure 5.3. Spectral response for the 300nm UV filter. (From: Filter Specs)

## 2. Software

All the software is installed on the host computer and consists of the following main modules:

- Windows NT 4.0 is the operating system.
- LabVIEW 5.1 is used to control the scanning subsystem.
- WinView/32 v2.4 is used for camera control and data acquisition.
- IDL 5.5 and ENVI 3.5 are used for data processing.



Figure 5.4. Pictures of LINUS. On the left side is the electronics section with the computer the amplifier and the camera pulser and cooler. On the right side is the optics section, which also includes the camera body and the scanner mirror assembly.

## 3. LINUS Operation

The scanner mirror is set to a desired position by the stepping program. Light coming through the aperture is reflected by the mirror through the UV filter into the optical section of the device. The filter cuts all wavelengths outside its response region. The radiation is analyzed by the diffraction grating into the constituent wavelengths and is recorded by the camera. The camera output is sent to the host computer for storage and

subsequent processing. Once image acquisition is finished, the mirror is stepped to a new position and the process is repeated until the whole scene is imaged. At the time of data acquisition for this thesis, mirror stepping and image acquisition were done by two separate software applications (LabVIEW and WinView), which required user input. This, in addition to being elaborate and time consuming, results in an image of the whole scene that is extended in time (as much as 20 min), depending on the camera integration time per vertical strip of the scene. Currently, there is a project of integrating mirror scanning and data acquisition under one automated process using LabVIEW.

LINUS's product is a dataset consisting of three components for each pixel, two spatial coordinates and one spectral array. The vertical spatial coordinates (y) along with the spectral components for each horizontal position are recorded and the image is scanned horizontally to cover the scene (see figure 5.5). The data can be thought of as a hyperspectral data cube shown in figure 5.6. The field of view in the vertical direction (y axis) is 0.5 degrees and is recorded in 512 pixels, while in the horizontal direction (x axis) the maximum field of view that can be scanned is 2 degrees, or,  $\pm 1$  degree from the mirror boresight position. The horizontal field of view ( $\theta$ ), imaged at a certain mirror position, depends on the slit width setting and is given by equation 5.1.

$$\theta = 2 \tan^{-1} \left( \frac{w}{2f} \right) \quad (5.1)$$

where  $\theta$  is in radians, w is the slit width and f=25cm is the focal length of the primary objective lens of the optical system (see figure 5.2 above). The number of wavelengths recorded is 512 and the wavelength resolution depends on the diffraction grating and the slit width setting.

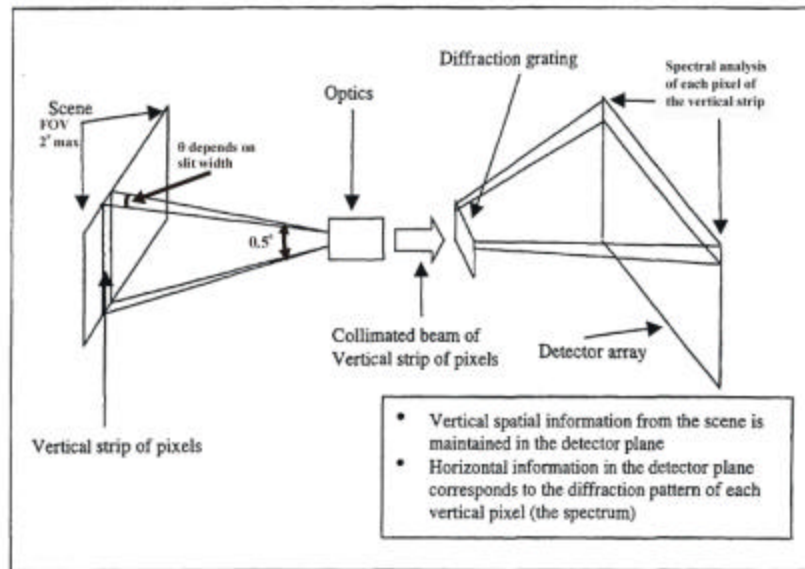


Figure 5.5. LINUS spectral imaging schematic diagram.

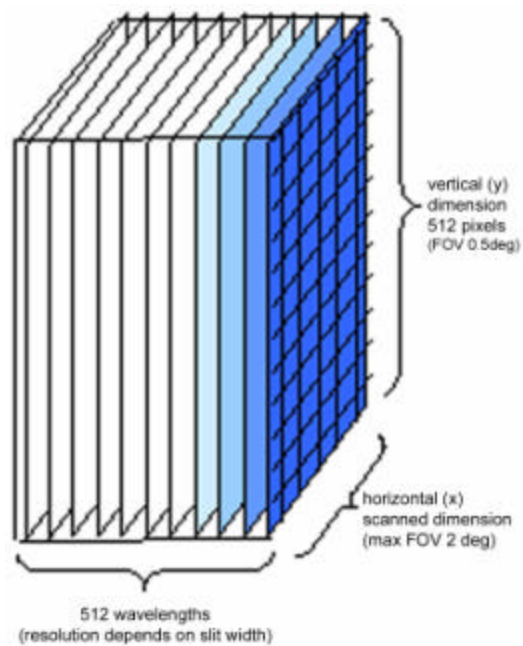


Figure 5.6. Data set produced by LINUS output.

## VI. EXPERIMENTAL DATA COLLECTION

### A. GENERAL

The initial schedule to field test LINUS was for early spring of 2002. Due to component manufacturing and integration delays, the device was not ready until late summer of the same year. The location selected for the first data acquisition was Lassen Volcanic National Park with the main site being the Sulfur Works where sulfuric emissions occur. The Park is located in northern California, USA as shown in figure 6.1 below. The Sulfur Works hydrothermal area (see figure 6.2) is the most accessible hot springs area in Lassen Park and it is thought to be part of the central vent system of ancient Mount Tehama.

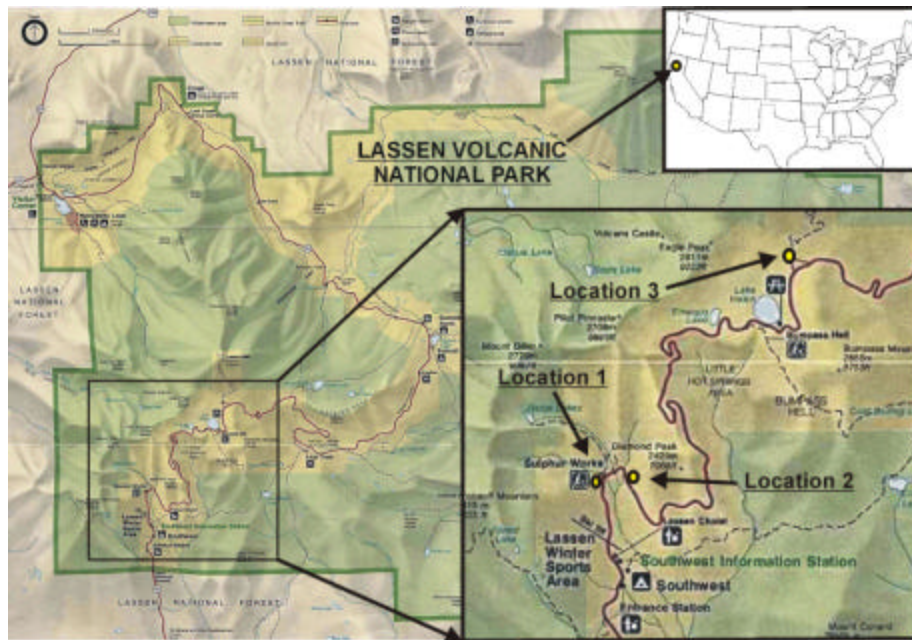


Figure 6.1. Map of Lassen Volcanic National Park. The square on the right is magnification of the area included in the left box. Locations 1, 2 and 3 are the spots where the measurements took place. (After: USGS website, 2002).



Figure 6.2. Some of the Sulfur Works vents.

## **B. BRIEF VOLCANIC HISTORY OF LASSEN PARK**

From 600,000 to 400,000 years ago, ancient Mt. Tehama gradually built up through countless eruptions. Later, this volcano became inactive and eroded away and its main vent was probably what is now the park's Sulfur Works. Lassen Peak began as a volcanic vent on Mt. Tehama's northern flank and was formed by eruptions about 27,000 years ago. It is considered the world's largest dome volcano. After being dormant for 27,000 years, in 1914, Lassen Peak started a seven-year eruptive activity. The most important eruption occurred on May 22, 1915 (see figure 6.3) (From: USGS website, 2002).



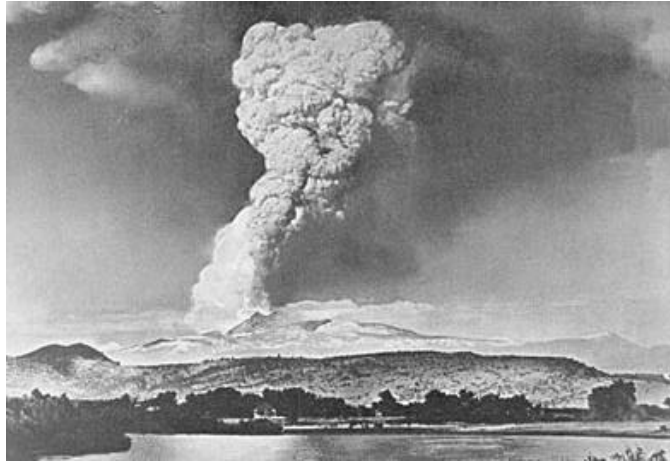


Figure 6.3. The May 22, 1915 explosive eruption of Lassen Peak. (From: USGS website, 2002)

## **C. DATA ACQUISITION**

### **1. First Trip**

The first trip to Lassen took place between 21 and 23 August 2002. Many data sets were acquired and returned back to NPS for evaluation and processing, since there was no capability to process the data on site yet. Evaluation of the data revealed that they were essentially useless, and further investigation showed that the main reason was scanning-mirror alignment problems, probably caused due to transportation of the device. Nevertheless, useful experience was gained regarding the transportation, handling and operation of LINUS in the field.

### **2. Second Trip**

The second trip took place on 13 and 14 September 2002. Evaluation and processing of the data acquired on this trip forms the focus of this thesis. At that time, the capability of scanning across the scene, although available, was not reliable. Thus, most of the images taken were with the mirror in the boresight position.

At the same time that measurements were performed with LINUS, other data were also recorded in a logbook to be used in the subsequent processing of the measurements and modeling with MODTRAN. Those data are:

- Date and time of day (recorded by the computer when saving the images).

- Latitude, longitude and elevation given by a hand-held GPS device.
- Inclination with respect to horizontal and heading of the line-of-sight of the LINUS optical system.
- LINUS optical system and camera settings: slit width, camera MCP voltage and integration time.
- Turn size (in degrees) in the azimuthal direction when the controls of the tripod that supports the optical system were used to perform a “mechanical scan” and step size for the few cases when the stepping program was used to perform a mirror-scan.
- Approximate weather conditions (temperature, wind, clouds) since no instruments were available.
- Other events or observations considered to be significant for the follow -on work (e.g. bad images for specific reasons, etc .).

The weather conditions were ideal for taking measurements during both days, with clear skies, mild winds and an average temperature of about 22<sup>0</sup>C (72<sup>0</sup>F). The measurements took place at locations 1, 2 and 3 as shown on the map in figure 6.1. Due to heavy road construction in the Park, measurements scheduled to take place at two other sites were not possible. The geographical coordinates of the locations are:

- Location 1: 40<sup>0</sup>26.92N, 121<sup>0</sup>32.14W, elevation 6982 ft
- Location 2: 40<sup>0</sup>26.93N, 121<sup>0</sup>32.13W, elevation 6993 ft
- Location 3: 40<sup>0</sup>26.88N, 121<sup>0</sup>31.98W, elevation 8413 ft

On 13 September, LINUS was deployed at location 1 and trial images were acquired to investigate how the device responded to combinations of various inclinations and azimuth angles. Slit width settings, camera MCP voltage settings and image integration times were also varied. Most of the measurements were taken in a NE-E (northeast-east) direction, which at that time, was about 90<sup>0</sup> with respect to the sun’s position, looking over the area where SO<sub>2</sub> was emerging (see figure 6.2).



Figure 6.4. Sulfur Works as seen from location 1.

On 14 September, measurements were taken at locations 2 and 3. At location 2, LINUS had an unobstructed view of the entire Sulfur Works area and the bulk of the data were acquired there (see figure 6.3). There were horizontal scans of about  $180^{\circ}$  in azimuth with the Sulfur Works area at the center ( $\pm 90^{\circ}$ ). The scans were performed manually using the controls of the tripod. The bulk of the data were acquired at a  $20^{\circ}$  inclination angle with respect to horizontal, with the device looking at the sky just above the tree-line.



Figure 6.5. LINUS setup at location 2.

Location 3 was at the parking area below Lassen Peak away from Sulfur Works. The purpose of the measurements there was to acquire clear sky spectra. These will be compared to those from locations 1 and 2 in order to identify expected differences in spectra due to  $\text{SO}_2$  presence in the data from locations 1 and 2 with no or much less  $\text{SO}_2$  at location 3. Images with the input aperture covered were also acquired in order to record the dark response of the device.

Difficulties encountered during the expeditions, which might be useful to mention for the next expeditions, are as follows:

- It was discovered in the beginning that there were minor light leaks into the device through the joints between the housing of the optics section and its removable lid, which provides access to the optics. Although minor, they seemed to affect the data under certain inclination and azimuthal angles (position of the optics system with respect to the sun). The light leaks were fixed on-site using aluminum tape and black felt where necessary.
- Under certain angles of the optics system with respect to the sun, light was reflected into the aperture from part of the aluminum frame that supports it

on the tripod. This was handled by covering the involved portion of the frame with black felt.

- The device is quite bulky and heavy for field use and some parts of it require four people to be handled properly (loading-unloading from the vehicle and setup). It also requires a paved area, so that the transportation vehicle can access it and the device can be deployed.

#### **D. RAW DATA**

During the two days of LINUS deployment, 625 data files were acquired taking up 303Mb of computer memory space. Later, these data were evaluated and analyzed, as described in chapter VIII, in order to find out if there is a SO<sub>2</sub> signature in them and whether this signature can provide quantitative estimates for the gas concentrations. Figure 6.6 shows an example of what the LINUS operators were seeing on the monitor of the device at the time of the data files acquisition. Figure 6.7 is the same as figure 6.6 with the difference that it is pseudocolored in order to get a feeling for the radiation intensity variations along the spectrum. Finally, the lower part of figure 6.8 is the first step in the data file processing, which gives the spectral profile of the recorded image by averaging the middle 256 lines (from 128 to 384 strip numbers). The units are Digital Numbers in all figures.

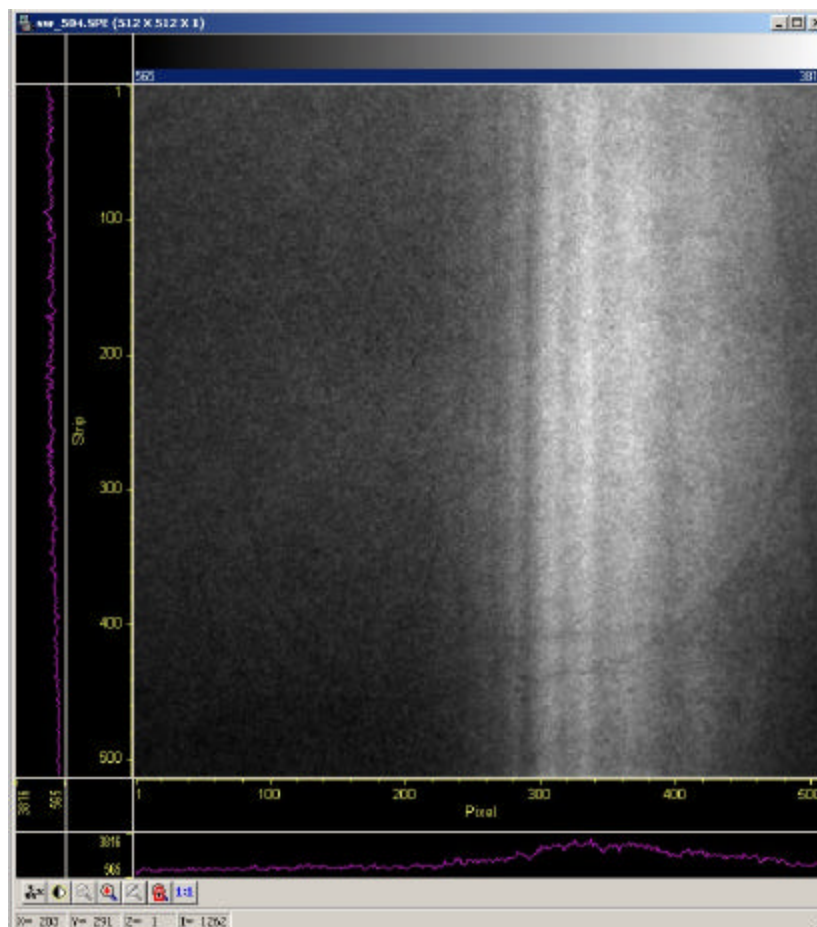


Figure 6.6. Screenshot of LINUS monitor at the time of data file acquisition. This is how the raw data looked like to the operators.

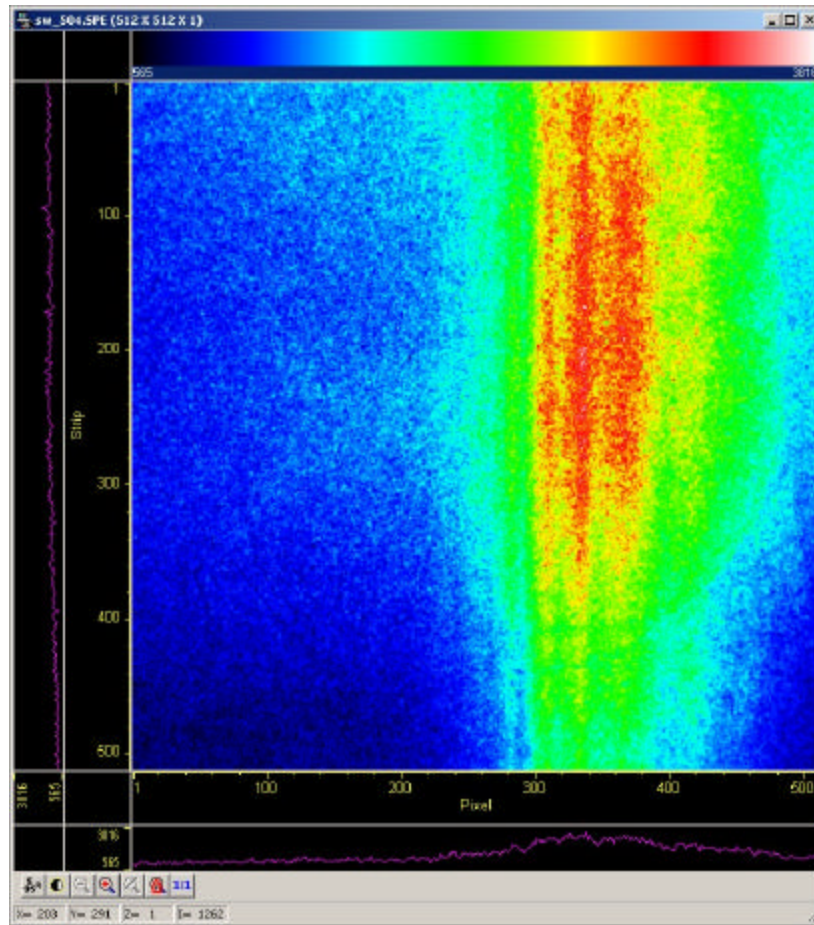


Figure 6.7. The previously presented data file in pseudocolor, which gave to Linus operators a first feeling about the intensity variations along the spectrum contained in the image.

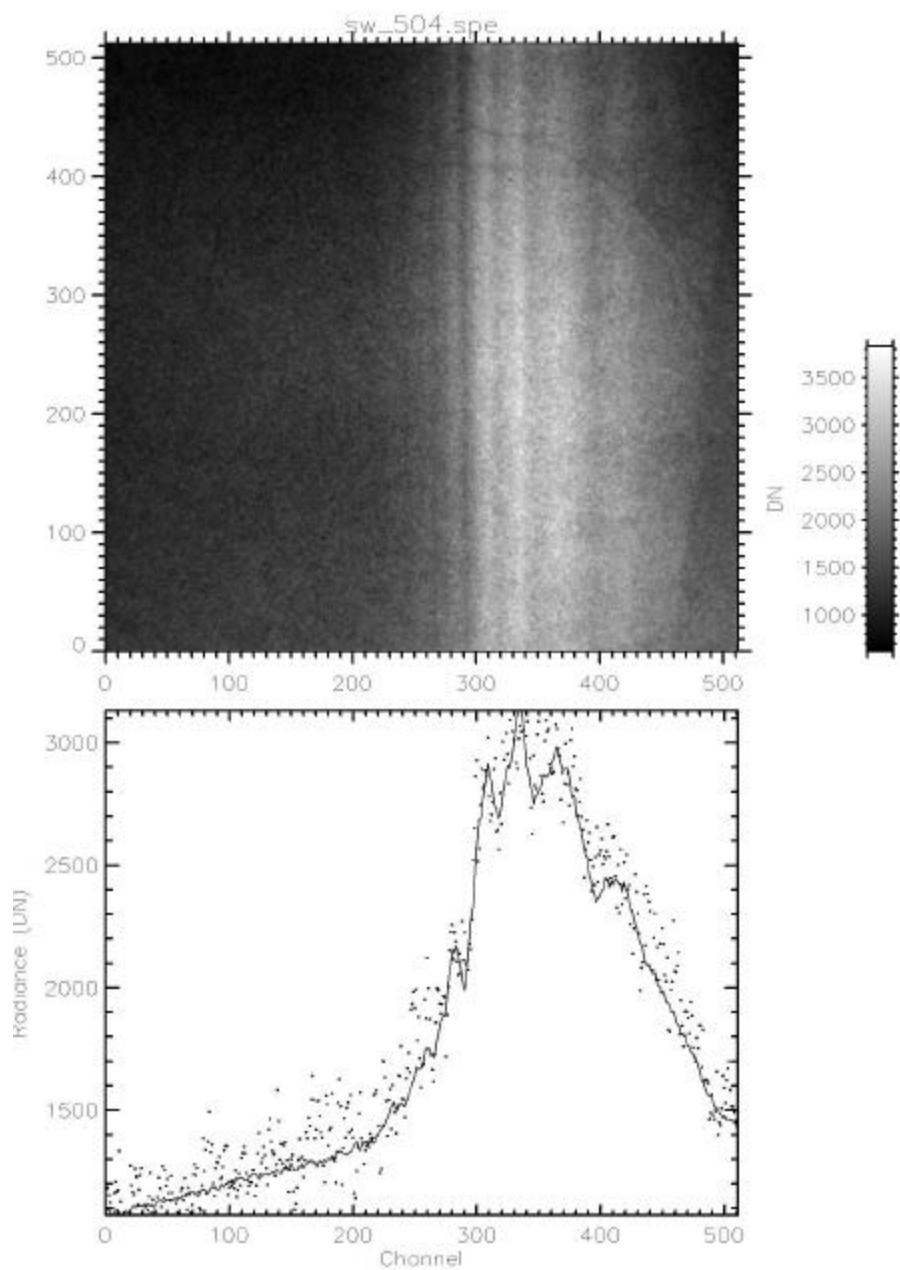


Figure 6.8. A first indication of the spectral profile of the recorded image by averaging the middle 256 lines. Vertical axis units are Digital Numbers (DN).



## VII. MODELING WITH MODTRAN

### A. GENERAL

Apart from collecting and analyzing experimental data using LINUS, it was also decided to simulate the data with a radiative transport model for the following reasons:

- LINUS had never been used in the field before, so modeling would give an indication of how the data should look like in the wavelength-radiance space.
- Processing of the modeled data would provide the SO<sub>2</sub> presence signature that later would be searched for in the experimental data.
- Comparison of modeling with experimental results would facilitate SO<sub>2</sub> detection by LINUS, and if positive, give a quantitative estimate of the gas concentration.

A sample procedure, which can be applied in designing the modeling of electro-optical systems, in this case LINUS, would include the following steps (Anderson et al., 1995):

- Selection of the basic problem – atmosphere as signature or contaminant. Atmosphere is modeled as a signature for this thesis.
- Selection of species, viewing platform, necessary geometric considerations and electro-optical system characteristics to be employed. In our case, the species of interest is SO<sub>2</sub>, and the platform is LINUS operating in the UV with a specific filter response (300 ± 10 nm) and variable viewing geometries.
- Selection of the modeling algorithm for instrument simulation (line by line or band model), based on ease of use and confidence in achieving required accuracy. The algorithm of choice for this case was the band model MODTRAN4.
- Selection and/or design of data analysis schemes and their implementation.

### B. MODTRAN4

In the early 1970's, the then Air Force Cambridge Research Laboratory, initiated a program to develop computer-based atmospheric radiative transfer algorithms. The first product of this program was LOWTRAN (LOW resolution TRANsmittance code), which was released in 1972. This limited initial effort has now progressed to a set of codes and related algorithms, including line-of-sight spherical geometry, direct and scattered

radiance and irradiance, non-local thermodynamic equilibrium etc., that contain thousands of coding lines in hundreds of subroutines with improved accuracy and efficiency. This set of codes includes, among others, LOWTRAN, FASCODE (Fast Atmospheric Signature CODE) and MODTRAN (MODerate resolution atmospheric TRANsmittance and radiance code). Each code relies upon a catalogue of fundamental molecular constants as contained in the HITRAN databases (atlas of high-resolution molecular spectroscopic data) (Anderson et al., 1995).

The model used to simulate LINUS experimental data is MODTRAN4 (Berk et al., 1999). MODTRAN4 is currently the U.S. Air Force standard moderate spectral resolution model for atmospheric transmission, radiance and flux. This radiative transport model extends from the thermal infrared through the visible and into the ultraviolet, covering the spectral region from 0.2 $\mu\text{m}$  to infinity (50,000-0 $\text{cm}^{-1}$ ) (Kneizys et al., 1988). It was developed jointly by Spectral Sciences, Inc. and the Air Force Research Laboratory / Space Vehicles Directorate (AFRL/VS). MODTRAN was first released in 1989 as an attempt to improve the spectral resolution of LOWTRAN 7 (Kneizys et al., 1988) from 20 $\text{cm}^{-1}$  Full Width at Half Maximum (FWHM) with 5 $\text{cm}^{-1}$  calculation increments, to 2 $\text{cm}^{-1}$  FWHM with 1  $\text{cm}^{-1}$  increments (Berk et al., 1989).

MODTRAN and its predecessors have been used extensively over the last quarter century in the design and analysis of broadband, multiband and short-wave IR/Visible hyperspectral imaging sensors. For example, remotely sensed spectral imagery of the Earth's surface can be used to its fullest advantage only when the influence of the atmosphere has been removed and the data are reduced to units of reflectance. This can be achieved with MODTRAN (Adle-Golden et al., 1999).

MODTRAN uses a spherically symmetric atmosphere, consisting of homogeneous layers up to 100km altitude, each of which is characterized by the layer boundary specification of temperature, pressure and atmospheric species concentrations. It uses Snell's law to refract a line-of-sight (LOS) (Acharya et al., 1999). It can use one of the six available geographical-seasonal model atmospheres or a user specified atmosphere. The atmospheric species whose concentrations can be user-defined are shown in the table 7.1 below.

No	Species	Other name
1	water vapor (H <sub>2</sub> O)	
2	carbon dioxide (CO <sub>2</sub> )	
3	ozone (O <sub>3</sub> )	
4	nitrous oxide (N <sub>2</sub> O)	
5	carbon monoxide (CO)	
6	methane (CH <sub>4</sub> )	
7	oxygen (O <sub>2</sub> )	
8	nitric oxide (NO)	
9	sulfur dioxide (SO <sub>2</sub> )	
10	nitrogen dioxide(NO <sub>2</sub> )	
11	ammonia (NH <sub>3</sub> )	
12	nitric acid (HNO <sub>3</sub> )	
13	CCl <sub>3</sub> F	CFC-11
14	CCl <sub>2</sub> F <sub>2</sub>	CFC-12
15	CClF <sub>3</sub>	CFC-13
16	CF <sub>4</sub>	CFC-14
17	CHClF <sub>2</sub>	CFC-22
18	C <sub>2</sub> Cl <sub>3</sub> F <sub>3</sub>	CFC-113
19	C <sub>2</sub> Cl <sub>2</sub> F <sub>4</sub>	CFC-114
20	C <sub>2</sub> ClF <sub>5</sub>	CFC-115
21	ClONO <sub>2</sub>	
22	HNO <sub>4</sub>	
23	CHCl <sub>2</sub> F	
24	CCl <sub>4</sub>	
25	N <sub>2</sub> O <sub>5</sub>	

Table 7.1. Molecular species for user defined atmospheric profiles. SO<sub>2</sub> is number 9.  
(After MODTRAN4 User's Manual, 1999)

### C. SELECTION OF MODTRAN4 INPUT CARDS AND VARIABLE VALUES

Although MODTRAN is an invaluable scientific tool, for the novice user, it is obscure and hard to use. There are hundreds of variables that can be defined by the user, which are only very briefly described in the user's manual (Berk et al., 1999). Furthermore, the user interface is based in the era when the computers were initially developed and the input was given by 80 character input punch cards. Extensive research in the existing literature, MODTRAN documentation and published applications, did not

reveal many details about most of the variables and the effects they have on the output. It seems that in most of the applications slight variations of the standard example input files (called “cases”) provided with the MODTRAN code are used. For the purpose of this thesis, none of the sample input files was satisfactory even with extensive modifications. Thus, a new input file had to be built. In order to understand the effects of certain variable values to the output for this thesis, extensive trial runs had to be performed. Some of the results are presented below, with the purpose of documenting what was done, and helping subsequent users avoid repeating the same procedure.

## **1. Selection of Input Cards**

The input cards used for this modeling case, along with the associated variables and their values, are shown in appendix A. Except for the cards required by the model, there are a number of optional cards that are used to specify the user-defined atmospheric profiles and geometry. In summary, the cards used are:

- Card 1: Main radiation transport driver. Required.
- Card 1A: Radiative transport driver (continued). Required.
- Card 1A2: Spectral data and sensor response function file. Optional.
- Card 2: Main aerosol and cloud options. Required.
- Card 2C: User-defined atmospheric profiles. Optional.
- Card 2C1: User-defined atmospheric profiles. Optional.
- Card 2C2: User-defined atmospheric profiles. Optional.
- Card 3STD: Line-of-sight geometry. Required.
- Card 3A1: Solar/Lunar scattering geometry. Optional.
- Card 3A2: Solar/Lunar scattering geometry. Optional.
- Card 4: Spectral range and resolution. Required.
- Card 5: Repeat run options. Required.

## **2. Selection of Variable Values**

In this section, the values selected for specific variables are discussed. Where it was clear by the problem what the values should be, only a brief justification or description is given. In the cases where it was deemed that further investigation was

needed with trial runs, all the other variables were held constant, with their default or the previously decided values, and the variable in question was changed. For some of these cases, the results of the trial runs will be presented. Examples of specific input files used to simulate Lassen measurements are presented in appendix B.

*a. Card 1*

MODEL=7: It specifies that user-defined atmospheric profiles will be provided in cards 2C, 2C1 and 2C2. These will specify the way the atmosphere will be divided in layers and the temperature and SO<sub>2</sub> concentration of the first layer.

IEMSCT=2: The code has to execute in solar radiance mode in order to model the radiance reaching the sensor.

IMULT=1: The spectral region of interest is in the UV, which is dominated by Rayleigh scattering. Thus, multiple scattering is necessary. Furthermore, the solar geometry at the location of H1 (LINUS latitude and longitude) is needed. Trial runs of the code indicated that with single scattering, radiances are systematically smaller than those with multiple scattering, with the maximum difference in the area of 500nm where the radiance curves have maxima. The effect of single and multiple scattering on the radiance for an extended spectral region is illustrated in figure 7.1 and the ratio of single scattering divided by multiple scattering in figure 7.2. It is obvious that single scattering gives about 85% less radiance than multiple scattering in the spectral region of interest (about 300nm).

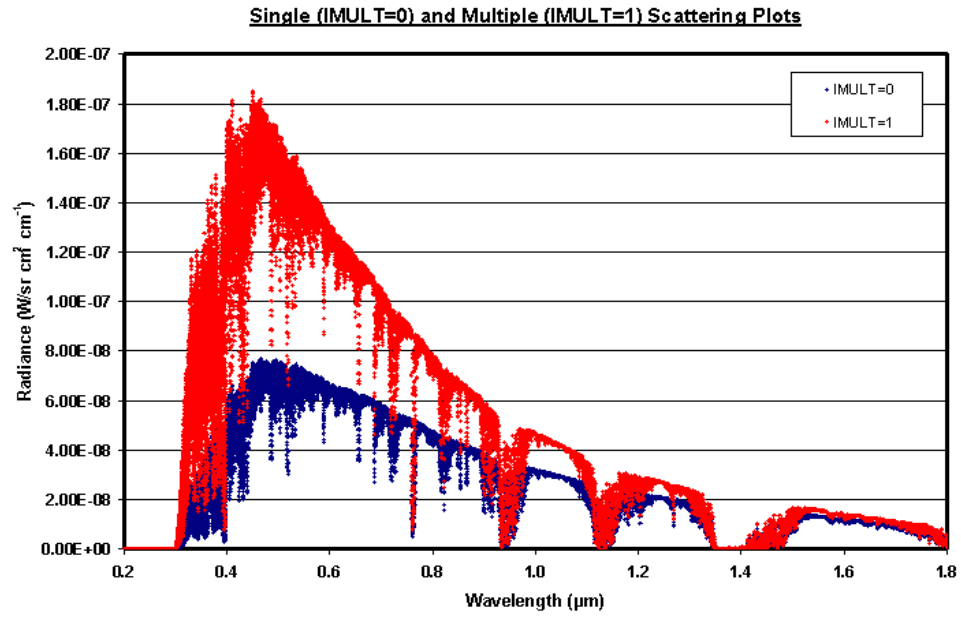


Figure 7.1. MODTRAN results for single and multiple scattering.

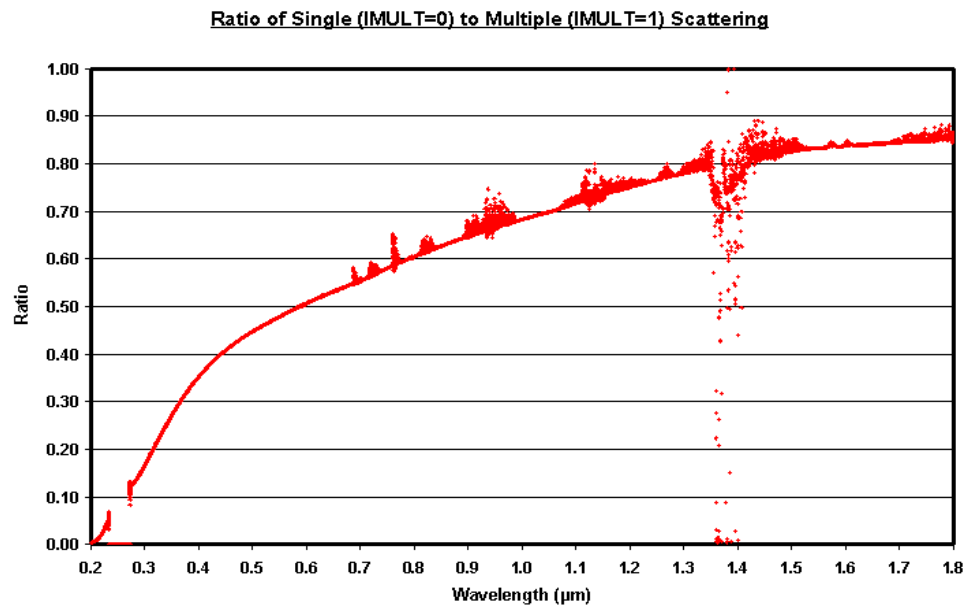


Figure 7.2. Ratio of single divided by multiple scattering from MODTRAN results.

NOPRNT=0: The output files mainly used for information and subsequent processing are the tape6 (TP6) and PLT. If NOPRNT=-1, huge TP8 files are created, which generally are not needed but require a lot of memory.

***b. Card 1A***

DIS=T: This activates the DISORT (DIScrete Ordinate Radiative Transfer) algorithm. This is the best multiple scattering algorithm implemented in MODTRAN4, which together with the following DISAZM and NSTR variables, provide the most accurate results (Acharya et al., 1999). Figure 7.3 shows that, calculations without using the DISORT algorithm deviate from the better calculations involving DISORT, particularly for wavelengths smaller than 292nm. The disadvantage is that its use increases computational time by a factor of 30 or more.

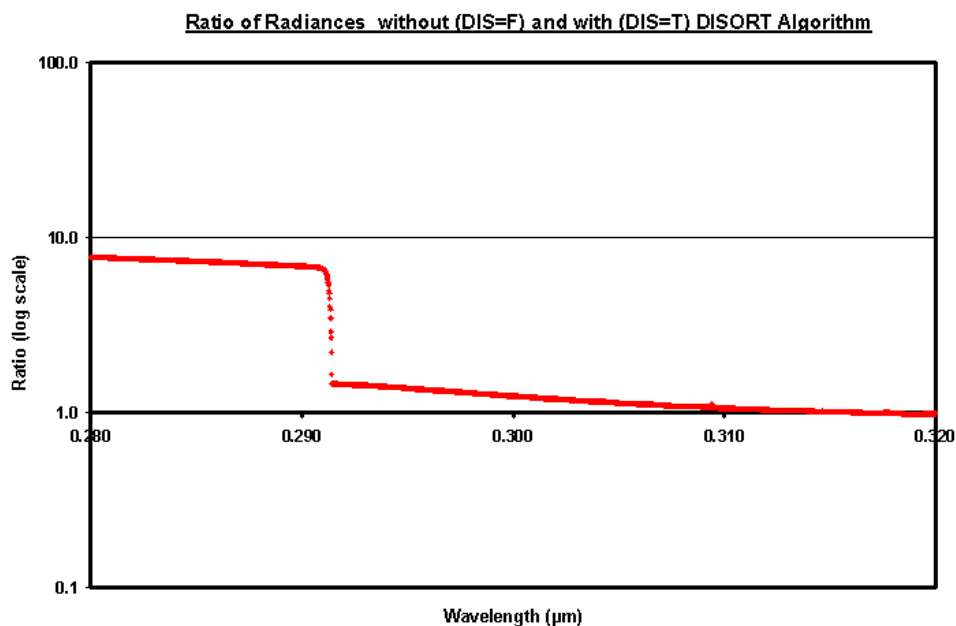


Figure 7.3. Effect of using the DISORT algorithm in the spectral region of interest.

DISAZM=T: Includes azimuthal dependence in the line-of-sight multiple scattering of solar radiation. It is needed since LINUS can scan to various azimuthal directions (headings).

NSTR=8: This is the optimized value recommended by the MODTRAN manual for most applications. There are no specific forward scatterers modeled that would require the value of 16 except from the default ones.

LSUN=F: This makes use of the default solar  $5\text{cm}^{-1}$  spectral resolution irradiances. Trial runs with LSUN=T, which uses the  $1\text{cm}^{-1}$  binned solar irradiance data and ISUN=2, which assigns  $\text{FWHM}=2\text{cm}^{-1}$  were also performed to investigate how this change affects the output. In these runs it was set LSUNFL=F or blank, so that the Kurucz solar irradiance database was used. These runs showed there was no advantage in using LSUN=T (see figure 7.4), especially for the case of LINUS which has a spectral resolution worse than  $9\text{cm}^{-1}$ .

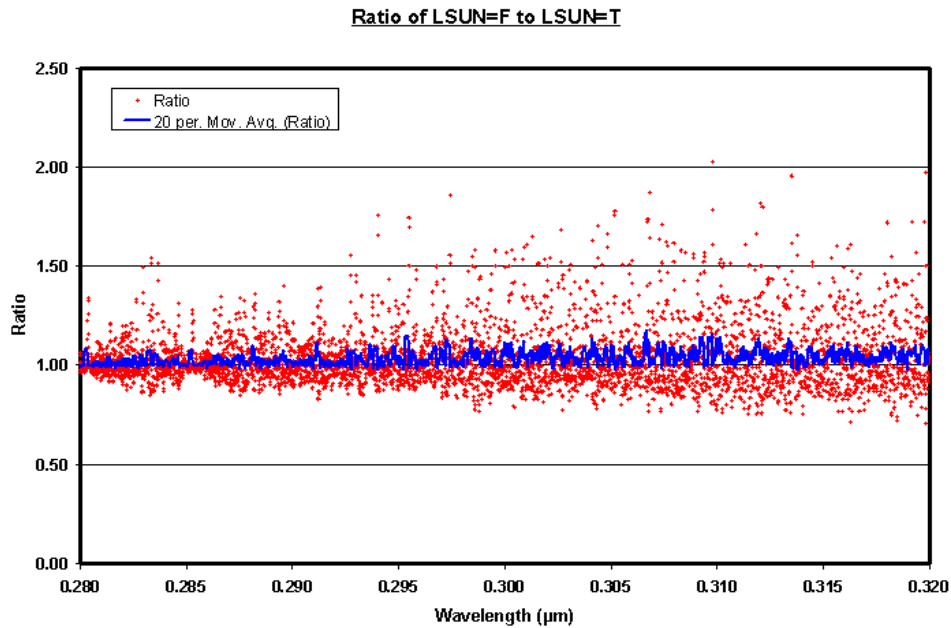


Figure 7.4. Solar irradiance comparison for  $5\text{cm}^{-1}$  (LSUN=F) and  $1\text{cm}^{-1}$  (LSUN=T)



spectral resolution. Results for Lassen Park with MODTRAN standard atmosphere 2.

CO2MX=365.00000: Use the recommended CO<sub>2</sub> mixing ratio (1999 value) instead of the default 330 ppmv.

LBMNAM=T: In order to read the newer band model parameter file BMP99\_01.BIN from Card 1A2, instead of the default BMP98\_01.BIN.

**c. Card 2**

IHAZE=1: Sets the extinction coefficient to rural with a default visibility of 23 km, which was the case at Lassen Park when the measurements were taken .

GNDALT=2.13000: This is the altitude in km at Sulfur Works location 2 in Lassen Park (see figure 6.1).

**d. Card 2C**

ML=36: Sets the number of layers in the user -defined atmospheric profile, which in this case, is 36.

IRD1=1: Read data for user-defined atmospheric profiles from cards 2C1 and 2C2.

**e. Cards 2C1 and 2C2**

ZMDL gives the altitude of layer boundary in km. After several trial runs, it was found that MODTRAN, whatever the initial altitude is (say x), divides the remaining range up to 6km in 6 layers according to the formula:

$$y = \frac{6.0 - x}{6} \quad (7.1)$$

so the first six layers (if uniformly thick) are: x, x+y, x+2y, ..., x+5y, 6.0. After 6.0, the layers are 1km thick for up to 25km. From 25 to 60km, the layers are 5 km thick, from 60 to 80km they are 10km thick and from 80km it goes directly to 100km, which is the boundary of the last layer. For the Sulfur Works case, the first layer starts at 2.13km. By

the geometry of the Sulfur Works site and the extent of the plumes, it was assumed for modeling purposes that the plume was a cylinder with a diameter of approximately 250m (rising vertically). Furthermore, by assuming that LINUS was located just outside the circumference of the cylinder and looking through the plume at an average inclination angle with respect to horizontal of 20 degrees, it was determined that the first layer, which supposedly contained SO<sub>2</sub>, was 90m thick. Then, the boundaries for the first six layers up to 6km were calculated to be 2.130, 2.220, 2.976, 3.732, 4.488 and 5.244km. All the ZMDL values used in the calculations are shown in sample input cards presented in appendix B.

T=2.200E+01: This is the temperature in Celsius of the first boundary. For the rest it was set to T=0.000E+00 so that together, with subsequent flags, the values of the MODTRAN standard model atmosphere 2 (Mid-Latitude Summer) will be used.

JCHAR(J) (with J=1-14) = 2B22222222A222, for the first layer. The 2 means use the default values for the standard model atmosphere 2. JCHR(2)=B, indicates ambient temperature in degrees Celsius. JCHR(11)=A, indicates the volume mixing ratio for SO<sub>2</sub> in ppmv. JCHAR(J)=222222222222, for the rest of the layers, which essentially means, that except for the first layer where a user defined temperature and SO<sub>2</sub> concentration was used, for the rest of the layers, default values from the MODTRAN standard model atmosphere 2 (Mid-Latitude Summer) were used.

WMOL(J)=0.000E+00 for J=1-10 and 12. Together with the flags JCHAR(J) makes use of the default concentrations from the standard model atmosphere 2 of the gases 1-10 and 12 shown in table 7.1 above.

WMOL(11) gives the concentration of the SO<sub>2</sub> in ppmv. Initial runs with the regular concentration (WMOL(11)= 0.000E+00), 10ppmv (WMOL(11)= 1.000E+01), 100ppmv and 1,000ppmv were performed to establish a SO<sub>2</sub> signature in the spectrum. Subsequently, runs with other concentrations were performed to match the modeled and experimental spectral profiles. The 10ppmv concentration (0.721atm-cm/km) is  $4.3 \times 10^4$  times larger than that of the MODTRAN standard atmosphere 2 under the same conditions. The SO<sub>2</sub> concentration as a function of altitude is given in figure 7.5.

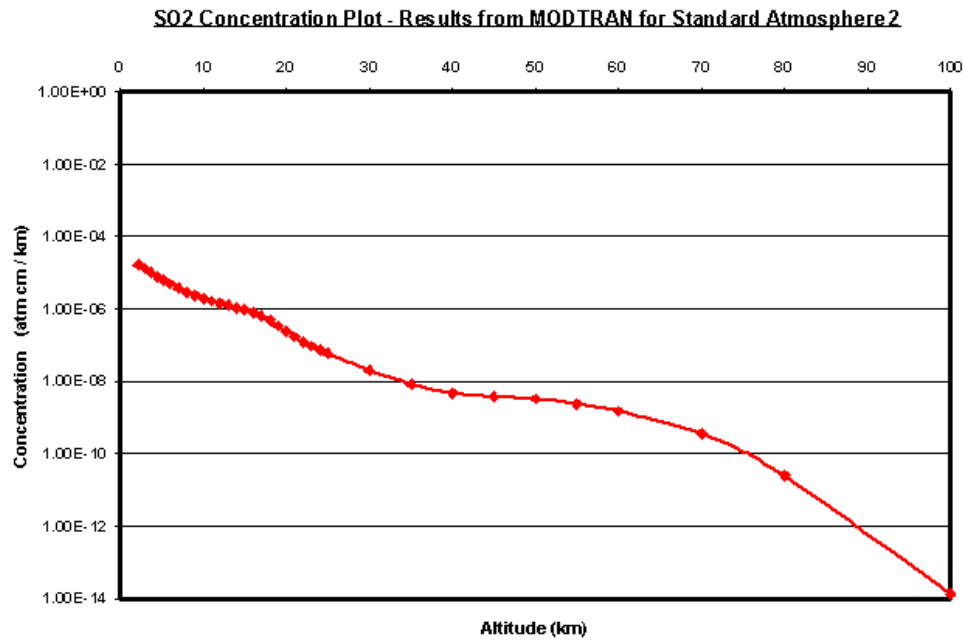


Figure 7.5. SO<sub>2</sub> concentration as a function of altitude for the MODTRAN standard atmosphere 2.

***f. Card 3***

H1=2.130: This is the initial altitude in km and defines the position of the sensor.

H2=blank since the line-of-sight is a slant path to space.

ANGLE=70: This is 90 degrees minus the inclination angle of the line-of-sight of the instrument with respect to horizontal. The majority of the measurements were taken at an inclination of 20 degrees. It changes depending on the inclination angle where a simulated measurement took place.

***g. Card 3A1***

IPARM=1: Use of sensor latitude and longitude together with the day of the year and time of the day to specify the solar geometry with respect to the line-of-sight of the sensor.

IDAY=255: This is the Julian day that the measurements took place.

***h. Card 3A2***

PARM1=40.450: This is the latitude of location 2 at Sulfur Works. It is slightly different when the measurements at locations 1 and 3 are modeled (see chapter VI).

PARM2=121.530: This is the longitude of location 2 at Sulfur Works. Same as above for locations 1 and 3.

TIME= 18.700: This is the Greenwich time of day when a modeled measurement took place. It changes for measurements performed at different times.

PSIPO=290.000: Shows the path azimuth or heading of the line-of-sight with respect to the North. It changes depending on the heading where a simulated measurement took place.

***i. Card 4***

V1 and V2: These are the initial and final frequencies in wavenumbers [ $\text{cm}^{-1}$ ] used in the calculation (spectral range of the simulation). The values used are V1=20000 and V2=50000 (0.2–0.5 $\mu\text{m}$ ).

**D. SIMULATION NOTES**

**1. Variable Values Verification**

Due to the structure of the MODTRAN input file, the values of certain variables earlier in the file restrict or define the use or not of subsequent cards and the values of other variables. Thus, caution must be taken so that the values used are compatible. If not, two possibilities normally occur. First, the code does not run and gives an error message, which gives the user an indication that something is wrong. Second, the program runs without giving any message but changes the incompatible values to compatible ones by itself. This is dangerous and can produce incorrect results. The same effect can occur due to a misplaced value in the input file, which is possible due to the strict format of the file. For example, suppose that a user wants to run MODTRAN in a

multiple scattering mode using the DISORT algorithm and azimuthal dependence (DIS=T, DISAZM=T, NSTR=8). If, by mistake, IMULT=0 is input instead of the correct 1 in the previous card, the program will assign the values DIS=F, DISAZM=F, NSTR=0 and the code will run in single scattering mode without giving any message. A good method to use to overcome these problems is to check the variable values that are echoed in the tape6 output file, against those of the input file in order to locate any possible changes.

## **2. Computational Time**

The use of the DISORT multiscattering algorithm with azimuthal dependence, in order to produce more accurate results, increases the computational time greatly. Runs without using DISORT require 2-4 minutes on a personal computer with an AMD 850MHz CPU, depending on the values of some variables. The same runs with the DISORT algorithm require about 1.5-2 hours, which is about 30 times longer run times on average. This can be a problem if a large number of simulations is required in a short period of time.

## **3. Spectral Resolution**

In the initial trial runs where SO<sub>2</sub> absorption features were investigated, MODTRAN was run at the finest possible resolution of 1cm<sup>-1</sup> bins with 2cm<sup>-1</sup> FWHM. During those runs it was found that if the spectral lower limit V1 was greater than 22,681cm<sup>-1</sup> (lower than 0.441μm), the program did not run with spectral bins of 1cm<sup>-1</sup>. Instead, it required resolution equal or greater than 5cm<sup>-1</sup> and ran in LOWTRAN mode. For this reason, the spectral region used in the initial simulations was 50,000–20,000cm<sup>-1</sup> (0.2–0.5μm). The output files were later reduced to the spectral region of interest (280–320nm). Due to the inverse relation between spatial frequency (cm<sup>-1</sup>) and wavelength, the spectral resolution over extended spectral regions is not constant but gets finer as the wavelength decreases. For the 300nm region, the resolution is 0.009nm if the spectral bins are 1cm<sup>-1</sup>.

The actual resolution of LINUS depends on the slit width and the exact values were not known at the time this thesis was written. Estimates indicate that it should be from 0.4 to 1nm. When LINUS measurements were simulated, runs at various resolutions were performed in order to reproduce profiles with similar spectral details as the measured ones. The finest resolution used was  $9\text{cm}^{-1}$  (0.08nm at 300nm) and was based on the assumption that the 512 pixels of the camera focal plane sample one wavelength per pixel in the region 278-318nm where LINUS operates (see wavelength calibration in chapter VIII). The results were much more detailed than the measured spectral profiles. After several trials it was found that simulations with  $55\text{cm}^{-1}$  bins (0.5nm at 300nm) reproduced results similar in detail with the LINUS measurements.

## VIII. DATA ANALYSIS

### A. SIMULATED DATA

#### 1. LINUS UV Filter

As mentioned in chapter V, after the radiation is reflected on the scanning mirror, it enters the optics section of the device through a filter with the response given by figure 5.3. The vendor of the filter, Omega Optical, Inc., was contacted in order to provide the filter data in electronic form so they could be used in the simulation but they did not respond to the request. The filter response curve was then digitized and fitted by the Gaussian given by equation 8.1, in units of nm, and it is plotted in figure 8.1. This fit was then used to simulate the effect of the filter on the MODTRAN output data.

$$f(x) = 15.17e^{-\frac{(x-298.43)^2}{4.48}}/2 \quad (8.1)$$

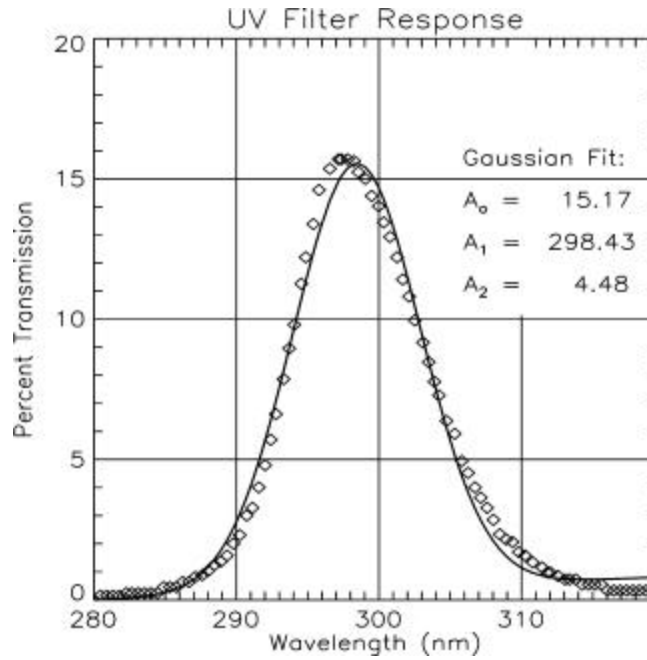


Figure 8.1. The continuous line shows the Gaussian fit of the LINUS filter response. Diamonds show data points taken from the real filter response curve presented in figure 5.3.

## 2. SO<sub>2</sub> Presence Effects and Spectral Signature

MODTRAN was run in order to find out how the presence of SO<sub>2</sub> in the plume affects the spectral profile and to establish a signature that would be searched for in the experimental data. Runs for normal atmosphere, and atmospheres with 10ppmv, 100ppmv and 1000ppmv of SO<sub>2</sub> were performed. Since at the time this thesis was written, the spectral resolution of LINUS was not known precisely, the simulations were done in two spectral resolutions. The first is 0.08nm (9cm<sup>-1</sup> at 300nm) and represents the best achievable resolution assuming that each of the 512 camera pixels records a different spectral channel (no over- or under-sampling) in the range 278.15-319.20nm, where LINUS operates as measured during calibration with platinum spectra. The second is 0.5nm (55cm<sup>-1</sup> at 300nm), which is the estimated device resolution taking into account the device slit width and optics limitations. The results presented in figures 8.2 through 8.8 are for the Sulfur Works location 2, with a heading of 290 degrees, an inclination to horizontal of 20 degrees at 10:45 a.m. The lines in the plots are fitted curves to the data points, which are plotted with dots.

### *a. Figures 8.2 through 8.4*

Figures 8.2 through 8.4 show the simulated spectral profiles for the various SO<sub>2</sub> concentrations that reach the aperture of LINUS before they pass through the filter. Figures 8.2 and 8.3 are for the same resolution of 0.08nm, but the second picture has a smaller scale in the radiance axis in order to show the details at lower wavelengths. Figure 8.4 shows the profiles for 0.5nm resolution. The observations deduced are as follows:

- The radiation is rapidly reduced as the wavelength is reduced and there is practically no signal below 295nm even for the regular atmosphere.
- The profile of the low SO<sub>2</sub> concentration of 10ppmv is similar to that of the regular atmosphere with minor differences. The profile of the 100ppmv concentration is significantly different than that of the regular atmosphere and strong SO<sub>2</sub> absorption features can be identified. The 1000ppmv concentration diminishes the signal so much that it makes it practically zero, so that presence of concentration of this order in the line-of-sight of the device would be immediately evident.



- There is a significant difference in the structure of the profiles with resolution. The 0.08nm profiles have many more details than that of 0.5nm, facilitating the identification of absorption characteristics. In the 0.5nm resolution, the details are smoothed out and in order to identify differences in the profiles, the difference in concentrations has to increase significantly.

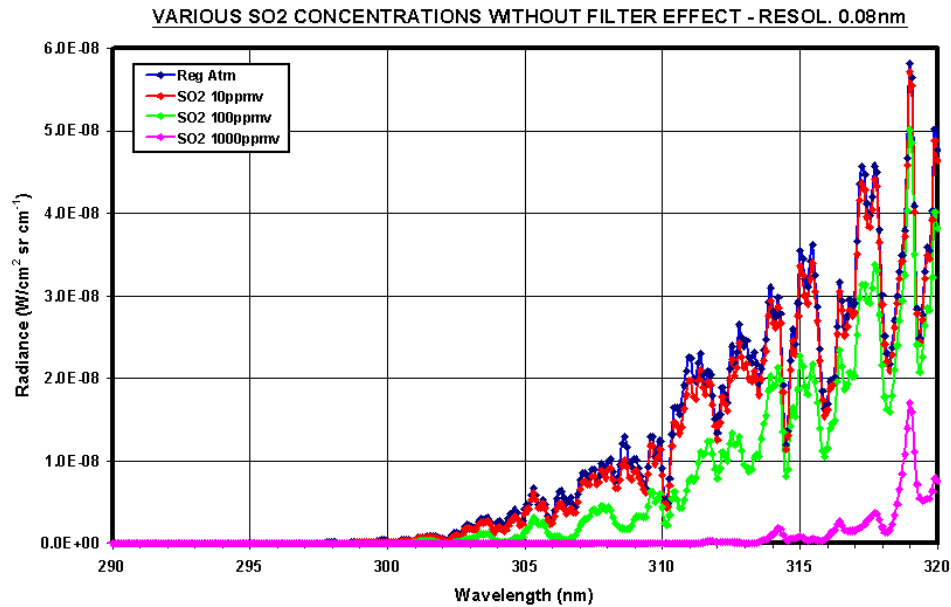


Figure 8.2. Simulated sky radiance spectral profiles for various SO<sub>2</sub> concentrations at Sulfur Works without LINUS filter effect. Resolution 0.08nm.

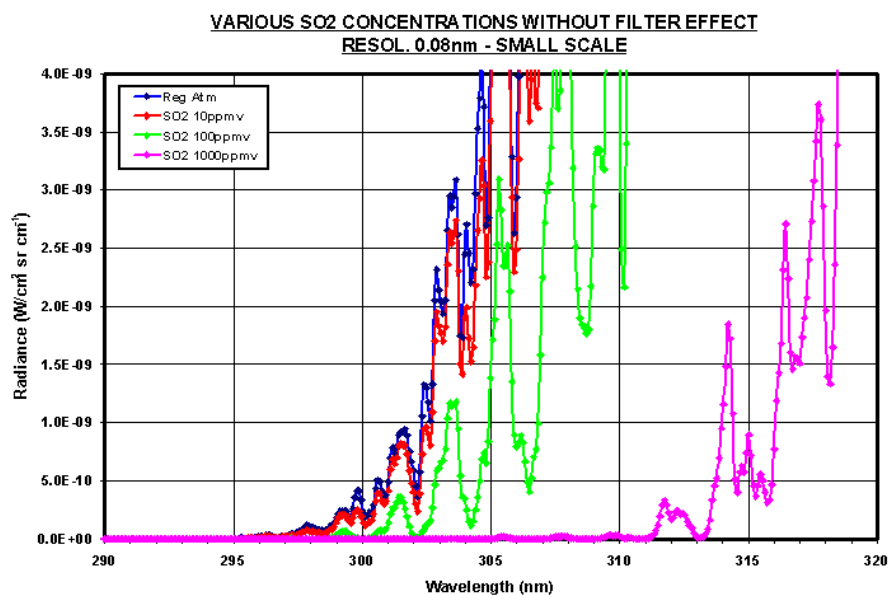


Figure 8.3. Simulated sky radiance spectral profiles for various SO<sub>2</sub> concentrations at Sulfur Works, without LINUS filter effect, at smaller scale than figure 8.2. Resolution 0.08nm.

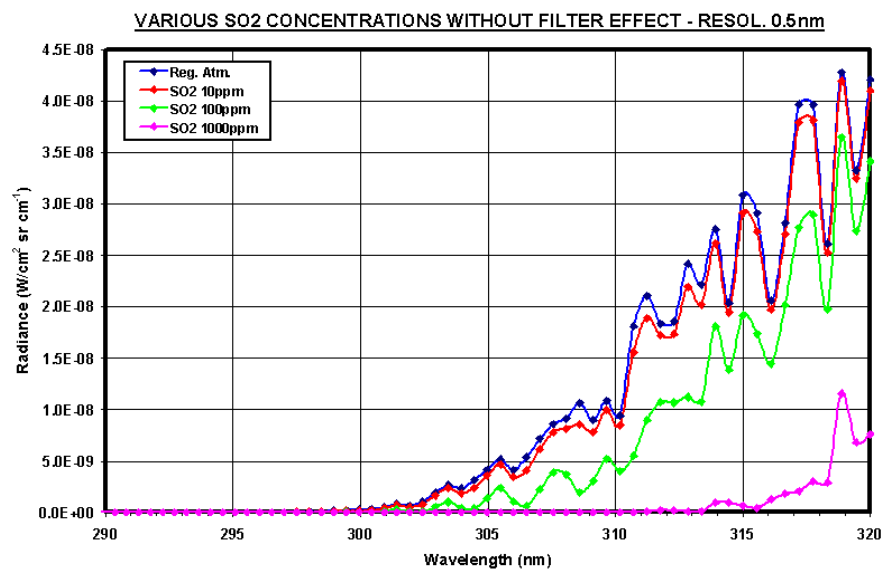


Figure 8.4. Simulated sky radiance spectral profiles for various SO<sub>2</sub> concentrations at Sulfur Works without LINUS filter effect. Resolution 0.5nm.

***b. Figures 8.5 and 8.6***

Figures 8.5 and 8.6 show the simulated spectral profiles for the various SO<sub>2</sub> concentrations after they have past through the LINUS filter. Essentially, these figures are produced from the data used to plot figures 8.2 and 8.4 after applying the Gaussian effect shown in figure 8.1. The observations deduced from these figures are:

- It is obvious that the filter suppresses the spectral profile above 312nm where significant SO<sub>2</sub> absorption effects are observed in the unfiltered data. There is practically no effect below 295nm from the filter, since the available radiation is already diminished by itself.
- The signal passing through the 1000ppmv concentration, already small without the filter effect, after the filter is so small that it does not show up with the existing scale of the radiance axis. For this reason, it was not plotted in this set of figures.
- The filter modulates the profiles and gives them a Gaussian-like shape. Although the filter has maximum transmittance at 298.4nm, the maximum of the spectral profiles is at about 305nm due to the rapid increase of the signal as the wavelength increases.
- As with the previous figures, the 0.08nm resolution profiles have significantly more detailed structure than those of the 0.5nm. With the latter resolution, much of the detail is lost due to under-sampling of the spectral region.
- There is a number of well-defined SO<sub>2</sub> absorption characteristics in the spectral profiles of the SO<sub>2</sub> concentrations, with much more profound those of the 100ppmv. These characteristics are greater in number and magnitude in the 0.08nm resolution plot and are diminished in the 0.5nm resolution plot. In the first plot (figure 8.5) they are observed at 297.9, 299.9, 300.6, 302.4, 302.9, 304.0, 304.6, 306.3, 308.6 and 310.7nm. In the second plot (figure 8.6) they appear at 298.0, 299.9, 308.6 and 310.7nm.

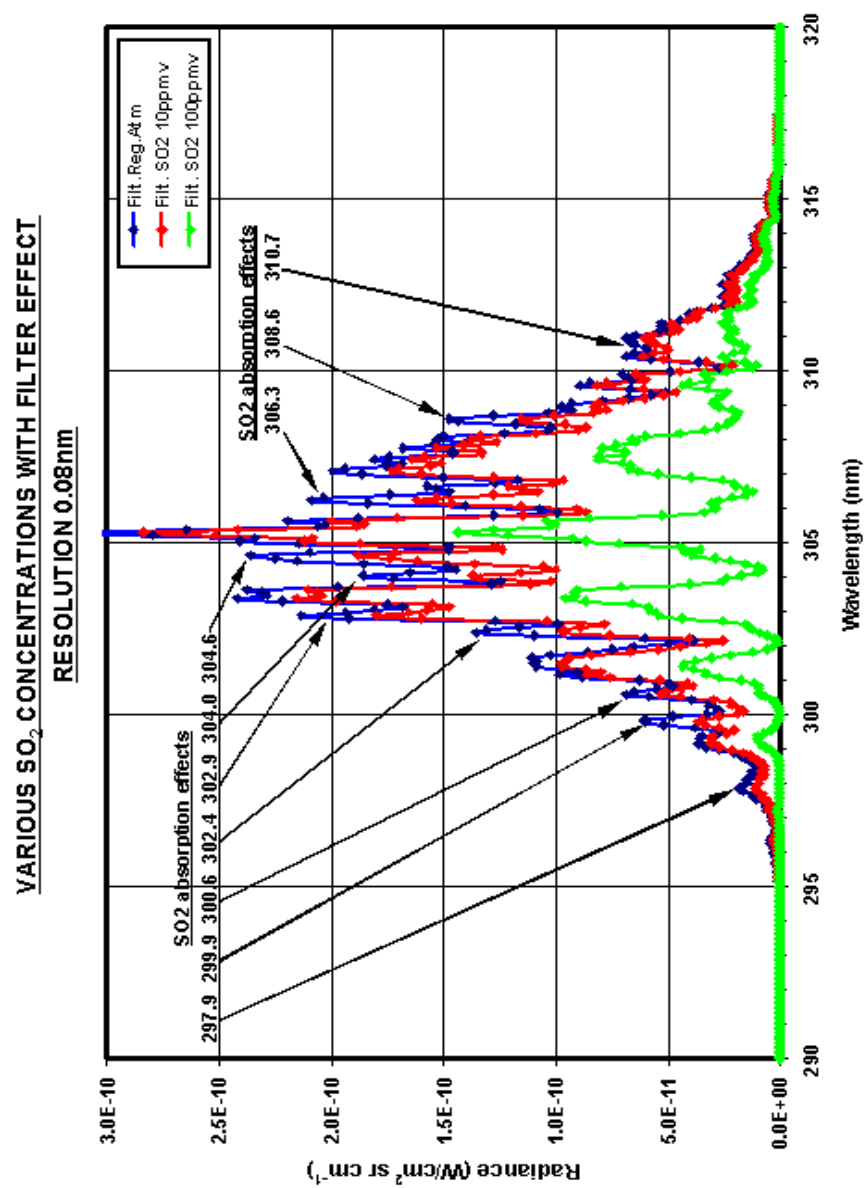


Figure 8.5. Simulated spectral profiles for various SO<sub>2</sub> concentrations at Sulfur Works with LINUS filter effect. Resolution 0.08nm

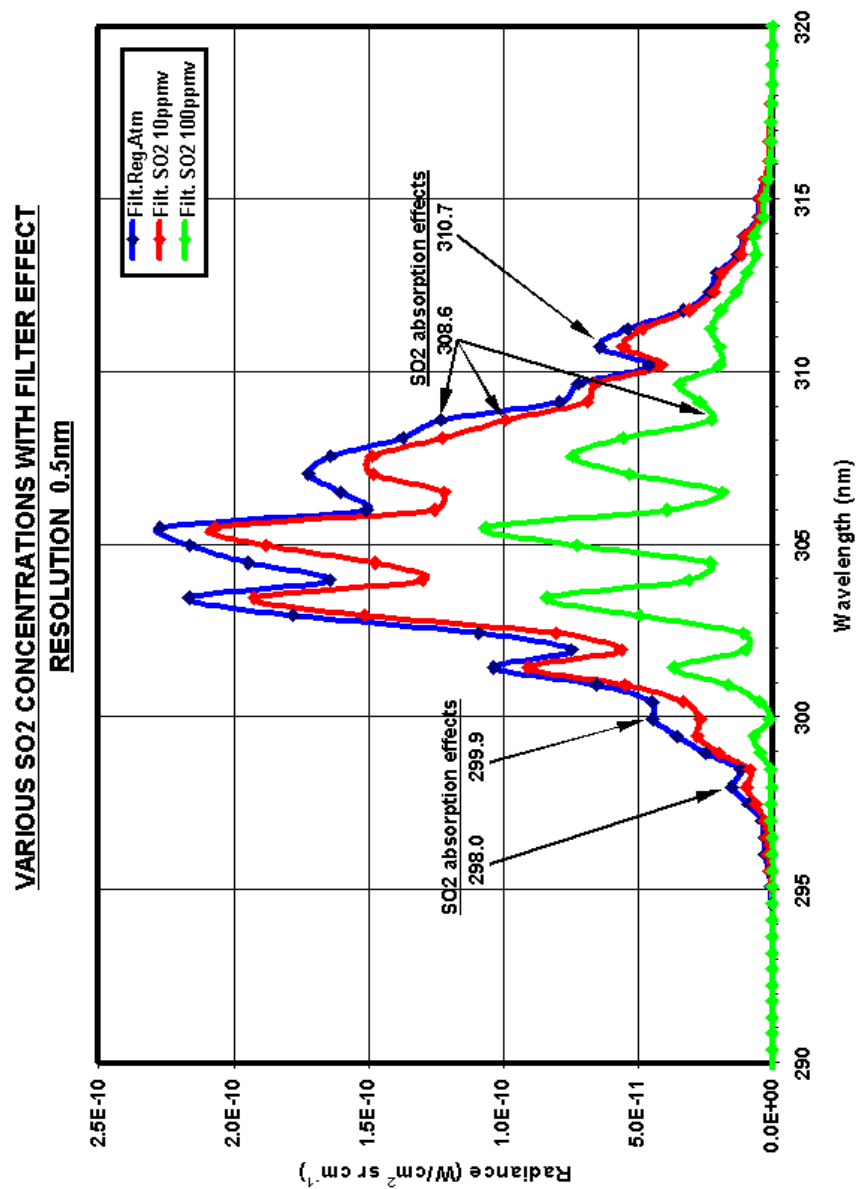


Figure 8.6. Simulated spectral profiles for various SO<sub>2</sub> concentrations at Sulfur Works with LINUS filter effect. Resolution 0.5nm

*c. Figures 8.7 and 8.8*

Figures 8.7 and 8.8 show the ratios of the SO<sub>2</sub> containing spectral profiles divided by the profile of the regular atmosphere in order to find out the SO<sub>2</sub> presence signature. The observations from these figures are:

- Both 0.08 and 0.5nm resolutions give similar results, but the absorption characteristics in the former are well defined by many data points, while in the latter, they are barely defined by 3-4 data points. This indicates that the resolution of 0.5nm is marginal and lower resolutions (larger than 0.5nm) are not able to identify SO<sub>2</sub> absorption characteristics.
- The troughs are due to the SO<sub>2</sub> absorption bands with the stronger effect appearing at 299.9nm for the 10ppmv concentration and 299.9, 304.4 and 306.5nm for the 100ppmv. Furthermore, the total signal is diminished especially at smaller wavelengths. The greater the concentration, the smaller the overall signal. At 1000ppmv, there is practically no signal as was also observed in the previous plots of the radiance space.
- The absorption characteristics are in agreement with those observed in the previous figures of the wavelength-radiance plots.
- The absorption characteristics revealed by the ratios are in a very good agreement with the SO<sub>2</sub> absorption cross-section measurements presented in chapter III, figures 3.2 and 3.7.
- The ratio is very sensitive to SO<sub>2</sub>-induced effects in the spectral profiles. Even for the low concentration of 10ppmv, which does not induce significant changes with respect to the profile of the regular atmosphere in the radiance space, the ratio clearly reveals its presence. This indicates that the ratio with clear sky spectra is a valuable tool giving a definite SO<sub>2</sub> signature even for small concentrations.

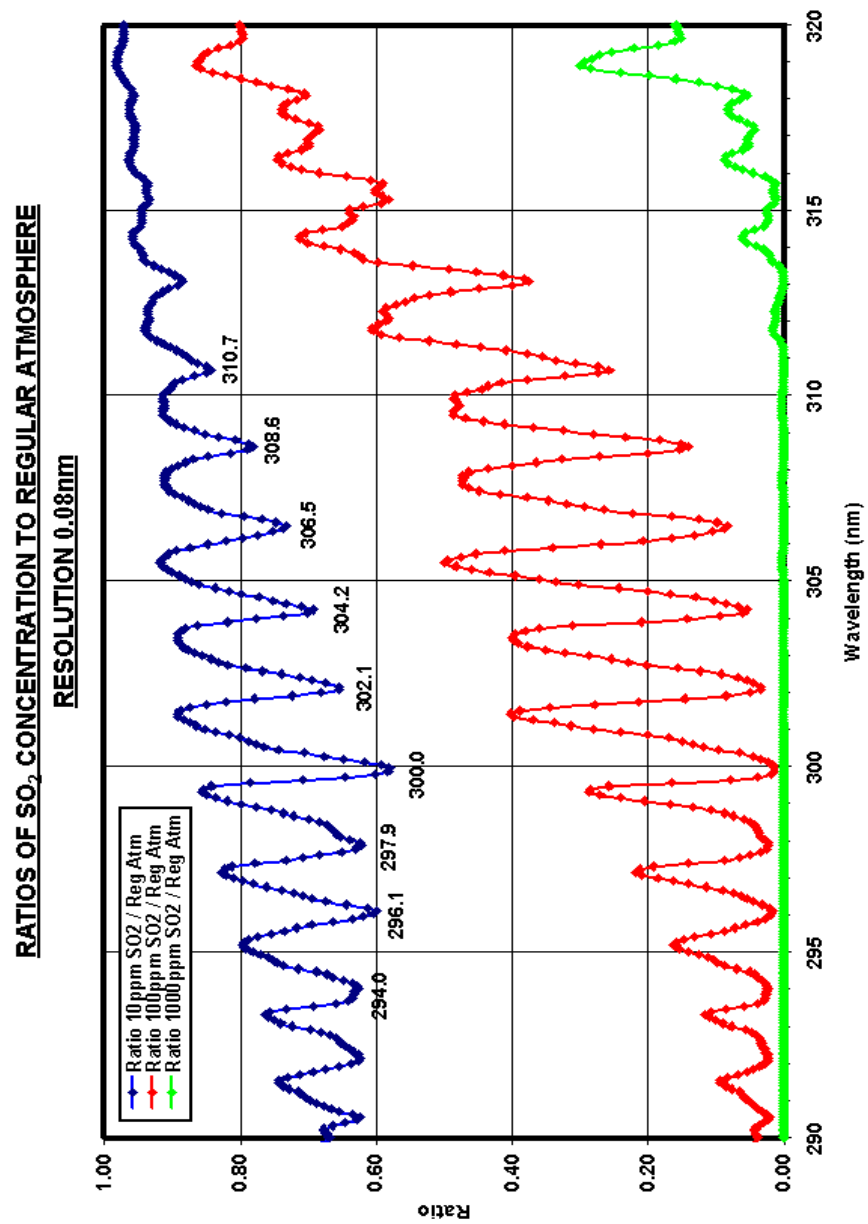


Figure 8.7. Ratios of SO<sub>2</sub> concentrations to regular atmosphere at 0.08nm resolution.

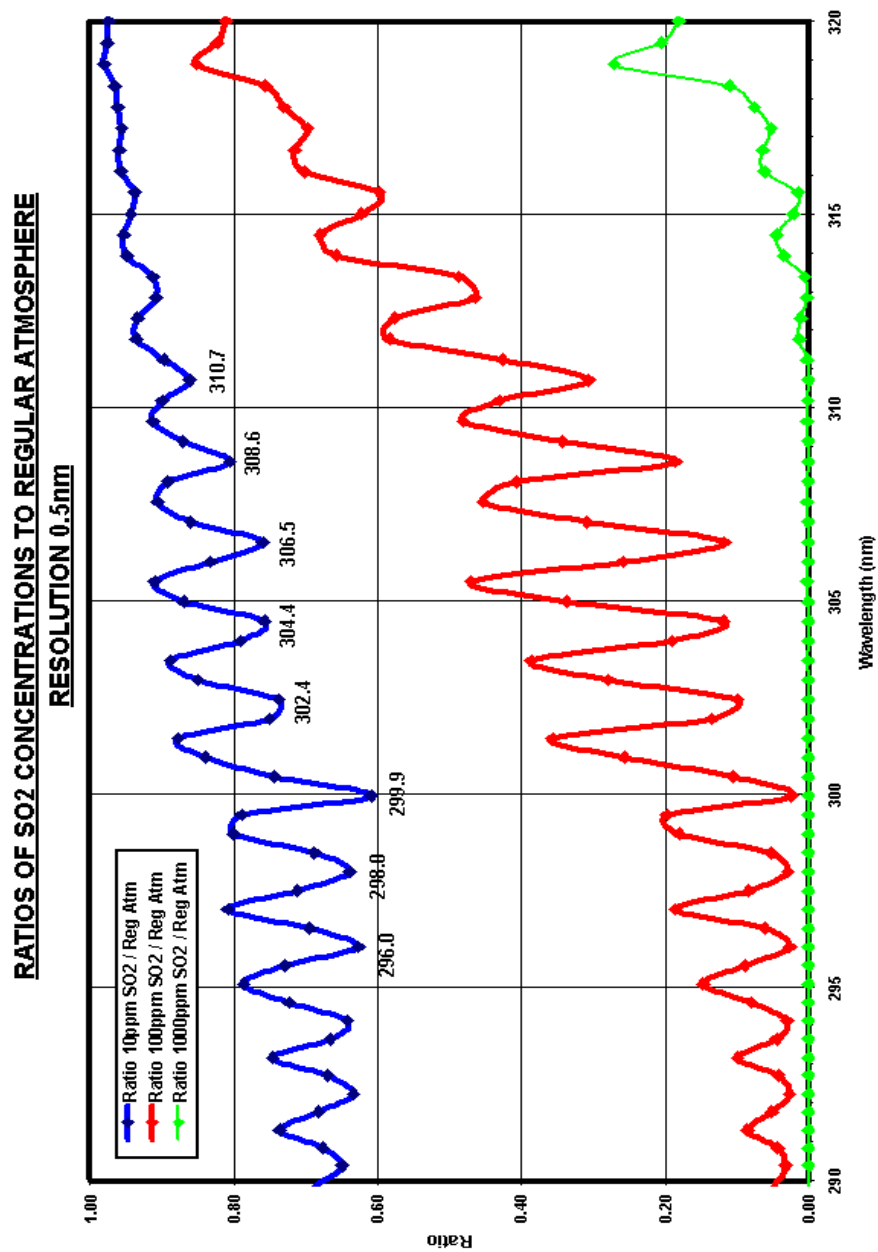


Figure 8.8. Ratios of SO<sub>2</sub> concentrations to regular atmosphere at 0.5nm resolution.



### 3. Spectral Profile Structure Investigation

In an effort to identify the origins of the observed spectral profile structure in the region of interest, additional MODTRAN simulations were performed. In these simulations, the effects of the oxygen ( $O_2$ ) and ozone ( $O_3$ ) molecules were investigated since these are considered to be the most significant molecules in the UV region. Comparisons of the results of the MODTRAN standard atmosphere 2 (Mid-Latitude Summer) to those of the same atmosphere that contained no  $O_2$ , no  $O_3$  and no  $O_2$  and  $O_3$  at the same time were performed. Solar irradiance measurements at the top of the atmosphere (TOA) were also examined. The following conclusions were reached from those simulations:

- Oxygen has no effect in the structure of the spectral profile in the region of interest.
- Ozone greatly diminishes the radiance by a varying way as illustrated in figures 8.9 through 8.11 below. In figure 8.9, the radiances of regular atmosphere and atmosphere without  $O_3$  are plotted. For illustration purposes, a moving average is also plotted. In figure 8.10, the ratio of the regular atmosphere to atmosphere with no  $O_3$  in logarithmic scale is presented in order to illustrate the varying effect of  $O_3$  with wavelength. In figure 8.11, the same ratio in linear scale is plotted in order to highlight the region above 300nm. It is evident that at smaller wavelengths,  $O_3$  does not induce a structure to the spectral profile up to 313nm except that it significantly and monotonically decreases the signal.

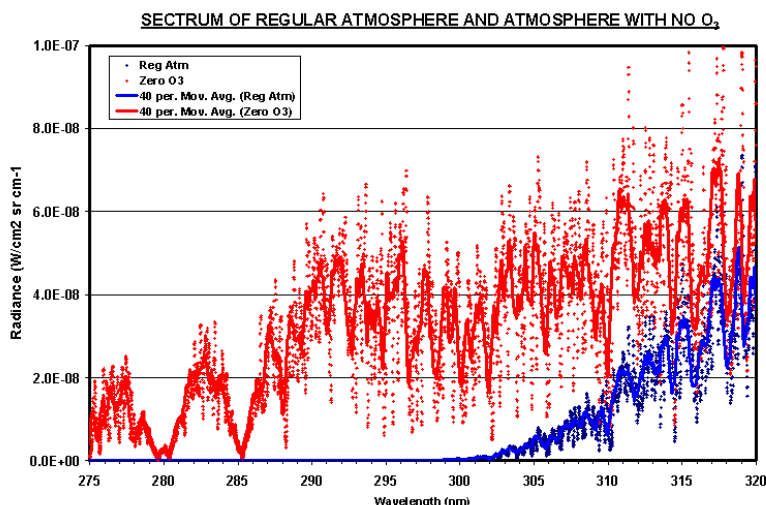


Figure 8.9. Spectrum of regular atmosphere and atmosphere with no  $O_3$ .

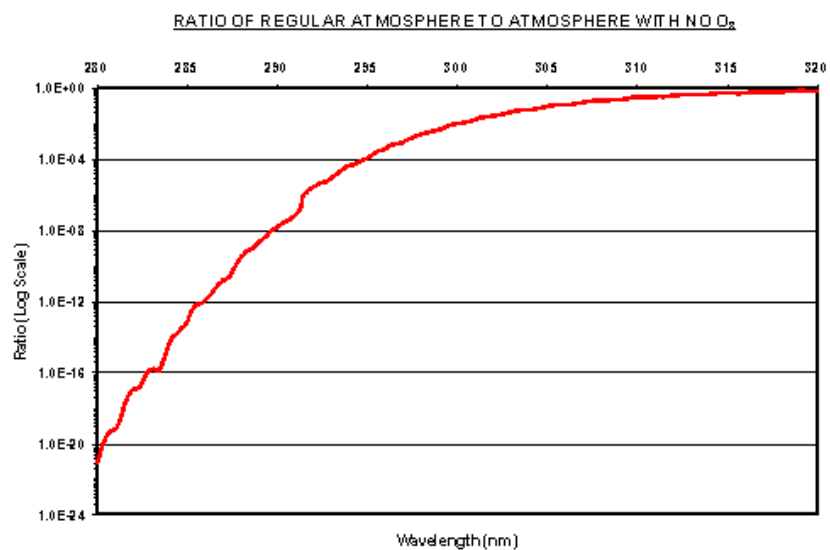


Figure 8.10. Ratio of radiances in log-scale of regular atmosphere to atmosphere with no O<sub>3</sub>.

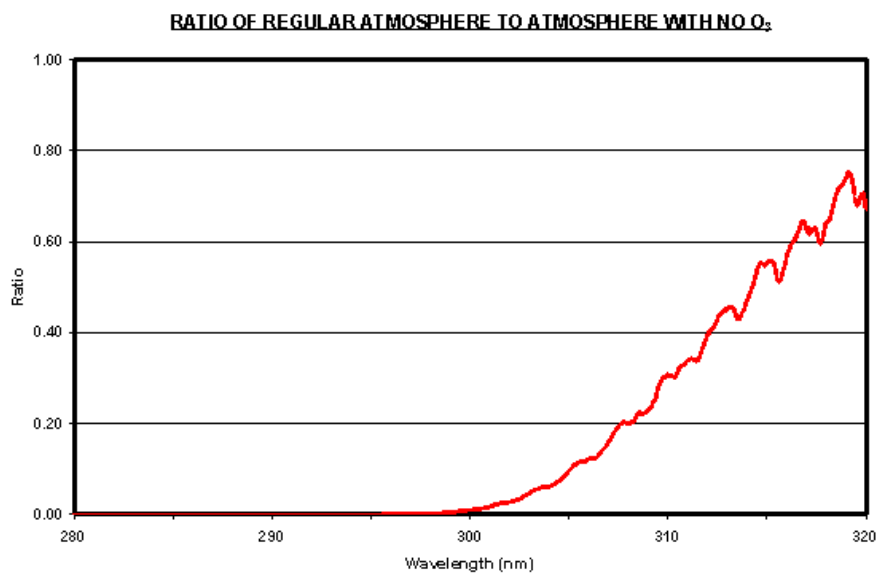


Figure 8.11. Linear ratio of radiances of regular atmosphere to atmosphere with no O<sub>3</sub>.

- In figure 8.12, the solar irradiance out of the atmosphere, as given in the corrected Kurucz database (Berk et al., 1999), together with the radiance of regular atmosphere at 2.13km altitude, are plotted. Due to the significant scale change that the atmospheric radiance experiences in this region, only a small spectral interval is plotted. For illustration purposes, a moving average was used. There is good agreement in the overall structure of the two curves. Thus, the main cause for the observed spectral structure in the spectral region of interest is the solar irradiance before it enters the atmosphere.

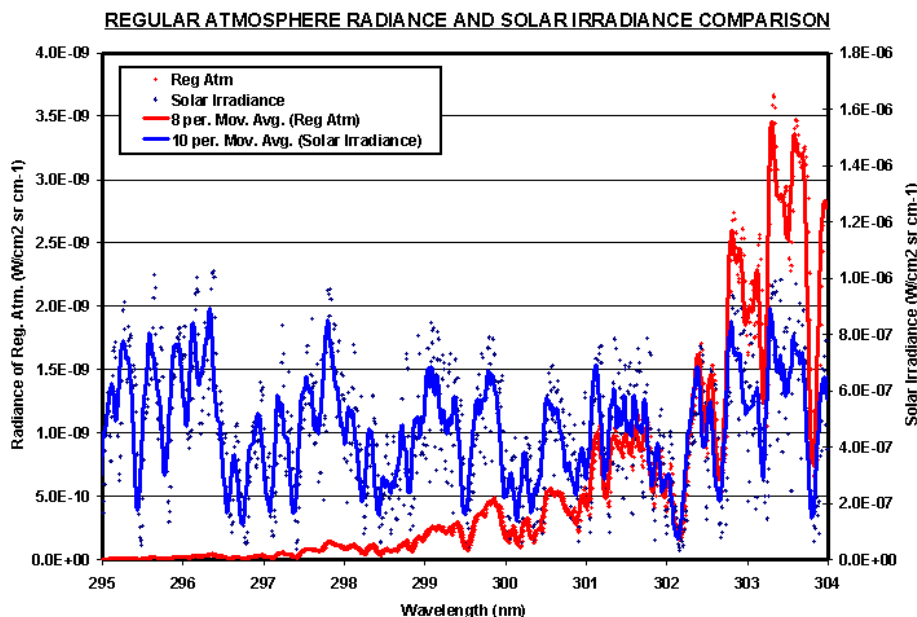


Figure 8.12. Spectrums of solar irradiance out of the atmosphere and regular atmosphere radiance at 2.13km altitude.

## B. EXPERIMENTAL DATA

### 1. Wavelength and SO<sub>2</sub> Calibration of LINUS

Soon after the acquisition of the experimental data, a wavelength calibration was performed in the lab in order to assign a wavelength scale to the raw data. The calibration was performed using a platinum lamp and the results are shown in figure 8.13.

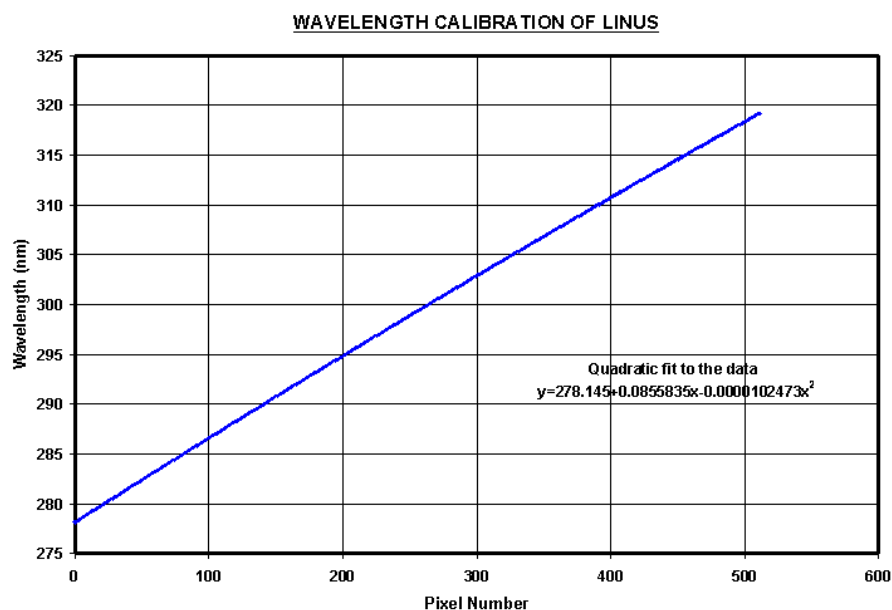


Figure 8.13. Results of wavelength calibration of LINUS using a platinum lamp.

An SO<sub>2</sub> calibration was also performed using a photocell with various pressures of SO<sub>2</sub> and a deuterium lamp as the UV source. The results with a slit width of 0.11mm are presented in figure 8.14. The SO<sub>2</sub> absorption characteristics, the reduction in transmission and the fine structure of the curves, are evident. It should be noted that the fine structure did not appear in the measurements performed with a 0.55mm slit width, due to the reduced resolution of the device at that slit width. Each plotted curve is the ratio of the radiance recorded by the device at the specific SO<sub>2</sub> pressure, divided by a subsequent measurement with the photocell completely evacuated. For more details on the two calibrations, see Gray, 2002.

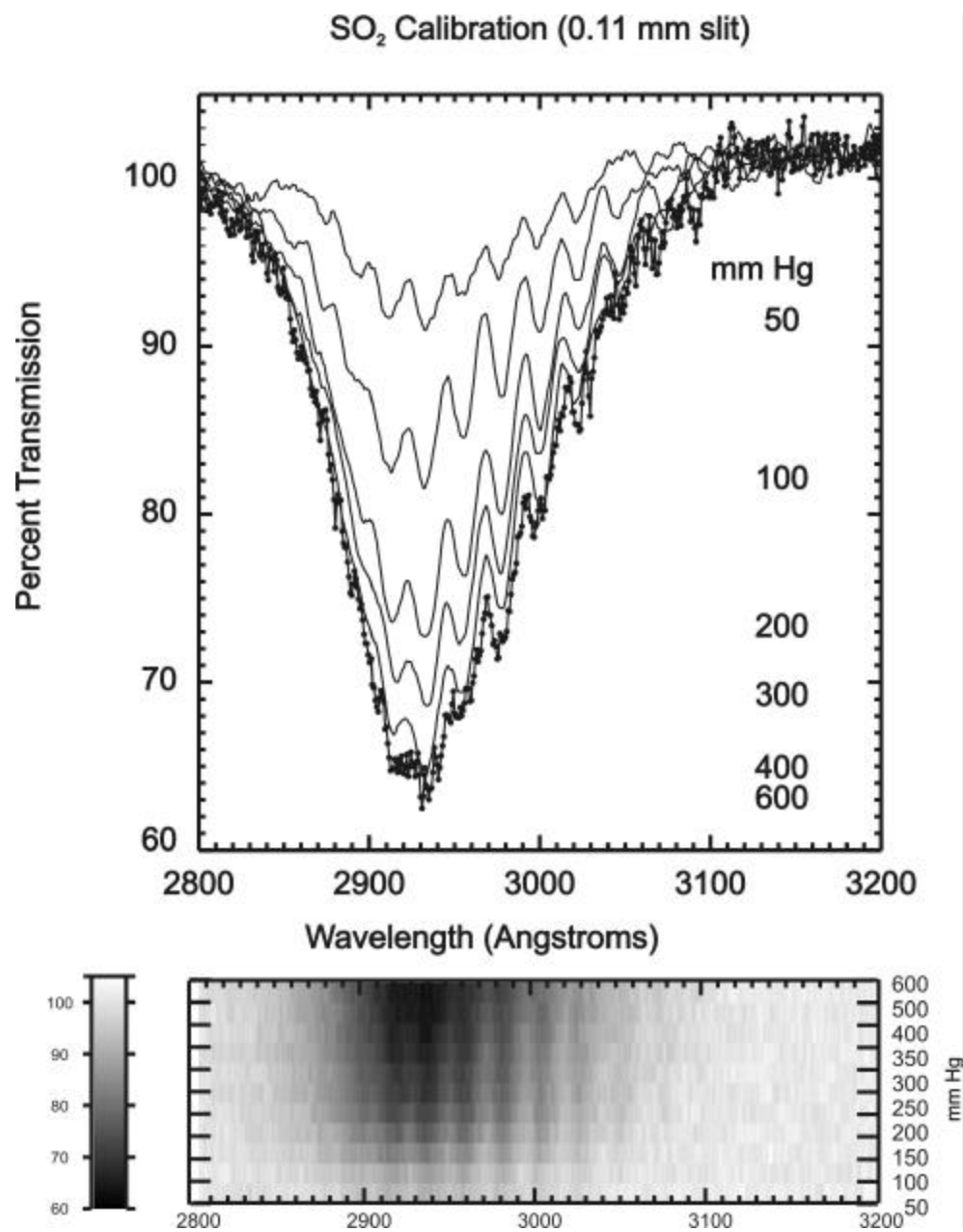


Figure 8.14. SO<sub>2</sub> calibration results of LINUS.

## **2. Data Analysis**

For each collected image a wavelength assignment was performed according to the results of the calibration mentioned earlier. Then, a spectral profile was extracted by averaging the radiance values of the middle 256 pixels along the vertical axis of the image (spatial y axis) as explained and illustrated in chapter VI, figure 6.8. Subsequently, there were two approaches in the data analysis: an individual image analysis and an ensemble analysis.

### ***a. Individual Image Analysis***

Initially, the selection of specific images was done according to several criteria, such as the quality of the image, no over or under exposure, no objects in the image, strong spectral profile etc. From those images, those taken with the line-of-sight over the gas vents and those of the clear sky taken at Lassen Peak were finally selected. Images taken with the aperture covered were also selected in order to evaluate the response of the device with no incoming signal.

The plots of the spectral profiles of the selected images are presented in appendix C. Figure C.1 shows the spectral profiles of all selected images. Figures C.2 and C.3 show spectral profiles of images taken over the vents at Sulfur Works from location 2 and figure C.4 shows those taken at Lassen Peak (clear sky spectra). In figure C.5, the data were acquired with the aperture of LINUS covered. In figures C.2 through C.5, the red curve represents the average of all the plotted curves in each figure.

A plot of all the averages is shown in figure 8.15 below. The differences in radiance are due to different slit widths, acquisition times, inclinations, headings and time of the day the images were acquired. The sw\_012 through sw\_020 files are the ones with the aperture covered (see also figure C.5). It is obvious that their spectral profile is practically flat and does not induce any structure to the signal. For that reason and since ratios were mainly used in the subsequent analysis, no action to eliminate the device “dark” response was taken.

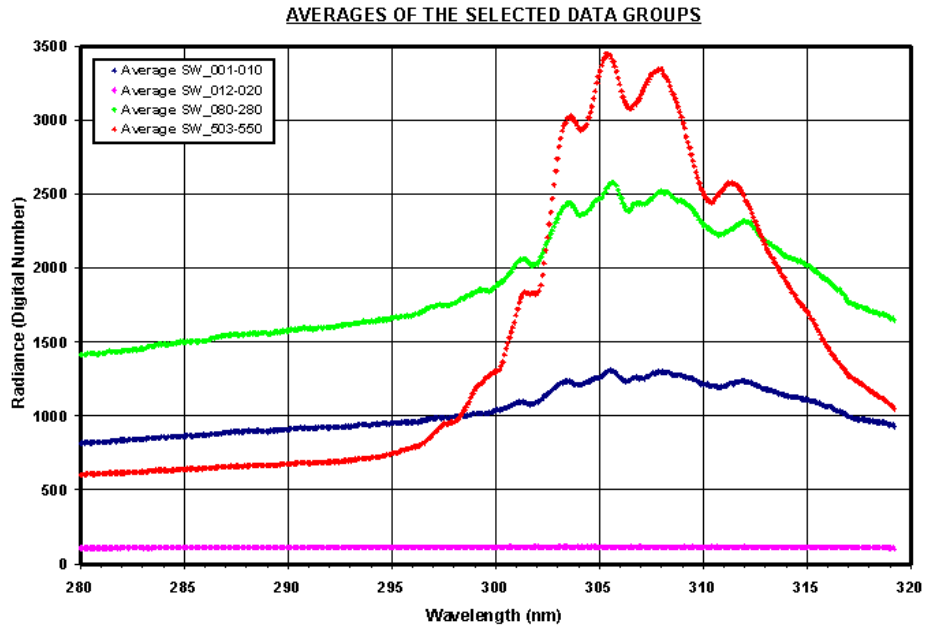


Figure 8.15. Plot of the averages from figures C.2 through C.5.

Figure 8.16 shows a comparison in radiance space of selected spectral profiles with strong structure taken over the Sulfur Works vents, where the presence of  $\text{SO}_2$  was investigated, divided by a Lassen Peak profile, which is clear atmosphere data. The most notable differences in structure appear at 297.7 and 299.7nm, where two peaks of the Lassen Peak profile do not appear in the Sulfur Works profile. These two characteristics are in agreement within 0.3nm with the  $\text{SO}_2$  absorption cross-section characteristics measured at 298.0 and 300.0nm (chapter III, figure 3.3) and within 0.2nm with the simulation results at 297.9 and 299.9nm (figure 8.5 above).

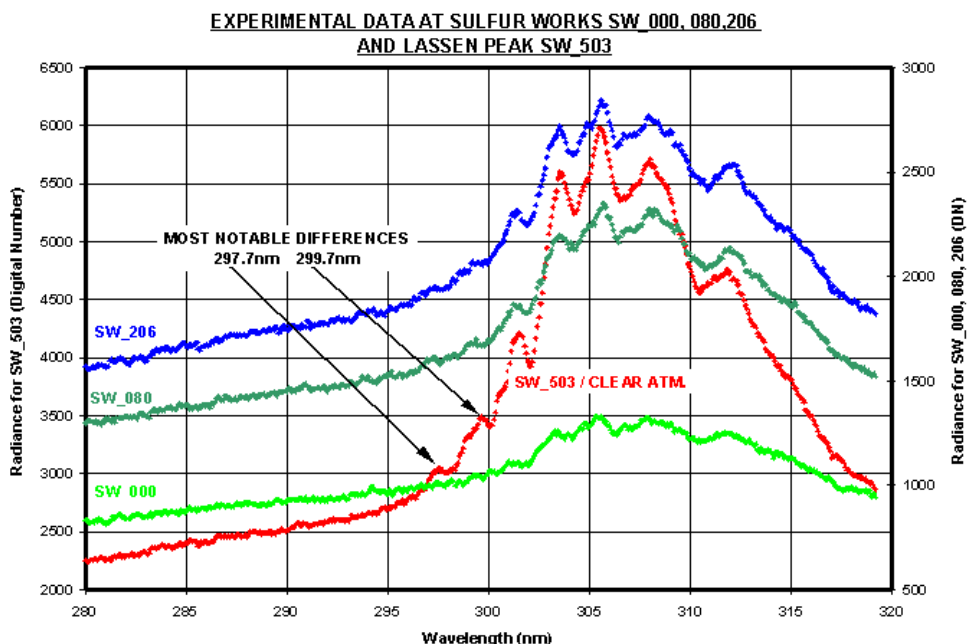


Figure 8.16. Comparison of spectral profiles with strong structure over the Sulfur Works vents (possible  $\text{SO}_2$  presence) with Lassen Peak (clear atmosphere).

Furthermore, the profiles with the most significant spectral structure from Sulfur Works were divided by one from Lassen Peak, in an effort to find out whether a signature of  $\text{SO}_2$ , as specified by the simulations, was present. The results are presented in figure 8.17 below. The observations from this figure are as follows:

- The overall shape of the curves has similarities to those of the  $\text{SO}_2$  calibration (figure 8.14), the difference being that the calibration curves are shifted about 13nm to the left. In the calibration case, the radiation source was a deuterium lamp while at Lassen Park, it was the sun.
- There is a structure to the curves with troughs at 297.8, 299.8, 300.6, 301.6, 303.7, 305.8, 308.4 and 311.1nm. From those, the troughs at 301.6, 303.7 and 305.8nm are very profound while the rest are weak. The troughs, which agree with the  $\text{SO}_2$  absorption characteristics specified by the MODTRAN simulations, are at 297.8, 299.8, 300.6 and 308.4nm. The rest, including the most profound, do not agree with those that were simulated. The differences are due to a right shift of about 0.5-0.6nm of the simulated data.



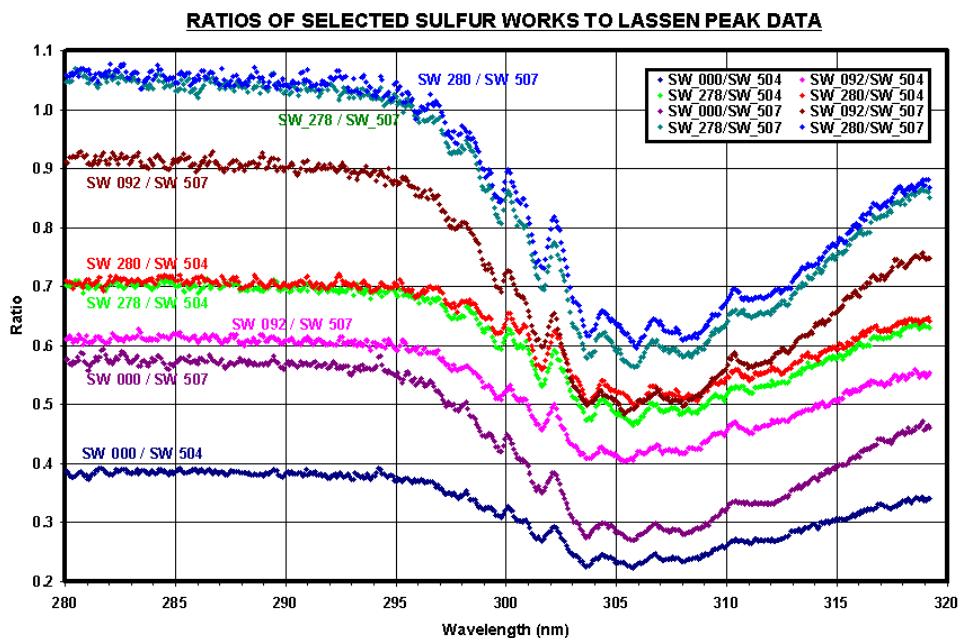


Figure 8.17. Ratios of strong Sulfur Works spectra (possible SO<sub>2</sub> existence) with strong Lassen Peak spectra (clear atmosphere).

The ratios of the averaged spectral profiles are plotted in figure 8.18 below. The detail of the spectral structure of the previous figure is diminished but not lost. Ratios of profiles with a less strong structure are also plotted in figure 8.19 for comparison. These ratios have no detail in their structure compared to figures 8.17 and 8.18.

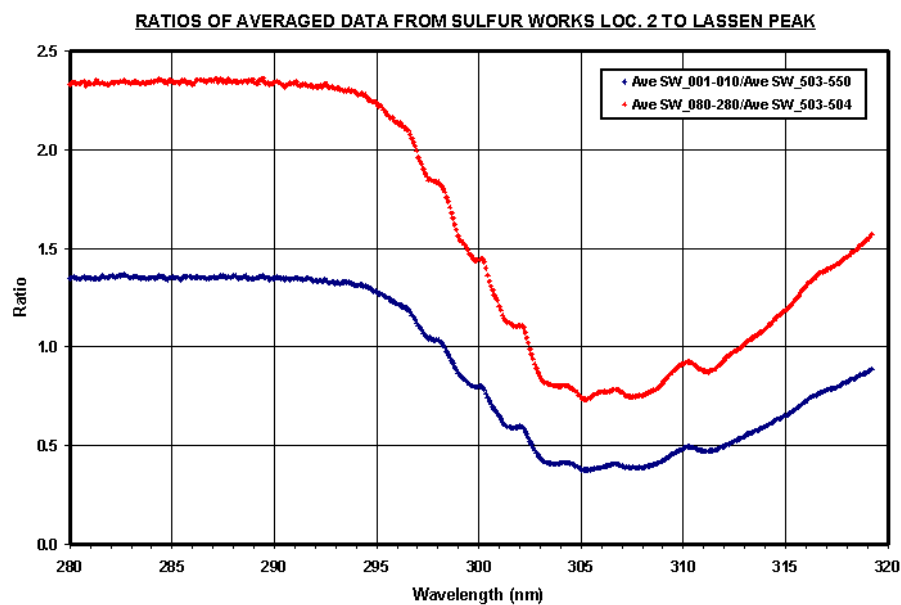


Figure 8.18. Ratios of the Sulfur Works averages (blue, green) to the Lassen Peak average (red) shown in figure 8.15 above.

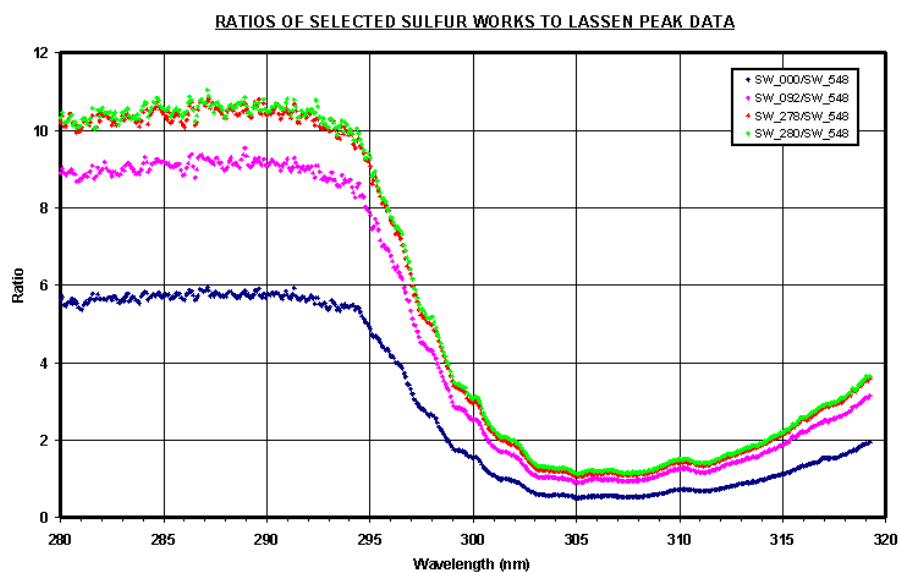


Figure 8.19. Ratios of Sulfur Works (possible  $\text{SO}_2$  existence) with Lassen Peak spectra (clear atmosphere). Spectral profiles that do not have strong structure were used.

**b. Ensemble Analysis**

In this approach, the data were treated as a whole in an effort to find bold characteristics of SO<sub>2</sub> absorption. One of the products of this effort is illustrated in figure 8.20. The vertical axis shows all the images collected at Lassen Park represented as lines. In order to produce a line, the middle 256 spatial lines of each image were averaged as described earlier. Horizontal black lines represent images that were rejected as “bad”, in order not to induce undesirable effects to the statistics of the whole image. The average spectrum of all images, along with a simulated spectrum of clear atmosphere, are also plotted. Finally, the figure includes one of the results of the SO<sub>2</sub> calibration. Observations similar to those deduced from the individual image analysis described earlier can be identified. The spectral character of all images is evident. No bold SO<sub>2</sub> absorption characteristics could be identified by this approach.

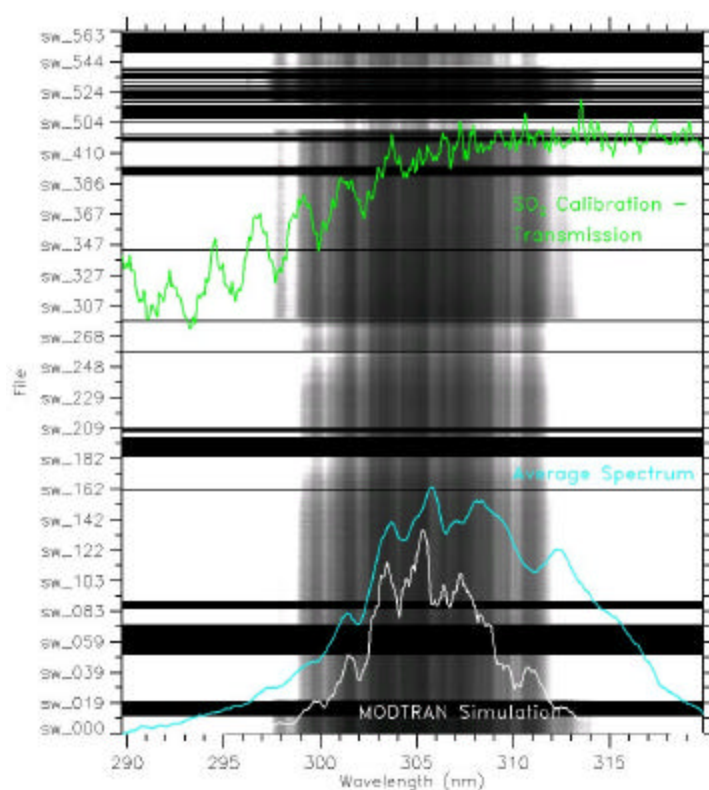


Figure 8.20. Summary of the experimental measurements with a simulated clear atmosphere and SO<sub>2</sub> calibration spectral profiles.

### C. COMPARISON BETWEEN EXPERIMENTAL AND SIMULATED DATA

In an effort to evaluate how well simulated and experimental data agree with each other, and if SO<sub>2</sub> presence characteristics deduced by the simulations exist in the experimental data, many comparisons were performed. The comparisons, as above, included selected images against selected simulated data and comparisons of all the data as a whole as described in the ensemble approach above. Some of these comparisons in the radiance space are presented in figures 8.21 through 8.26.

The general observations from these graphs are:

- There is a good agreement between simulated and experimental data from about 290 to 306nm. From 306nm and above, although the profile structures are similar, the experimental profile becomes wider and the peaks and troughs are in different wavelength positions. This is attributed to effects of the filter of the device to the recorded radiation, which could not be reproduced by the filter simulation. As illustrated in figure 5.3, the filter response curve is slightly tilted towards the smaller wavelengths and the Gaussian fit did not reproduce this effect (see figure 8.1).
- The shape of the experimental curves along the radiance axis depends upon the acquisition time and slit width, while the simulated curves do not.
- The simulated curves have zero radiance outside the response region of the simulated filter, while the experimental curves have non-zero values in this region due to the dark response of the device and possibly, stray radiation coming into the device from paths other than its line-of-sight.

Figures 8.21 and 8.22 show the simulated and measured spectral profiles of clear atmosphere (without SO<sub>2</sub>). The simulated data are in the two resolutions used in the simulations. It is evident that the details of the experimental spectral profile match those of the 0.5nm resolution much better than those of the finer 0.08nm resolution. The conclusion from these graphs is that LINUS with a 0.11mm slit width operates at about 0.5nm resolution.

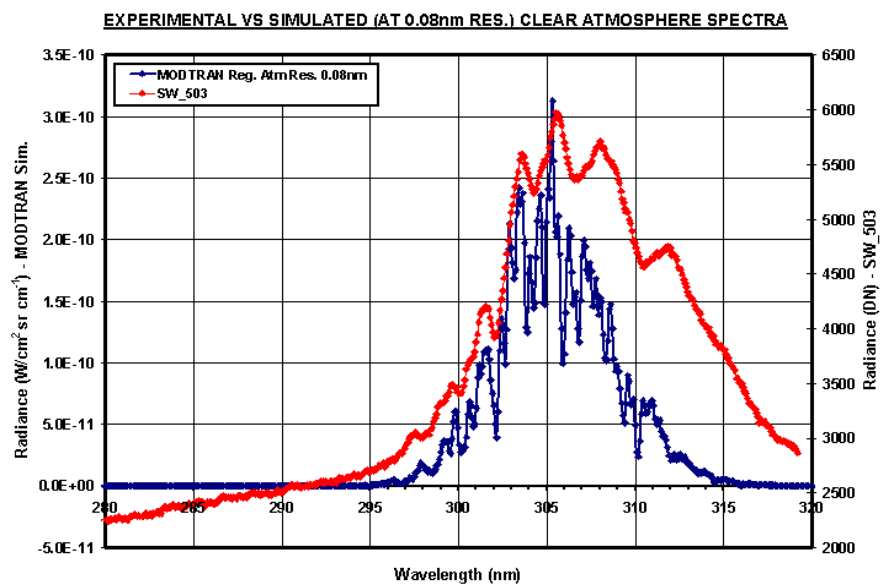


Figure 8.21. Measured and simulated spectral profiles of clear atmosphere. The simulated data are in 0.08nm resolution.

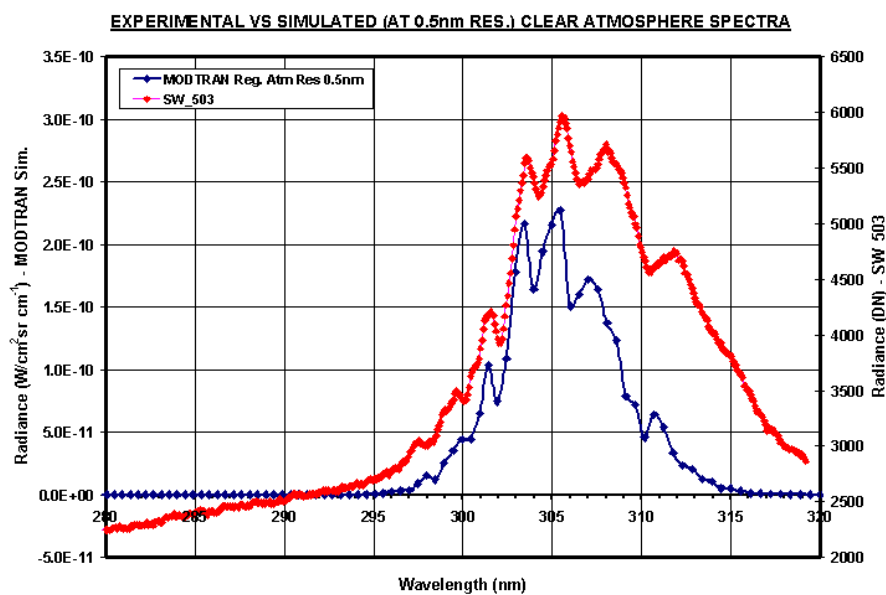


Figure 8.22. Measured and simulated spectral profiles of clear atmosphere. The simulated data are in 0.5nm resolution.

Figure 8.23 shows two spectral profiles looking over the vents at Sulfur Works, compared to regular atmosphere and 10ppmv SO<sub>2</sub> simulated spectral profiles. The most noticeable difference in the simulated data at 300nm agrees with the behavior of the experimental curves in that area.

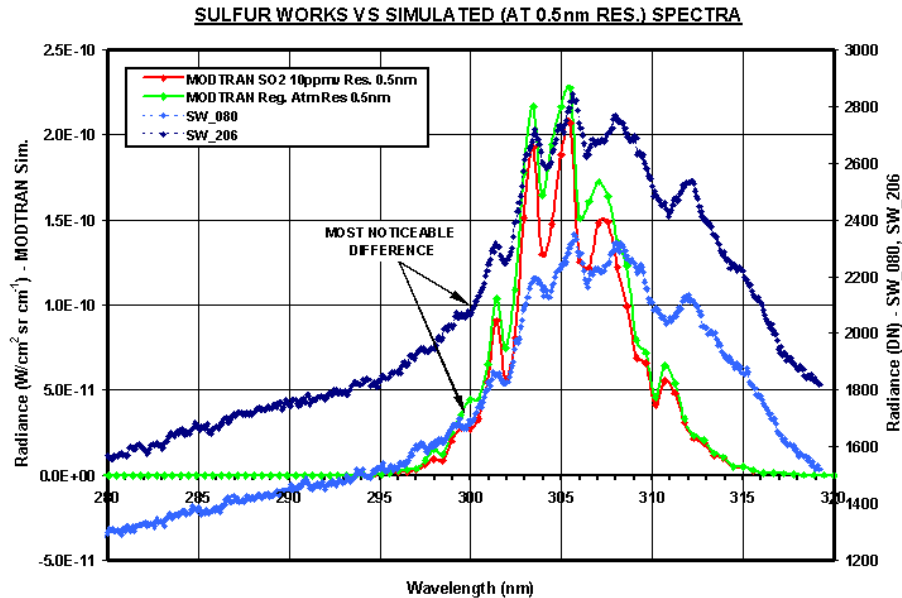


Figure 8.23. Measured and simulated spectral profiles of clear atmosphere and simulated with 10ppmv SO<sub>2</sub> atmosphere. The simulated data are in 0.5nm resolution.

Furthermore, ratios between experimental and simulated data were investigated. The simulated data were remapped to the experimental data wavelength coordinates using interpolation, so that the ratios could be calculated. Some of the results are presented in figures 8.24 through 8.26.

Figure 8.24 shows the ratios of two images taken at Sulfur Works (SW\_080, SW\_206) and one at Lassen Peak (SW\_503) divided by simulated clear atmosphere spectra. The first two images are taken over the vents while the third is a clear atmosphere image. The structure of all the curves looks nearly identical with the most noticeable difference at 300nm.

Figure 8.25 shows inverted ratios between simulated clear atmosphere and simulated atmosphere with 10ppmv SO<sub>2</sub> divided by experimental clear atmosphere spectra. There is a significant change at 300nm. Finally, figure 8.26 illustrates plots of ratios of more data sets, which are consistent with the above observations. The difference at 300nm appearing in all figures is caused by the simulated SO<sub>2</sub> concentration, implying that this is the point for which the most significant SO<sub>2</sub> effect in measurements should be searched.

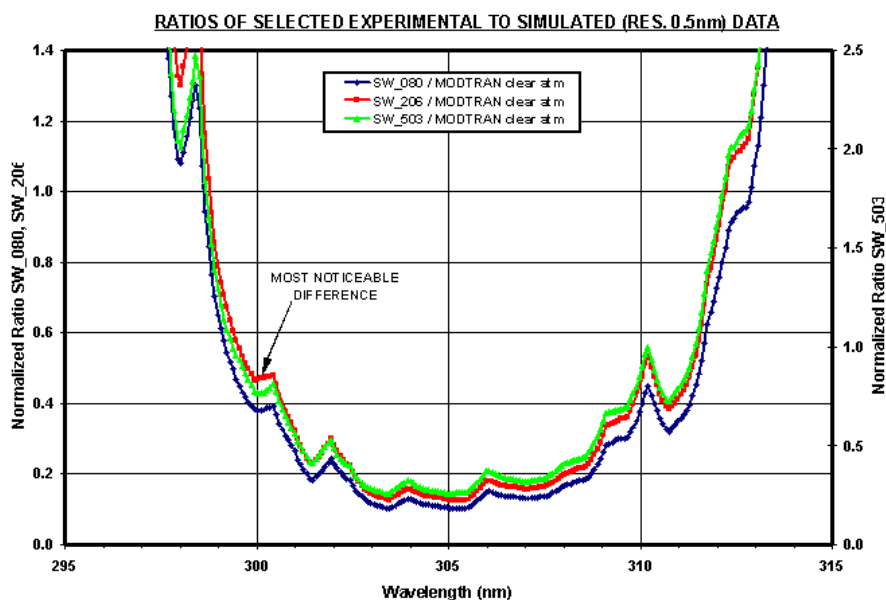


Figure 8.24. Ratios of data taken over the Sulfur Works vents (SW\_080 and SW\_206) and clear atmosphere at Lassen Peak (SW\_503) divided by simulated clear atmosphere.

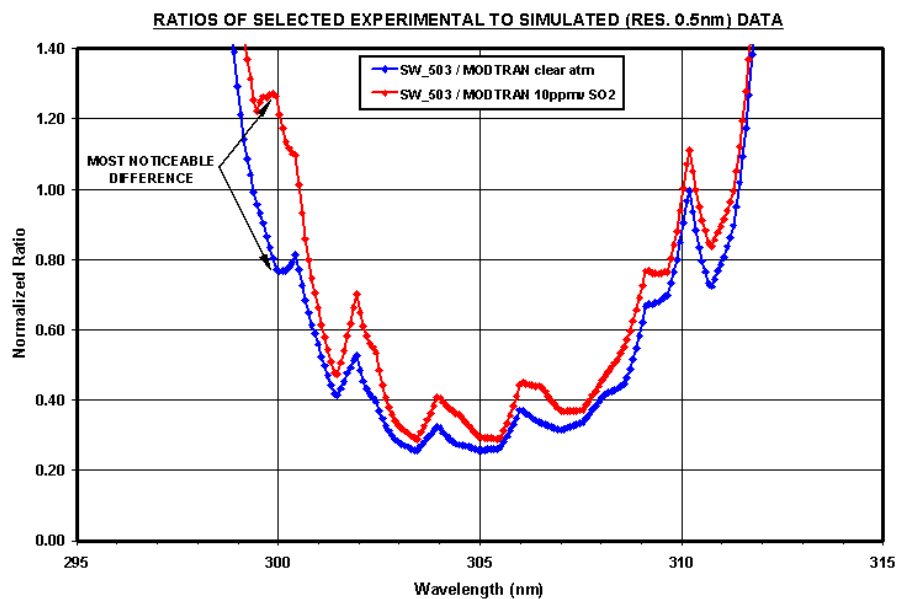


Figure 8.25. Inverted ratios of simulated clear atmosphere and 10ppmv of  $\text{SO}_2$ -containing atmosphere divided by clear atmosphere at Lassen Peak (SW\_503).

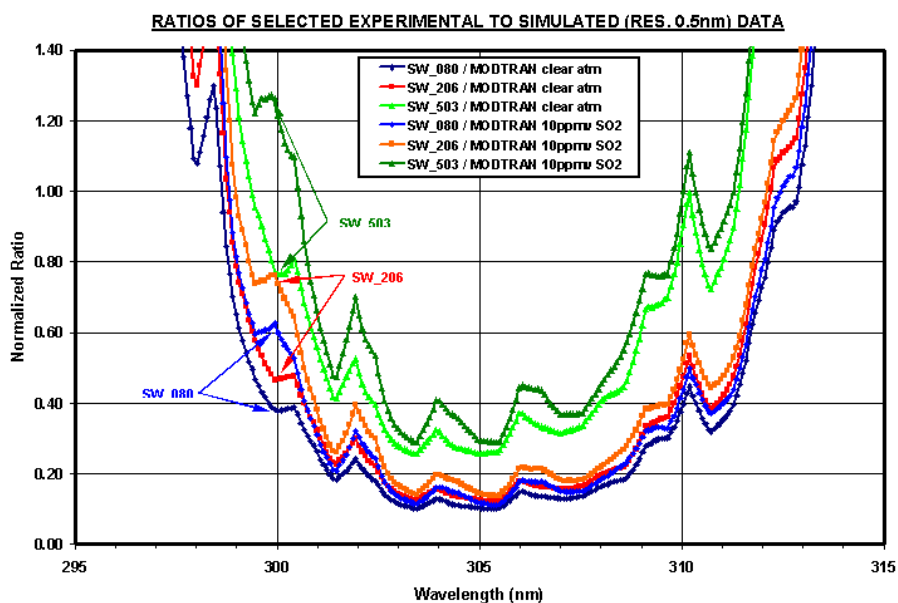


Figure 8.26. Ratios of selected experimental to simulated data.



Finally, figure 8.27 compares MODTRAN with SO<sub>2</sub> calibration data. The MODTRAN curve is the ratio of atmosphere containing 10ppmv SO<sub>2</sub>, divided by clear atmosphere. The SO<sub>2</sub> calibration curve is the ratio of the data acquired with 100mmHg of SO<sub>2</sub> in the photocell, divided by the data with the photocell evacuated. There is a very good agreement in the absorption characteristics of the gas around the center of the maximum spectral response of the filter. Disagreement away from 300nm is due to the differences between real and simulated filter response. There is also a shift in wavelength associated with the focus of radiation on the focal plane of the instrument (Gray, 2002).

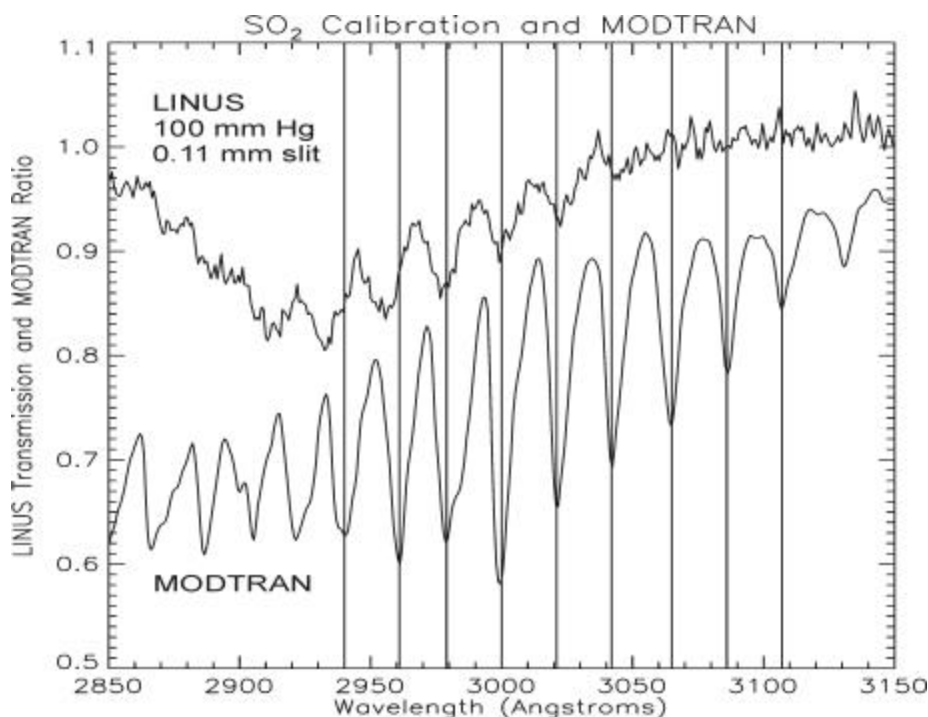


Figure 8.27. Comparison between MODTRAN and SO<sub>2</sub> calibration absorption characteristics.

#### D. SUMMARY

Initially MODTRAN simulations were used in order to identify the absorption characteristics of SO<sub>2</sub> and its presence signatures at various concentrations and spectral resolutions. Then, experimental data processing aimed to determine if those characteristics and signatures were present in the images taken at Sulfur Works. Finally, a

combined analysis was performed. The observations deduced from the analysis are summarized below:

- The simulated data have SO<sub>2</sub> absorption characteristics that agree very well with the laboratory absorption cross section measurements described in chapter III (figures 3.2, 3.7 and 8.2 through 8.6).
- According to the simulations, SO<sub>2</sub> presence in the atmosphere causes differences in the spectral profiles, which are very small in small concentrations but increase and are noticeable in larger concentrations.
- Ratios of simulated SO<sub>2</sub>-containing and clear atmosphere reveal a clear and characteristic signature even for low concentrations (figures 8.7 and 8.8).
- The spectral profile of the simulated clear atmosphere in the region of interest is mainly due to solar irradiance (figure 8.12).
- According to the SO<sub>2</sub> calibration, LINUS can record the fine spectral structure caused by SO<sub>2</sub> absorption bands at slit widths around 0.11mm (figure 8.14).
- Comparisons of the experimental data taken at Sulfur Works (atmosphere possibly containing SO<sub>2</sub>) and Lassen Peak (clear atmosphere) show that the most noticeable differences occur at 297.7 and 299.7nm (figure 8.16).
- The details of the experimental spectral profiles match those simulated at 0.5nm resolution much better than those of the finer 0.08nm resolution. This indicates that LINUS with a 0.11mm slit width operates at about 0.5nm resolution (figures 8.21 and 8.22).
- There is a good agreement between simulated and experimental data from about 290 to 306nm. From 306nm and above, the experimental profile becomes wider and the peaks and troughs are in different wavelength positions. This is attributed to effects of the filter of the device to the recorded radiation, which could not be reproduced by the filter simulation.
- Combined analysis of the experimental and simulated data of 10ppmv SO<sub>2</sub> concentration indicated that the largest noticeable difference is at 299.9nm which corresponds to the maximum of the absorption cross section of the SO<sub>2</sub> molecule (figure 8.23).
- The ensemble analysis approach did not reveal any bold SO<sub>2</sub> absorption characteristics in the experimental data.

The final conclusion for the measurements taken at Lassen Park is that there are minor indications of SO<sub>2</sub> presence in the sulfuric plums emanating at Sulfur Works. The concentration is estimated to be much less than 10ppmv. This result is in contradiction with what was expected when the site was selected for the LINUS first measurements.

Extensive investigation in the literature in order to find out any previous measurements or gas analysis of the Sulfur Works emanations did not reveal anything. The U.S. Geological Survey was conducted and communication with Mr. M. A. Clynné of the Volcano Hazards Team indicated that Sulfur Works plumes should not have any or have very little  $\text{SO}_2$ . This is the case for any gas coming through an aqueous fluid, because  $\text{SO}_2$  dissociates into  $\text{H}_2\text{S}$  and  $\text{S}$ , and in effect, is scrubbed from the plume. This is in agreement with the results of this thesis.

THIS PAGE INTENTIONALLY LEFT BLANK

## IX. SUMMARY, CONCLUSIONS AND RECOMMENDATIONS

This thesis is one small step in investigating the concept of passive detection of gases in an extended scene in the atmosphere by using the principles of remote sensing in the ultraviolet region of the electromagnetic spectrum. Specifically, the sensor used was LINUS (Lineate Imaging Ultraviolet Spectrometer) and the gas under study was sulfur dioxide ( $\text{SO}_2$ ). Due to problems with the scanning software at the time this thesis was conducted, LINUS was mainly used as a spectrometer instead of an imager.

The first goal of this project, which was to develop the operational capability of LINUS and deploy it for the first time in the field in order to acquire data of natural plumes, was successfully accomplished. The device was deployed at Lassen Volcanic National Park in August and September of 2002, and a number of measurements of the sulfuric plumes and clear atmosphere in the area were acquired. During those deployments, a number of problems were encountered. On site or subsequent solutions to those problems, established non-existent knowledge and experience in using the device outside the laboratory. The response of the device was also investigated by changing various settings, such as the slit width, acquisition time and microchannel plate gain.

Furthermore, modeling of the data was performed using MODTRAN4. Modeling was designed to simulate the signal going into the device optics section after it had passed through the UV filter. The specific conditions under which several measurement sets were taken, were simulated. The simulations were in very good agreement with laboratory  $\text{SO}_2$  absorption cross section measurements found in the literature and gave an indication of how the LINUS data should look like in the wavelength-radiance space. They also established an  $\text{SO}_2$  absorption signature that was used to identify  $\text{SO}_2$  absorption effects in the experimental data.

The experimental data were analyzed using an individual image analysis approach by selecting specific images and investigating their spectral structure, and an ensemble approach, where the images were processed as a whole in order to identify the presence of bold  $\text{SO}_2$  characteristics. The first approach showed minor  $\text{SO}_2$  presence indications, while the second did not.

Details of the analysis, findings and observations are presented in the previous chapter. The final conclusion for the measurements taken at Lassen Park is that there are minor indications of SO<sub>2</sub> presence in the sulfuric plums emanating at Sulfur Works. The concentration is estimated to be much less than 10ppmv. This result is in contradiction with what was expected when the site was selected for the LINUS first measurements. Extensive investigation in the literature did not reveal any previous measurements or gas analysis of the Sulfur Works emanations. Communication with Mr. M. A. Clynne of the U.S. Geological Survey Volcano Hazards Team indicated that there should be little or no SO<sub>2</sub> in the plumes emanating from Sulfur Works, since it is a hot springs area with no hot magma. This is in agreement with the results of this thesis.

Follow-on work on this project should include the following:

- Replacement of the existing UV filter, with a new filter of wider spectral response centered at 300nm and higher transmission coefficient.
- Determination of LINUS spectral resolution at various slit widths and measurement of the SO<sub>2</sub> detection threshold concentration.
- Selection of a new site for measurements with a definite and, if possible, known or estimated SO<sub>2</sub> concentration by other means, so that direct comparisons with LINUS results can be done. The sites could be either active volcanoes or smoke stacks with SO<sub>2</sub>-rich plumes.

# APPENDIX A. MODTRAN INPUT CARDS AND VARIABLES

MAIN RADIATION TRANSPORT DRIVER - REQUIRED													
CARD 1	MODTRN	SPEED	MODEL	ITYPE	IMSCAT	IMULT	M1	M2	M3	M4	M5	M6	MDEF
VARIABLE TYPE / COLUMN NUMBER	A1 (1)	A1 (2)	I3 (3-5)	I5 (6-10)	I5 (11-15)	I5 (16-20)	I5 (21-25)	I5 (26-30)	I5 (31-35)	I5 (36-40)	I5 (41-45)	I5 (46-50)	I5 (51-55)
VARIABLE VALUE	M	blank	7	3	2	1	0	0	0	0	0	0	0
RADIATIVE TRANSPORT DRIVER (CONTINUED) - REQUIRED													
CARD 1A	DIS	DISAZM	NSTR	LSUN	ISUN	CO2MX	H2OSTR	O3STR	LSUNFL	LMNVA	LFLTNM	H2OAEF	SOLCON
VARIABLE TYPE / COLUMN NUMBER	L1 (1)	L1 (2)	I3 (3-5)	L1 (6)	I4 (7-10)	F10.5 (11-20)	A10 (21-30)	A10 (31-40)	I4X,A1 (42)	I4X,A1 (44)	I4X,A1 (46)	I4X,A1 (48)	2X,F10.3 (51-60)
VARIABLE VALUE	T	T	8	F or T	0 or 2	365.000000	0	0	F	T	F	F	0.000
SPECTRAL DATA AND SENSOR RESPONSE FUNCTION FILE - OPTIONAL													
CARD 1A2	BMNAME	Comments											
VARIABLE TYPE / COLUMN NUMBER	A80	If LBMNAME=T in card											
VARIABLE VALUE	DATAEMP99_01.BIN	1A											
MAIN AEROSOL AND CLOUD OPTIONS - REQUIRED													
CARD 2	APLUS	IHAZE	CNOVAM	ISEASN	ARUSS	IVULCN	ICSTL	ICLD	IVSA	VIS	WSS	WHH	RAINRT
VARIABLE TYPE / COLUMN NUMBER	A2 (1-2)	I3 (3-5)	A1 (6)	I4 (7-10)	A3(11-13)	I2 (14-15)	I5 (16-20)	I5(21-25)	I5 (26-30)	F10.5 (31-40)	F10.5 (41-50)	F10.5 (51-60)	F10.5 (61-70)
VARIABLE VALUE	blank	1	blank	0	blank	0	0	0	0	0.00000	0.00000	0.00000	2.13000
USER-DEFINED ATMOSPHERIC PROFILES - OPTIONAL													
CARD 2C	ML	IRD1	IRD2	TITLE									
VARIABLE TYPE / COLUMN NUMBER	I5 (1-5)	I5 (6-10)	I5 (11-15)	A65 (16-80)									
VARIABLE VALUE	36	1	0	text									
CARD 2C1	ZMDL	P	T	WMOL(1)	WMOL(2)	WMOL(3)	JCHAR(J)	J=1, 14	JCHARX	Comments			
VARIABLE TYPE / COLUMN NUMBER	F10.3 (1-10)	E10.3 (11-20)	E10.3 (21-30)	E10.3 (31-40)	E10.3 (41-50)	E10.3 (51-60)	14A1	(61-74)	I4X,A1 (76)	Example of the 1st atmospheric layer			
VARIABLE VALUE	2.130	0.000E+00	2.200E+01	0.000E+00	0.000E+00	0.000E+00	2B22222222A222	2					
CARD 2C2	WMOL(4)	WMOL(5)	WMOL(6)	WMOL(7)	WMOL(8)	WMOL(9)	WMOL(10)	WMOL(11)	WMOL(12)	Comments			
VARIABLE TYPE / COLUMN NUMBER	E10.3 (1-10)	E10.3 (11-20)	E10.3 (21-30)	E10.3 (31-40)	E10.3 (41-50)	E10.3 (51-60)	E10.3	E10.3	E10.3	If RD1=1 on card 2C, WMOL(9) is the SO2 concentration			
VARIABLE VALUE	0.000E+00	0.000E+00	0.000E+00	0.000E+00	0.000E+00	0.000E+00	0.000E+00	0.000E+00	0.000E+00				
LINE-OF-SIGHT GEOMETRY - REQUIRED													
CARD 3STD	H1	H2	ANGLE	RANGE	BETA	RO	LENN	PHI	Comments				
VARIABLE TYPE / COLUMN NUMBER	F10.3 (1-10)	F10.3 (11-20)	F10.3 (21-30)	F10.3 (31-40)	F10.3 (41-50)	F10.3 (51-60)	I5 (61-65)	5X,F10.3 (71-80)					
VARIABLE VALUE	2.130	blank	70.000	0.000	0.000	0.000	0	0.000					

**SOLAR/LUNAR SCATTERING GEOMETRY - OPTIONAL**

<b>CARD 3A1</b>		IPARM	IPH	IDAY	ISOURC	Comments
VARIABLE TYPE / COLUMN NUMBER	I5 (1-5)	I5 (6-10)	I5 (11-15)	I5 (16-20)	If IEM SCT=2 on card 1	
VARIABLE VALUE	1	2	255	0		

<b>CARD 3A2</b>		PARM1	PARM2	PARM3	PARM4	TIME	PSIPO	ANGLEM	G	Comments
VARIABLE TYPE / COLUMN NUMBER	F10.3 (1-10)	F10.3 (11-20)	F10.3 (21-30)	F10.3 (31-40)	F10.3 (41-50)	F10.3 (51-80)	F10.3 (81-90)	F10.3 (91-100)	If IEM SCT=2 on card 1	
VARIABLE VALUE	40.450	121.530	blank	blank	18.700	290.000	blank	blank		

**SPECTRAL RANGE AND RESOLUTION - REQUIRED**

<b>CARD 4</b>		V1	V2	DV	FWHM	YFLAG	XFLAG	DLIMIT	FLAGS	Comments
VARIABLE TYPE / COLUMN NUMBER	F10.0 (1-10)	F10.0 (11-20)	F10.0 (21-30)	F10.0 (31-40)	F10.0 (41-50)	A1 (41)	A1 (42)	A8 (43-50)	A7 (51-57)	
VARIABLE VALUE	20000	50000	1	2		R	W	blank	7blanks	

**REPEAT RUN OPTIONS - REQUIRED**

<b>CARD 5</b>		IRPT	Comments
VARIABLE TYPE / COLUMN NUMBER	I5 (1)		
VARIABLE VALUE	0		



## APPENDIX B. EXAMPLES OF MODTRAN INPUT CARDS

Two examples of MODTRAN input cards are presented in this appendix. In the first three pages, the input data are presented together with their “coordinates”, a column number from 01 to 80 in the first and last two rows and the card number in the first five columns. These “coordinates” are used for user/reader convenience and do not exist in a normal input file. In the last two pages of the appendix, a normal input file is presented. The files simulate measurements at Sulfur Works Location 2 with a 10ppmv concentration of SO<sub>2</sub> in the first atmospheric layer with thickness 90m.

[illegible]

102

103

104

105

THIS PAGE INTENTIONALLY LEFT BLANK

## APPENDIX C. SELECTED SPECTRAL PROFILES FROM EXPERIMENTAL DATA

This appendix shows plots of the spectral profiles of selected images taken with LINUS at Sulfur Works Location 2 and Lassen Peak (Location 3).

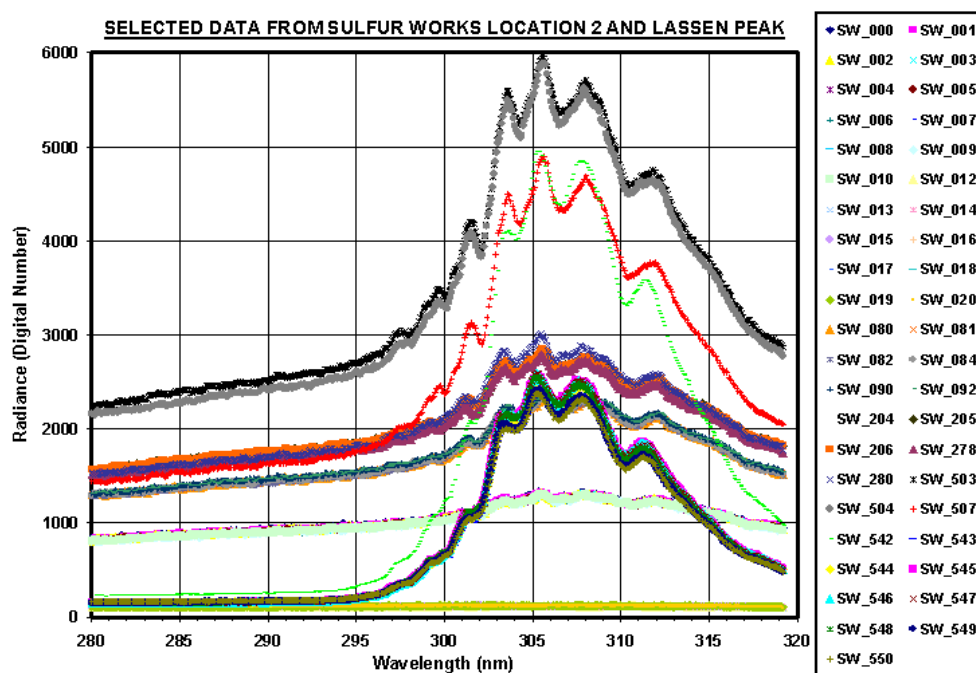


Figure C.1. Plot of the spectral profiles of all selected images.

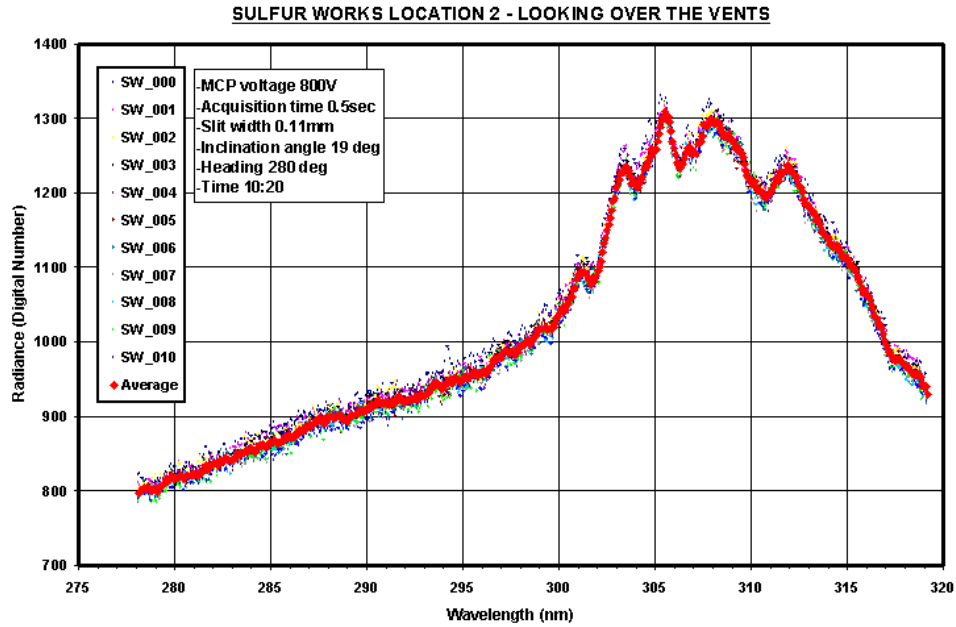


Figure C.2. Plot of spectral profiles of one group of selected images at Sulfur Works.

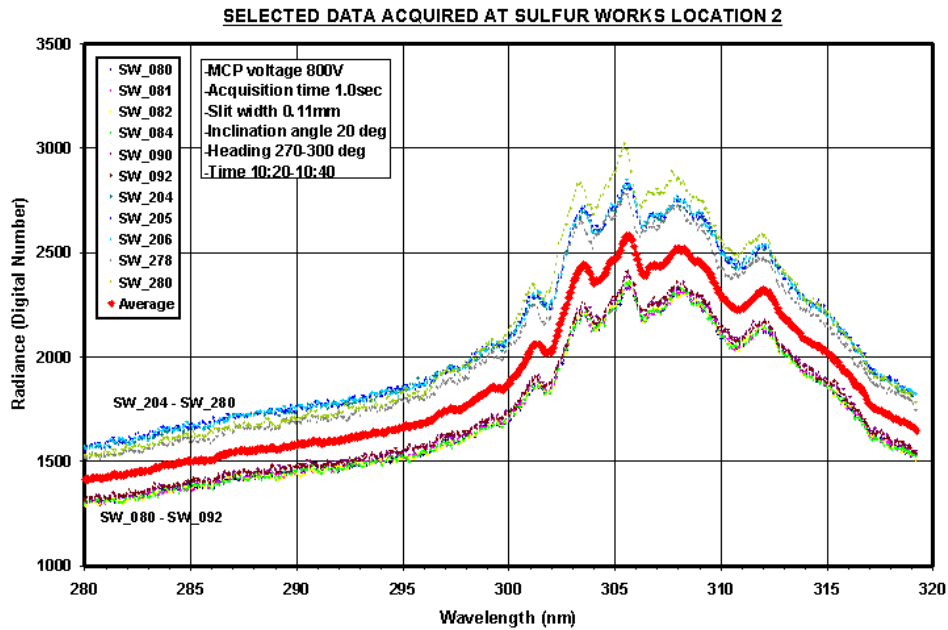


Figure C.3. Plot of spectral profiles of another group of selected images at Sulfur Works.



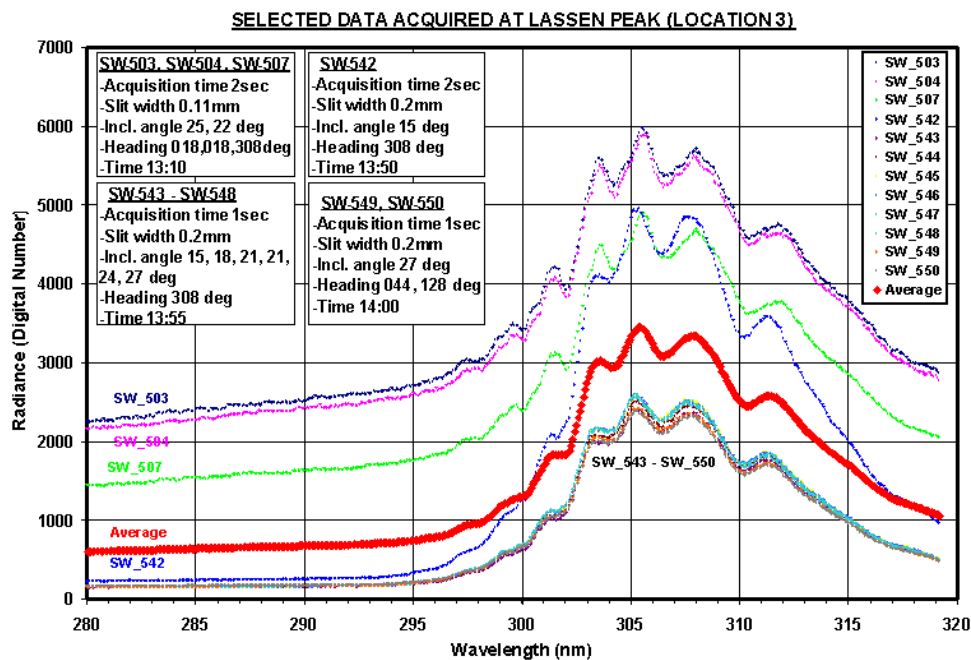


Figure C.4. Plot of spectral profiles of selected images at Lassen Peak.

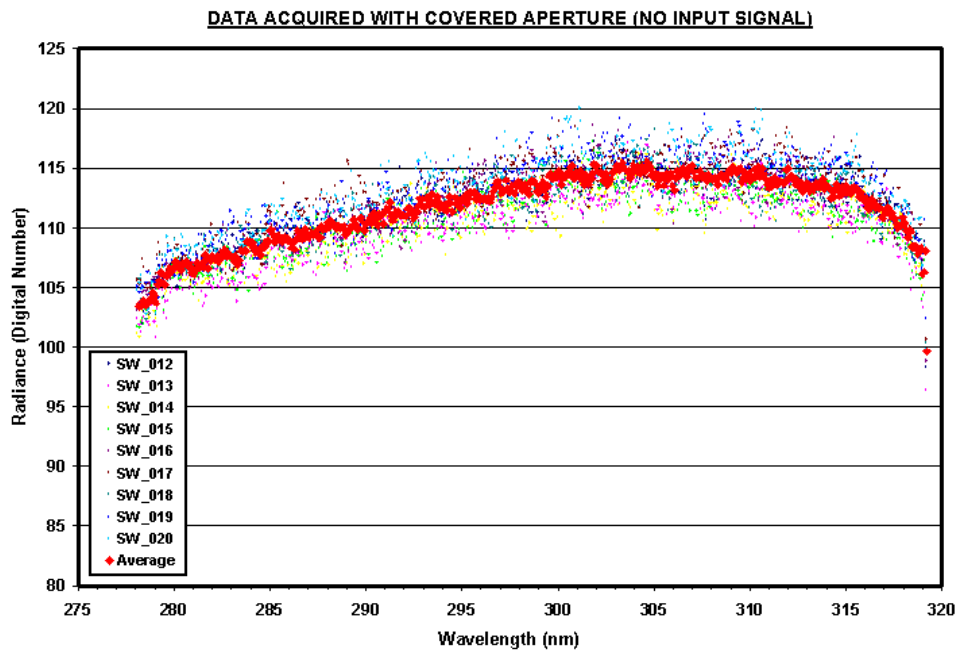


Figure C.5. Plot of spectral profiles of measurements taken with the aperture of LINUS covered.

THIS PAGE INTENTIONALLY LEFT BLANK

## LIST OF REFERENCES

- Acharya, P. K., Berk, A., Anderson, G. P., Larsen, N. F., Tsay, C., and Stamnes, K. H., "MODTRAN4: Multiple Scattering and Bi-Directional Reflectance Distribution Function (BRDF) Upgrades to MODTRAN", SPIE Proceeding: Optical Spectroscopic Techniques and Instrumentation for Atmospheric and Space Research III, 1999.
- Adler-Golden, S. M., Matthew, M. W., Bernstein, L. S., Levine, R.Y., Berk, A., Richtsmeier, S. C., Acharya, P. K., Anderson, G. P., Felde, G., Gardner, J., Hoke, M., Jeong, L. S., Pukall, B., Mello, J., Ratkowski, A., and Burke, H. H., "Atmospheric Correction for Short-wave Spectral Imagery Based on MODTRAN4", SPIE Proceeding: Imaging Spectrometry V, 1999.
- Anderson, G. P., Kneizys, F. X., Chetwynd, J. H., Wang, J., Hoke, M. L., Rothman, L. S., Kimball, L. M., and McClatchey, R. A., "FASCODE / MODTRAN / LOWTRAN: Past / Present / Future", 18th Annual Review Conference on Atmospheric Transmission Models, 1995.
- Atkins, P. W., "Physical Chemistry", Freeman, 1982.
- Barrett, E. C. and Curtis, L. F., "Introduction to Remote Sensing", Chapman & Hall Ltd, 1982.
- Berk, A., Acharya, P. K., Bernstein, L. S., Anderson, G. P., Chetwynd, J. H., and Hoke, M. L., "Reformulation of the MODTRAN Band Model for Higher Spectral Resolution", SPIE Proceeding: Algorithms for Multispectral, Hyperspectral, and Ultraspectral Imagery VI, 2000.
- Berk, A., Anderson, G. P., Bernstein, L. S., Acharya, P. K., Dothe, H., Matthew, M. W., Adler-Golden, S. M., Chetwynd, J. H., Richtsmeier, S. C., Pukall, B., Allred, C. L., Jeong, L. S., and Hoke, M. L., "MODTRAN4 Radiative Transfer Modeling for Atmospheric correction", SPIE Proceeding: Optical Spectroscopic Techniques and Instrumentation for Atmospheric and Space Research III, 1999.
- Berk, A., Bernstein, L. S., and Robertson, D. C., "MODTRAN: A Moderate Resolution Model for LOWTRAN 7", Air Force Geophysics Laboratory, 1989.
- Berk, A., Anderson, G. P., Acharya, P. K., Chetwynd, J. H., Bernstein, L. S., Shettle, E. P., Matthew, M. W., and Adler-Golden S. M., "MODTRAN4 User's Manual", Air Force Research Laboratory / Space Vehicles Directorate, 1999.
- Bernath, P. F., "Spectra of Atoms and Molecules", Oxford University Press, 1995.
- Brassington, D. J., "Sulfur Dioxide Absorption Cross-Section Measurements from 290 nm to 317 nm", Journal of Applied Optics, v. 20, pp. 3774-3779, 1981.

Campbell, J. B., "Introduction to Remote Sensing", Guilford Press, 1987.

Casadevall, T. J., Stokes, J. B., Greenland, L. P., Malinconico, L. L., Casadevall, J. R. and Furukawa, B. T., "SO<sub>2</sub> and CO<sub>2</sub> Emission Rates at Kilauea Volcano, 1979-1984", U.S. Geological Survey Professional Paper 1350, 1987.

Casadevall, T. J., Johnston, D. A., Harris, D. M., Rose, W. I., Malinconico, L. L., Stoiber, R. E., Bornhorst, T. J., Williams, S. N., Woodruff, L. and Thompson, J. M., "SO<sub>2</sub> Emission Rates at Mount St. Helens from March 29 through December, 1980", U.S. Geological Survey Professional Paper 1250, 1981.

Elachi, C., "Introduction to Physics and Techniques of Remote Sensing", Wiley, 1987.

Elias, T., "Sulfur Dioxide Emission Rates of Kilauea Volcano, Hawaii, 1979-1997", U.S. Geological Survey Professional Paper 1623, 1998.

"Encyclopedia of Volcanoes", Academic Press, 2000.

Gibson, P. J., "Introduction to Remote Sensing", Routledge, 2000.

Goody, R. M., and Yung, Y. L., "Atmospheric Radiation", Oxford University Press, 1989.

Gray, J., "Design and First Operations of the Lineate Imaging Near-Ultraviolet Spectrometer (LINUS)", Master's Thesis, Naval Postgraduate School, Monterey, California, December 2002.

Hecht, E., "Optics", A. Wesley, 2002.

Kneizys, F. X., Anderson, G. P., Shettle, E. P., Gallery, W. O., Abreu, L. W., Selby, J. E. A., Chetwynd, J. H., and Clough, S. A., "Users Guide to LOWTRAN 7", Air Force Geophysics Laboratory, 1988.

Kompatzki, R. C., "Design and Development of the Image Scanner for Lineate Imaging Near UV Spectrometer (LINUS)", Master's Thesis, Naval Postgraduate School, Monterey, California, December 2000.

Kuriger, D. W., "Absolute Calibration Techniques for UV Spectroscopy Based upon Platinum Emission Line Spectra", Master's Thesis, Naval Postgraduate School, Monterey, California, December 2001.

"Manual of Remote Sensing", American Society of Photogrammetry, 1983.

Mares, A. G., “Remotely Sensed Density Measurements of Volcanic Sulfur Dioxide Plumes Using a Spectral Long Range Infrared Imager”, Master’s Thesis, Naval Postgraduate School, Monterey, California, September 2002.

Marino, S. A., “Operation and Calibration of the NPS UV Imaging Spectrometer (NUVIS) in the Detection of Sulfur Dioxide Plumes”, Master’s Thesis, Naval Postgraduate School, Monterey, California, December 1999.

Matthew, M. W., Adler-Golden S. M., Berk, A., Richtsmeier, S. C., Levine, R. Y., Bernstein, L. S., Acharya, P. K., Anderson, G. P., Felde, G. W., Hoke, M. L., Ratkowski, A., Burke, H. H., Kaiser, R. D. and Miller, D. P., “Status of Atmospheric Correction Using a MODTRAN4-based Algorithm”, SPIE proceeding: Algorithms for Multispectral, Hyperspectral, and Ultraspectral Imagery VI, 2000.

McGee, T. J., and Burris, J., “SO<sub>2</sub> Absorption Cross Sections in the Near UV”, Journal of Quantitative Spectroscopy and Radiative Transfer, v. 32, p. 165 -182, 1987.

Millan, M. M., Hoff, R. M, Gallant, A. J., “Tall Stacks, Plume Dispersion and Emission Calculations by Correlation Spectroscopy”, Air Pollution Control Association, 1976.

National Aeronautics and Space Administration (NASA) web sites, 2002.

Realmuto, V. J., “The Potential Use of Earth Observing System Data to Monitor the Passive Emission of Sulfur Dioxide from Volcanoes”, American Geophysical Union, 2000.

Realmuto, V. J., “Volcanic SO<sub>2</sub> – High and Moderate Spatial Resolution”, Jet Propulsion Laboratory, 1995.

“Remote Sensing of Active Volcanism”, American Geophysical Union, 2000.

Richards, J. A. and Jia, X., “Remote Sensing Digital Analysis”, Springer, 1999.

Rothman, L. S., “The HITRAN Molecular Spectroscopic Database and HAWKS (HITRAN Atmospheric Workstation): 1996 Edition”, Journal of Quantitative Spectroscopy and Radiative Transfer, 1998.

Stamnes, K., Tsay, C., Wiscombe, W. and Jayaweera, K., “ Numerically Stable Algorithm for Discrete-Ordinate-Method Radiative Transfer in Multiple Scattering and Emitting Layered Media”, Journal of Applied Optics, 1998.

Stoiber, R. E., Malinconico, L. L. and Williams, S. M., “Use of the Correlation Spectrometer at Volcanoes”, Elsevier, 1983.

Thompson Jr., R. T., Hoell Jr., J. M. and Wade, W. R., "Measurements of SO<sub>2</sub> Absorption Coefficients Using a Tunable Dye Laser", Journal of Applied Physics, v. 46, pp. 3040-3043, 1975.

U.S. Geological Survey (USGS) web site, 2002.

Vandaele, A. C., Simon, P. C., Guilmot, J. M., Carleer, M. and Colin, R., "SO<sub>2</sub> Absorption Cross Section Measurements in the UV Using a Fourier Transform Spectrometer", Journal of Geophysical Research Section D Atmospheres, v. 99, p. 25599-25605, 1994.

Woods, P. T., Jolliffe, B. W. and Marx, B. R., "High Resolution Spectroscopy of SO<sub>2</sub> Using a Double Pulsed Dye Laser, with Application to the Remote Sensing of Atmospheric Pollutants", Optics Communications Journal, v. 33, p. 281, 1980.

World Ozone and Ultraviolet Radiation Data Center (WOUDC) web site, 2002.

## INITIAL DISTRIBUTION LIST

1. Defense Technical Information Center  
Ft. Belvoir, Virginia
2. Dudley Knox Library  
Naval Postgraduate School  
Monterey, California
3. Richard C. Olsen, Code PH/OS  
Department of Physics  
Naval Postgraduate School  
Monterey, California
4. Richard M. Harkins Code PH/HR  
Department of Physics  
Naval Postgraduate School  
Monterey, California
5. David S. Davis  
Department of Physics  
Naval Postgraduate School  
Monterey, California
6. William B. Maier  
Department of Physics  
Naval Postgraduate School  
Monterey, California
7. Hellenic Air Force General Staff  
B Branch, B1 Directorate  
Stratopedo Papagou  
Athens, Greece
8. Embassy of Greece  
Office of the Air Attaché  
Washington D.C.
9. Anastasios G. Halvatzis  
Hellenic Air Force  
Thessaloniki,  
Greece